

Final Report

DFG Research Group FOR575

High Frequency Parasitic Effects in Inverter-fed Electric Drives

*Höherfrequente Parasitäreffekte in
umrichtergespeisten elektrischen Antrieben*

Prof. Dr.-Ing. habil. Dr.h.c. Andreas Binder (Sprecher)
Prof. Dr.-Ir. Herbert De Gersem
Prof. Dr.-Ing. Volker Hinrichsen
Prof. Dr.-Ing. Peter Mutschler
Prof. Dr.-Ing. Thomas Weiland

Darmstadt, September 2009

Responsible for the report:

Prof. Dr.-Ing. habil. Dr.h.c. Andreas Binder, geb. 16.7.1957
Technische Universität Darmstadt
Institut für Elektrische Energiewandlung
Fachbereich 18 - Elektrotechnik und Informationstechnik
Landgraf-Georg-Straße 4, D-64283 Darmstadt
Telefon: 06151/16-2167, Fax: 06151/16-6033
E-Mail: abinder@ew.tu-darmstadt.de

1. Summary

This report summarizes the results of the research work of the first phase of the DFG Forschergruppe FOR575.

2. Introduction

During the first phase, the members of the DFG Research Group FOR575 have had 27 regular internal meetings. The meetings allowed the presentation of results in a scientific environment and created a fruitful connection between the professors and research members. They are documented in detail on the FOR575 homepage, where all the meeting protocols and power point presentations are available: <http://www.ew.e-technik.tu-darmstadt.de/cms/index.php>

The six projects of the DFG Research Group FOR575 are listed in Table 1, where the PhD students of the group for the first phase are presented. The results of the research are presented in a number of 24 scientific papers (section 3), which have already been published or will be published in the near future, being accepted in different journals and proceedings of the most important international conferences, dealing with electrical machines, drives and electromagnetic simulations.

TP1-Binder	<i>Calculation of parasitic high frequency current distribution in inverter-fed electrical machines</i> Dipl.-Ing. Oliver Magdun (Romania), Tutor: Prof. A. Binder
TP2-Binder	<i>Comparative analysis of losses in inverter-fed machines caused by high frequency current components using time-stepping</i> Dipl.-Ing. Ljubisa Petrovic (Serbia), Dipl.-Ing. Mehran Mirzaei (Iran), Tutor: Prof. A. Binder
TP3-DeGersem	<i>Simulation of wave propagation phenomena in inverter-fed drives</i> Dr.-Ing. Dipl.-Phys. Olaf Henze (Germany), Tutor: Prof. De Gersem
TP4-Hinrichsen	<i>Ageing mechanisms and energy handling capability of metal-oxide varistors for overvoltage protection in inverter-fed drives</i> Dipl.-Ing. Alexander Rocks (Germany), Tutor: Prof. Hinrichsen (No financial support from DFG)
TP5-Mutschler	<i>Influencing the voltage slope at the inverter output by modifying the switching behaviour of the IGBT power modules, accomplished by special gate drivers</i> Dipl.-Ing. Calin Purcarea (Romania), Tutor: Prof. Mutschler
TP6-Weiland	<i>Multiscale modelling and extraction of parameters in the simulation of inverter-fed drives</i> M.Sc. Zarife Cay (Turkey), Tutor: Prof. Weiland

Table 1.1. The 6 projects of the DFG Research Group FOR575, 1st phase

3. Overview on the research topics

In electrical drive systems, parasitic effects such as electromagnetic interferences (EMI) or circulating bearing currents are caused by the common mode (CM) stator ground currents. To calculate them, complex mathematical models of cables and electric machines at high frequency are necessary. Mr. Magdun dealt in **TP1**, with the development of suited cable and motor models for the calculation and prediction of CM currents. He proposed calculation methods of the CM currents with a) simplified equivalent circuit models per phase and b) distributed equivalent circuit

models per phase with parameters, which depend on the frequency to obtain a better modeling of the skin and proximity effects for the stator coil conductors within the slots and in the iron vicinity. The measured or calculated line-to-earth voltage has to be applied at the circuit input terminals. As cable models are necessary to calculate the line-to-earth voltage, a numerical calculation of the cable parameters has been performed with good results related to measurements.

In **TP2**, Mr. Petrovic and Mr. Mirzaei dealt with the calculation of eddy current losses in the rotor permanent magnets (PM) of synchronous machines with concentrated windings for high utilization in direct drive systems. Different calculation methods are compared in the Finite-Element environment: 1) analytical post processing of FE magnetostatic data with multi-move and eddy currents calculated from vector potential, 2) direct FE magneto-static method and 3) time stepping with a FE program. The axial segmentation effect on eddy current loss in magnets is taken into account by a new developed analytical method. In a second step, the additional losses in cage induction machines were simulated in a time-stepping procedure for high speed motors for the use in electric cars. Both types of machines were available as prototypes and so the measurement results could be used to evaluate the calculated losses.

Dr. Henze dealt, in **TP3**, with network models for inverter-fed induction motors, which operate at steady state. The models are based on the transmission line matrix (TLM) method, considering the cable impedance, capacitance, conductivity and resistance, described by 3x3 matrices combined with a 3 phase (abc)-model for the induction machine. The result is a transfer function, which couples the input voltage with the output voltage at the motor. To calculate the voltage at the motor, the voltages pulses from the inverter are transformed into the frequency domain via FFT. In the frequency domain, the voltage at the motor is computed by multiplication with the transfer function. For studying of high-frequency parasitic effects in inverter-fed drives, a transmission-line model for the stator coils of the induction machines has been proposed. In a second step, a detailed Finite-Integration-Model of multiline coil in a slot with sheets of conductive iron were numerically investigated to calculate the common mode current per turn at high current frequencies.

In **TP4**, Mr. Rocks dealt with the protection of the machine windings of inverter-fed drives against overvoltages, caused by traveling waves on electrically long lines. The use of ZnO varistors for overvoltage protection in inverter-fed drives can be a promising alternative to common solutions like filters. In this project the varistor's influence on the voltage distribution in the stator winding is presented under certain aspects such as cable type and varistor type. The main design for a long varistor life, which switches e.g. 3000 times per second is a broad cross section to get a low current density for low switching losses. The height of the varistors is adjusted to the operating voltage and can be small in low voltage AC machines. The varistor capacities, which is active before each switching instant reduces the voltage overload due to the voltage wave reflection. The voltage amplitudes are reduced and the voltage distribution is linearised within the winding, which increases the life time of the winding insulation of the machines. Otherwise the overvoltage in combination with a very short rise times imposes due to a non-linear voltage distribution an extreme dielectric stress on the insulation of electrical machines. With varistor discs it is possible to limit these overvoltages in combination with an increased rise time of the impulses occurring at the machine terminals. Due to the new design rules the varistor can withstand the switching losses and is able to dissipate the resulting heat to the surrounding medium. The investigation also led to

a better understanding of the mechanisms that allow to a reduction of the overvoltage at the machine terminal.

Mr. Purcarea dealt, in **TP5**, with different control strategies for the power switches of the inverter to reduce the voltage overload at the motor terminals. For that he did simplified time domain simulation models for inverter, cable and motor. The inverter point of view is the focus of his work, as it represents the source (dV/dt) of voltage overshoot at motor terminals via long cables. Cable and motor models are added to inverter model forming a single simulation system, where the HF-phenomena are calculated accurately. Measurement comparisons are presented to prove the reliability of chosen models. Mr. Purcarea designed and compared different types of inverter control strategies with passive filter applications and found that the filter variants are usually the solution with lower total losses.

Using finite element software, in **TP6**, Ms. Cay performed the extraction of parameters necessary in the simulation of inverter-fed drives. Ms. Cay performed electro-thermal computations using finite integration technique, modeling and simulation of rolling bearings and extractions of DC bus bar parasitics in PWM Inverters. She focused on the main tasks:

- a) FE simulation of simplified ball bearing models as an electrostatic circuit. She found a good coincidence with the simplified well-known lumped parameter circuits and the FE results;
- b) FE simulation of the electric field in varistors under step voltage surges. She combined the electrostatic field equations with the continuity equation of current flow and the non-linear dependence of the varistor permittivity on the electric field strength;
- c) FE simulation for the extraction of L-C-R-G parameters of printed circuit boards (PCB) for the trigger electronics of the electronic power switches of the inverter. She combined to different methods to calculate these parameters in good coincidence, which allow the design of low-inductive circuits for fast switching of the inverter power stage.

4. List of publications

1. O. Magdun, A. Binder, A. Rocks, O. Henze, "Prediction of common mode ground current in motors of inverter-based drive systems", Proceedings of Electromotion & ACEMP'07, 10-12 September, 2007, Bodrum, Turkey, pp.824-830
2. Lj. Petrovic, A. Binder, Cs. Deak, D. Irimie, K. Reichert, C. Purcarea: "Numerical Methods for Calculation of Eddy Current Losses in Permanent Magnets of Synchronous Machines", ISEF 2007, Prague, Czech Republic, September 2007, CD-ROM, 6 pages
3. A. Rocks, V. Hinrichsen, "Application of varistors for overvoltage protection of machine windings in inverter-fed drives", 6th IEEE International Symposium on Diagnostics for Electric Machines, Power Electronics and Drives, Cracow, Poland, September 6-8, 2007, CD-Rom, paper no. 112, 6 pages
4. A. Rocks, V. Hinrichsen, O. Henze, A. Binder, „Neuer Einsatz von Energievaristoren zum Überspannungsschutz an umrichtergespeisten Antrieben“, Tagungsband zum 12. Symposium Maritime Elektrotechnik, Elektronik und Informationstechnik, Rostock, 8 - 10 Oktober, 2007, pp. 233-238
5. A. Rocks, V. Hinrichsen, "Overvoltage Protection of inverter-fed drives with the help of energy varistors – dimensioning and lifetime considerations", IEEE APEC 2008, 24-28 February, 2008, Austin, Texas, pp.860-865.
6. Z. Çay, H. de Gersem, and T. Weiland, "Coupled electroquasistatic-thermal simulation using the finite integration technique", Proceedings of the 12th International IGTE Symposium on Numerical Field Calculation in Electrical Engineering, p. 91, 17-20 September, 2006 , Austria.

7. O. Henze, A. Rocks, H. De Gersem, T. Weiland, V. Hinrichsen, A. Binder, "A network model for inverter-fed induction-motor drives", EPE 2007, Aalborg, September 2007, 7 pages, CD-ROM
8. Z. Çay, O. Henze, and T. Weiland, "Modeling and Simulation of Rolling Element Bearings in Inverter-fed AC Motors", Proceedings of SPEEDAM'08, 11-13 June, 2008, Italy. pp. 1333-1336.
9. O. Henze, Z. Cay, O. Magdun, H. De Gersem, T. Weiland and A. Binder, "A Stator Coil Model for Studying High-Frequency Effects in Induction Motors , SPEEDAM'08, Italy, pp. 609 - 613
10. A. Rocks, V. Hinrichsen, „Effect of varistors for overvoltage protection in inverter-fed drives on the voltage distribution in the stator winding“, ISEI 2008, International Symposium on Electrical Insulation, Vancouver, 8-11 Juni 2008, pp. 624-627
11. Z. Cay, O. Henze and T. Weiland, "Extraction of DC Busbar Parasitics in PWM Inverters", Proceedings of the 13th International IGTE Symposium on Numerical Field Calculation in Electrical Engineering, pp. 212-217, 22-24 September, 2008, Austria.
12. A. Rocks, V. Hinrichsen, "Overvoltage protection of inverter-fed drives with the help of energy varistors - Dimensioning rules for consideration of different cable types", IEEE Applied Power Electronics Conference and Exposition 2009, Washington DC, 24-28 Februar 2009, pp.860-865
13. A. Rocks, V. Hinrichsen, „Metalloxidvaristoren als Überspannungsschutz für pulsumrichtergespeiste Drehfeldmaschinen“ ETG-Workshop „Isoliersysteme bei repetierenden impulsförmigen Beanspruchungen“, Hannover, Juli 2009 (to be published)
14. A. Rocks, V. Hinrichsen, „Betriebs- und Alterungsverhalten von Metalloxidvaristoren zum Überspannungsschutz pul-sumrichtergespeister Drehfeldmaschinen“, RCC-Fachtagung "Werkstoffe", Berlin, 6.-7. Mai 2009, pp. 207-215
15. A. Rocks, V. Hinrichsen, "Accelerated ageing test for metal-oxide varistors used for overvoltage protection in inverter-fed drives", ISH 2009, Kapstadt, Südafrika, 24- 28 August 2009, 6 pages, CD-ROM.
16. C. Purcarea, P. Mutschler, O. Magdun, A. Rocks and A. Binder, "Time domain simulation models for inverter-cable-motor system in electrical drives", EPE'09, Barcelona, September 2009, 10 pages, CD-ROM.
17. O. Magdun, A. Binder, C. Purcarea, A. Rocks, "High-Frequency Induction Machine Models for Calculation and Prediction of Common Mode Stator Ground Currents in Electric Drive Systems, EPE'09, Barcelona, September 2009, 8 pages, CD-ROM.
18. O. Magdun, A. Binder, C. Purcarea, A. Rocks, B. Funieru, "Modeling of Asymmetrical Cables for an Accurate Calculation of Common Mode Ground Currents", ICCE'09, San Jose, USA September 2009, 8 pages, CD-ROM.
19. O. Magdun, A. Binder, "Calculation of Roller and Ball Bearing Capacitances and Prediction of EDM Currents, IECON '09, Porto, November 2009, 6 pages, CD-ROM.
20. C. Purcarea, P. Mutschler, "Investigation of EMI reduction techniques using time domain simulation of drives," IECON'09, Porto, November 2009, 6 pages, CD-ROM.
21. C. Purcarea, J. Kedarisetti, P. Mutschler, "A Motor-Friendly and Efficient Resonant DC-link Converter", EPE'09, Barcelona, September 2009, 6 pages, CD-ROM.
22. Z. Çay, O. Henze, S. Koch, T. Weiland, "Modeling and extraction of parasitics in IGBT modules", Proceedings of the 16th Conference on the Computation of Electromagnetic Fields (COMPUMAG), Florianopolis, Brazil, 22-26 November, 2009 (to be published)
23. O. Henze, S. Koch, H. De Gersem, T. Weiland, "A 3D-Coil Model for Bearing Current Analysis of Inverter-fed Drives", EPE 2009, Barcelona, September 2009, 6-pages, CD-ROM
24. A. Rocks, *Einsatz von Metalloxid-Varistoren zum Überspannungsschutz pulsumrichtergespeister Drehfeldmaschinen*, PhD-thesis, submitted September 2009, TU Darmstadt

5. Subproject 1: Calculation of Parasitic High Frequency Current Distribution in Inverter-Fed Electrical Machines

Prof. Dr.-Ing. habil. Dr.h.c. Andreas Binder

Dipl.-Ing. Oliver Magdun

Institut für Elektrische Energiewandlung, TU Darmstadt

E-Mail: omagdun@ew.tu-darmstadt.de

5.1. Introduction

During normal operation, the electrical machines fed by fast switching inverters suffer from bearing damages [1]. A literature survey [2] has pointed out a percent of bearing failures bigger than 30% of the total machine failures. The reason of premature multiple bearing failures in the induction motors supplied by switching frequency inverters is the voltage and current stress directed to bearings. The physical explanation of the different bearing phenomena has been largely done in [3] related to the measurements and practical experiments. Four types of parasitic high frequency (HF) bearing currents have been described: capacitive currents, which are very small and usually not harmful, rotor ground currents, which may reach a considerable magnitude when the motor is grounded via the driven load, electric discharge machining (EDM) currents and circulating bearing (CB) currents which are induced by the magnetic field of the HF common mode ground current. It has been reported in [3] that the EDM currents occur already in small motors, whereas the HF circulating bearing currents are generated in bigger machines, typically above 100 kW. They are the most important destructive currents of bearings. The HF stator ground common mode (CM) current flows through the cable, the motor stator windings, via the stray capacitance between the stator windings, the motor frame and the ground back to the inverter frame, producing also an electromagnetic interference with electronic equipment. The HF stator ground CM current does not pass via the bearings, but causes the CB currents via induction when the inductive coupling common mode flux is big enough. The present report is focused on the accurate calculation of the CM stator ground currents. In [4], an equivalent transformer circuit was used to calculate the CB currents, using the CM current as a current source. Hence, the calculation of the CM current has allowed the calculation of the CB currents. The results of CB current calculation have been presented in the *DFG-Intermediate Report 2008*.

Generally, for the calculation of the CM current, CM equivalent circuit models of the electric machines are used, where a calculated or measured CM voltage is applied at the input [5], [6]. As a difference, in our research the CM currents are calculated more accurately, by the use of models per phase having the line-to-earth voltages as input, with parameters identified experimentally, analytically and by finite element methods (FEM):

- a) Simplified HF equivalent circuits models with constant parameters determined by experiments;
- b) Transmission line models with constant parameters, which are calculated analytically;
- c) Distributed HF equivalent circuit models with parameters calculated by FEM, which depend on the frequency in order to obtain a better modeling of the skin and proximity effects for the stator coil conductors within the slots and in the iron vicinity.

With the HF models of the induction motor of b) and c), the CM current may be estimated even in the design stage and its effects can be reduced by a proper winding arrangement. The HF models of a) can be used for the best design of the CM current filters, for the calculation of the CB currents, using the transformer model of [4] and for the prediction of the bearing voltages and EDM currents, considering the capacitive coupling mechanism (*DFG-Annual Report 2006*).

5.2. Simplified HF equivalent circuits for CM current calculation

5.2.1. LCR series circuits

Suitable for the analysis in the time domain, a LCR series resonant circuit has been proposed in [5] to compute the common mode ground current. Due to the damping factor ξ , $0 < \xi < 1$, when a step voltage V is applied to the circuit terminals, the common mode ground current has been found as having the expression:

$$i_{\text{com}} \cong \frac{V}{Z_0} \cdot e^{-\xi \cdot \omega_n \cdot t} \cdot \sin(\omega_n \cdot t) \quad (5.1)$$

where $\omega_n = \frac{1}{\sqrt{LC}}$ is the natural angular frequency, $\xi = \frac{R}{2} \cdot \sqrt{\frac{C}{L}}$ is the damping factor and

$Z_0 = \sqrt{\frac{L}{C}}$ is the characteristic impedance. A method to calculate analytically the parameters of the circuit R , C and L from the winding data or from the impedance-frequency characteristics was missing. The parameters were determined only comparing the calculated CM current waveform with the experimentally measured waveform by different software [5], [6]. But, the LCR series circuits did not always produce satisfactory results, because they consider only the motor parameters like the stator winding-to-stator frame capacitance C_g , the frame resistance R_g and an inductance L , identified at the natural oscillation frequency $f_n = \omega_n / 2\pi$ (1). However, the results obtained in an experimental research program [3] that included several inverters and motors with different power levels and numerous cables and filters, showed CM current waveforms far away from the CM current waveforms computed by (1) for a power level less or equal to 110 kW. For example, we have measured the CM ground current for an induction motor of 7.5 kW, when a long 4-conductor unshielded cable of 100 m (Fig. 12) is used to connect the motor to the inverter. The CM current waveform (Fig. 1b) shows deviations from (1). The line-to-earth voltage at the motor terminals is not a pure step voltage, but it is oscillating due to the wave reflection at the motor terminals. This phenomenon has been considered for an accurate representation of the unshielded cable of Fig. 12 in Section 5.6.

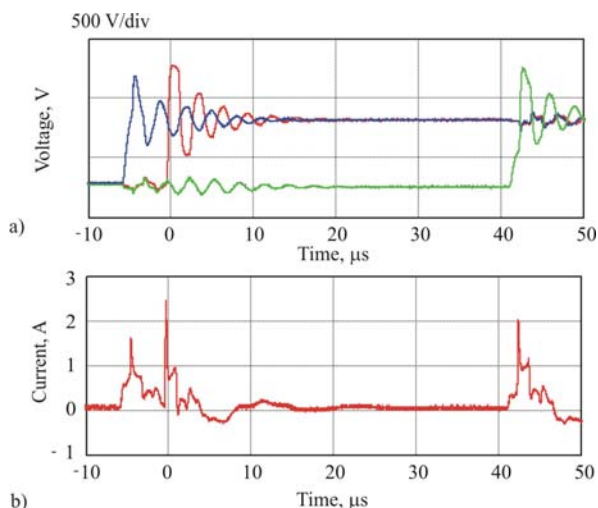


Fig. 1. Measurements effectuated on a 7.5 kW induction motor: (a) - measured voltages at operation with 100 m unshielded motor cable, DC link voltage 560V, 3 kHz switching frequency, (b) - measured common mode ground current

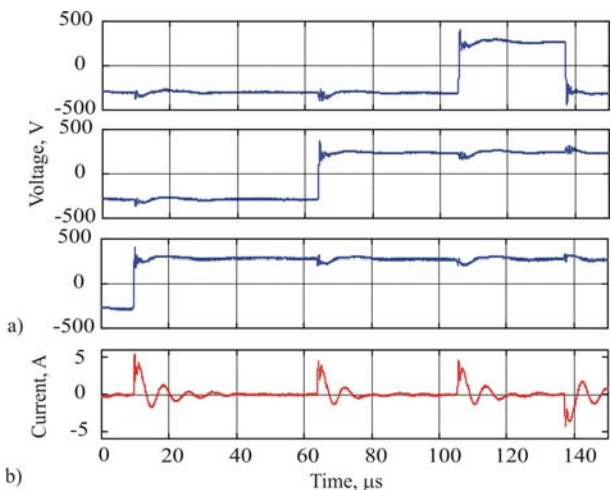


Fig. 2. Measurements effectuated on a 240 kW induction motor: (a) - measured voltages at operation with 2 m unshielded motor cable, DC link voltage 560V, 4 kHz switching frequency, (b) - measured common mode ground current

The method of [6] is simple and practically and can be used for the modelling of big induction motors (Fig. 2b). We have obtained a CM current waveform described by (1) for a motor of 240 kW, when the cable length between inverter and motor is less than 1-2 m and the line-to-earth voltage applied at the motor terminals is a step voltage (Fig. 2a). Similar results have been reported in [3] for different big power levels of the motors around 500 kW.

5.2.2. Simplified HF circuit models for a large frequency spectrum up to 10 MHz

With the simplified representation of Fig. 3a, the LCR series circuits do not consider a correct behavior of the common mode motor impedance for the entire relevant frequency spectrum between 1 kHz...10 MHz. Therefore, models available for this large frequency spectrum must be used instead of the lumped RLC circuit models. Due to its convenient and efficient parameterization, a simplified high frequency (SHF) circuit model of induction machines for the time and frequency domain simulation (Fig. 3b), proposed in [7], is chosen as one possibility to calculate the CM currents. The estimation of the SHF circuit parameters of induction motors may follow rules well established in [7], but which require measurements of the CM and DM (Differential Mode) impedance in dependence of the frequency up to 10 MHz.

In Fig. 3b the parasitic capacitances between the stator winding and the frame C_{g1} and C_{g2} and the corresponding resistances R_{g1} and R_{g2} of the CM current paths are shown together with the winding phase inductance L . The iron losses are represented by R_e and the I^2R -losses by R . Stray inductances and resistances of external and internal connector lines are considered by L_c and R_c . The SHF circuit was verified in [7] with good results regarding the frequency characteristics, for several machines with a rated power up to 45 kW. We checked the SHF circuit for the two machines, a small 4 pole squirrel cage induction machine (single layer, wound wire winding) 7.5 kW (Fig. 4a) and a bigger one 240 kW with two-layer profile copper winding (Fig. 4b). A good agreement between the measured and calculated CM and DM winding impedance between 1 kHz and 10 MHz has been found. In Fig. 4a and 4b, with bold lines (red and blue) are represented the calculated CM and DM impedance characteristics, when the parameters of Table 1 are used. The points "+" are the measured values for the CM and DM setup. Unfortunately, this method needs in addition a method for the parameters calculation of the SHF circuit model in the design stage as it is based on measured quantities.

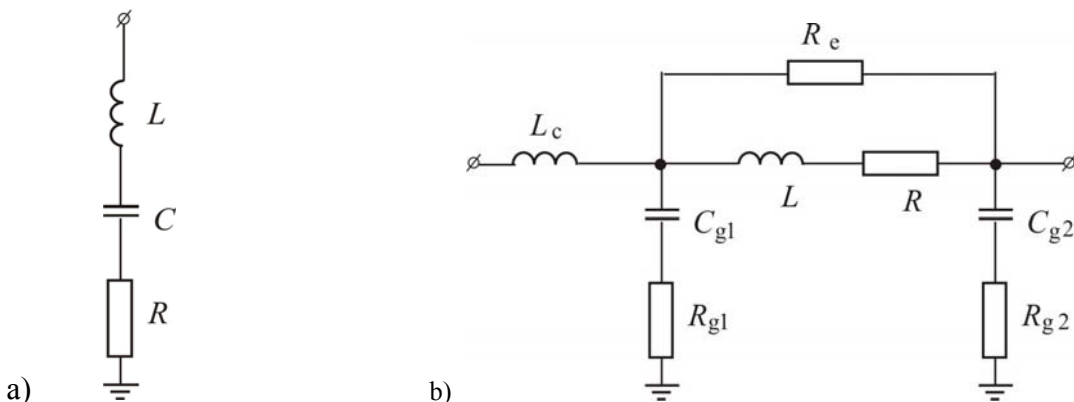


Fig. 3. Simplified equivalent HF circuit models per phase of an induction machine:
a) - lumped RLC circuit model, b) – Simplified HF (SHF) model proposed in [7]

Table 1: Equivalent circuit parameters for the SHF model of [7] determined from measurement

P_N kW	U_N V	C_{g1} nF	R_{g1} Ω	L_c μH	C_{g2} nF	R_{g2} Ω	L mH	R Ω	R_e Ω
7.5	400	0.53	3	0.5	2.83	30	1	5	1500
240	1375	1.12	15.07	0.6	10.55	4.07	0.15	5	533.3

5.3. Transmission line models with constant parameters

In the design stage, as an alternative to the SHF circuit model, methods which consider ladder circuit models of the stator winding including the stator slot area must be applied to predict the CM currents [8]. However, treating the stator winding as a simple RLC lumped circuit, the travelling wave phenomenon within the winding is neglected. Hence, the winding transient phenomena is neglected. In a study of the voltage distribution in the stator winding of an induction machine [9], it is clearly indicated that the stator winding of the induction machine at very high frequency must be treated as a transmission line. Models for windings have been used for the surge phenomena theory in electrical machines e.g. to predict consequences of lighting surges [10], [11].

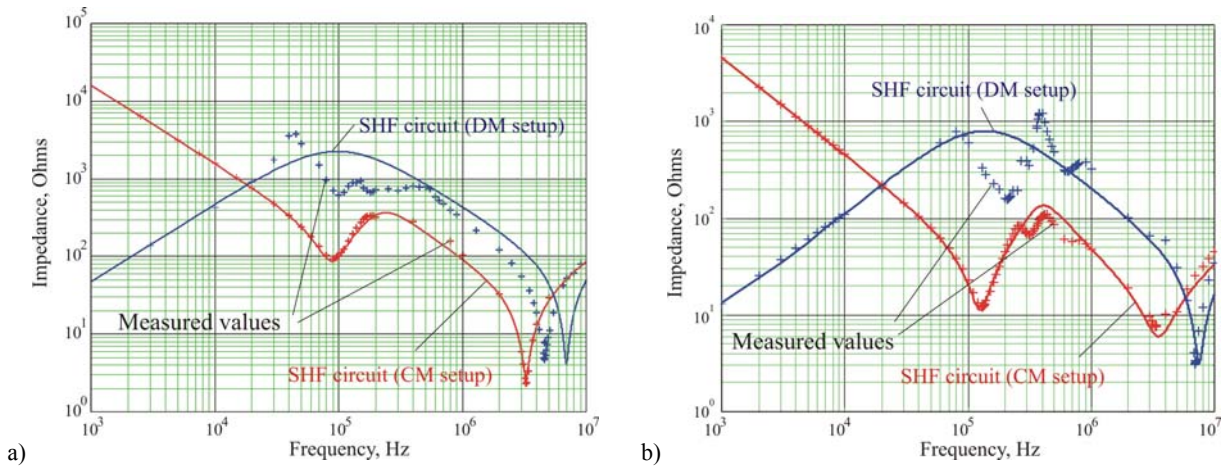


Fig. 4. Measured and calculated CM and DM winding impedance characteristics of 4 pole cage induction machines:
a) - 7.5 kW oval shape semi-closed stator slots, single layer wound wire winding,
b) – 240 kW rectangular open stator slots, two-layer profile copper winding

The most important assumption at high frequency in the MHz range, already mentioned, is that the magnetic field does not penetrate the stator and rotor core [14]. Also, the electric field energy is enclosed inside the slots and the air gap. The distortion effect of the iron core due to iron saturation on travelling waves in the slot is neglected. Considering the iron core as an impenetrable wall for the HF magnetic flux due to the eddy currents in the iron sheets, and the insulation as an uniform perfect dielectric layer inside of the slots ($\epsilon = \epsilon_0 \cdot \epsilon_r$), the velocity of wave propagation is taken to be $v_c = \frac{c_0}{\sqrt{\epsilon_r}}$. With $\epsilon_r \approx 4$ this velocity is half of the velocity of light in vacuum c_0 . The rise time t_r of the voltage $u(t)$ at the inverter due to the fast switching IGBT converter is typically less than 50 ... 200 ns and at the motor terminal 200 ... 300 ns (Fig. 1). It is converted to an equivalent sine wave frequency $f_e = \frac{1}{\pi \cdot t_r} \approx 1 \div 1.6 \text{ MHz}$ and a

corresponding wavelength $\lambda = v_c/f_e \approx 90 \div 150$ m. The value of λ is big enough to approximate the winding according to the transmission line theory, as a ladder circuit with only few Γ -sections in series. Each Γ -section is constituted by ΔR , ΔL , ΔC_s and ΔC_{ws} according to Fig. 5. However, the wire length of one turn in small and medium power AC machines is much smaller than the wavelength λ . So, a model of the stator winding per phase with a number of Γ -sections equal to the number of turn per phase N_s seems to be more appropriate. By considering all turns in the model, the windings with more branches in parallel can be also modeled properly. Due to the strong current displacement effect of the iron core, the mutual coupling between the slot portions of coils in adjacent slots can be assumed to be negligible. The magnetic coupling of the end winding per turn is rather weak, compared to the coupling between conductors within the same slot, and is therefore also neglected [11]. A more complex model for the CM ground current computation is considering this coupling [12]. In order to simplify the parameter calculus, the assumptions from the transmission line theory for considering the travelling wave phenomena are accepted.

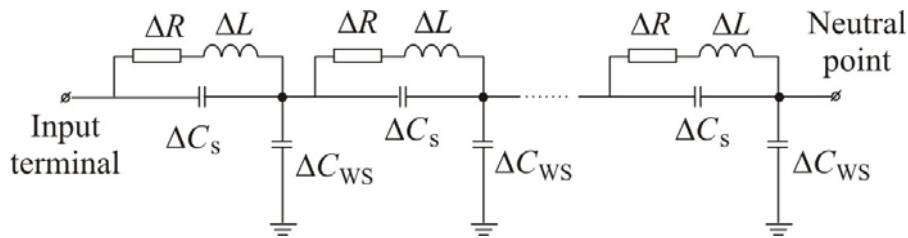


Fig. 5. Equivalent circuit of a stator winding (ΔR , ΔL are the resistance and inductance per turn, ΔC_s is the capacitance between two turns and ΔC_{ws} is the stator winding – frame capacitance per turn of one stator phase)

The equivalent circuit parameters of each turn, ΔR - the resistance per turn, ΔL - the inductance per turn, ΔC_{ws} – the capacitance between turn and iron stack, are calculated analytically [3] for two cage induction motors of 110 kW, $2p = 4$: a single layer winding with two parallel branches ($\Delta R = 2.4 \Omega / \text{turn}$, $\Delta L = 2 \mu\text{H} / \text{turn}$, $\Delta C_{ws} = 0.33 \text{ nF} / \text{turn}$) and two layer winding with four parallel branches ($\Delta R = 7 \Omega / \text{turn}$, $\Delta L = 3.2 \mu\text{H} / \text{turn}$, $\Delta C_{ws} = 0.202 \text{ nF} / \text{turn}$). The capacitance ΔC_s between two turns is neglected, as its influence is big only at the very first moment after the switching occurs. The analytical calculation of the parameters was checked numerically by the authors with FEM and the calculated CM current waveforms have been presented in [13] and the *DFG Annual Report 2007*.

With the TL equivalent circuit model of Fig. 5, the peak value of the CM ground current has been determined for the two motors with 10-15 % percent, plus or minus, in comparison with measurements. But, for the small motors in the range of 10 kW, the peak value of the CM current is not correctly predicted with TL equivalent circuit models. Thus, more refined distributed models (Fig. 6) close to the real case are required.

5.4. Distributed HF equivalent circuit models

The parameters of the refined distributed winding models (Fig. 6) are derived by computation with FEM. Two different analysis techniques are performed [14]:

- a) An electrostatic analysis to calculate the electric field and the corresponding capacitances in dependence of the decrease of the electric permittivity, when frequency increases [15];
- b) A harmonic AC analysis to calculate the magnetic field and losses at different frequencies. An improvement of the results is obtained, if a correct iron core representation at HF is done [16].

5.4.1. Distributed HF models for sinusoidal analysis

The number of necessary circuit elements for the refined DHF circuit (Fig. 6a) is very big. As an example, for the 7.5 kW motor winding it is around of 500 elements per phase. A numerical program was written in order to generate directly for a SPICE analysis, from the energy values calculated by FEM, the resistances, inductances and capacitances of the DHF circuit at any imposed frequency. The CM current is calculated as a superposition of those sinusoidal currents, which result from the AC SPICE analysis of the circuit, when the sinusoidal voltage sources with different frequencies obtained by the *Fourier* decomposition of the input CM voltage are applied at the circuit input.

5.4.2. Transmission line models derived from the DHF models with RL ladder circuits for HF effect consideration

To simplify the prediction methodology of the CM current, a reduced model of Fig. 6b is proposed. This model is represented turn by turn of the coils of the winding per phase. For each turn, the skin and proximity effects are considered by the use of RL ladder circuits (Fig. 10a) instead of a single RL branch. Accordingly the resistances and inductances per turn depend on frequency and are described by RL ladder circuits: $R_{1T} = R_{1T}(f)$ and $L_{1T} = L_{1T}(f)$. The capacitances of the circuit are calculated for a relative permittivity $\epsilon_r = 2$ of the slot insulation [9].

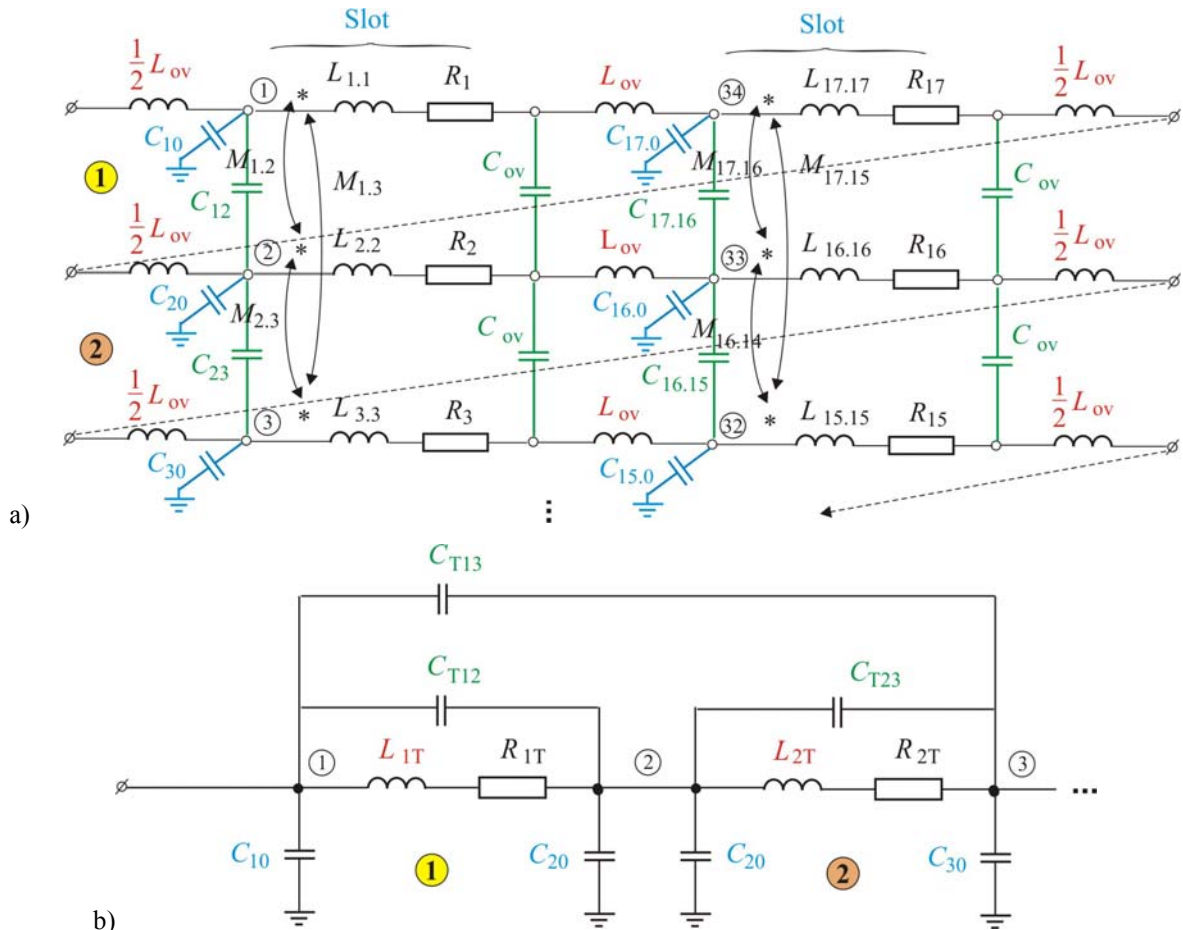


Fig. 6. Distributed equivalent HF circuit models per phase of an induction machine:
a) – a particular part of the distributed HF (DHF) model corresponding to a single layer winding with 17 turns per slot,
b) - transmission line model derived from the DHF model, with RL ladder circuits for all the pairs R_{1T} , L_{1T} , R_{2T} , L_{2T} , ... for the consideration of HF effects

To verify the model of Fig. 6b, the winding of a 7.5 kW induction motor was prepared by our industrial partner, *Johannes Hübner Company, Giessen*, (Mr. Ohl) with connections to each series coil per phase to be accessible for the parameter measurement of the series coils per phase (see *TP4-Hinrichsen*). The measured resistance and inductance of a coil are divided by the number of turns per coil $N_c = 17$ to get the average values of resistances and inductances per turn (Fig. 7a and 7b).

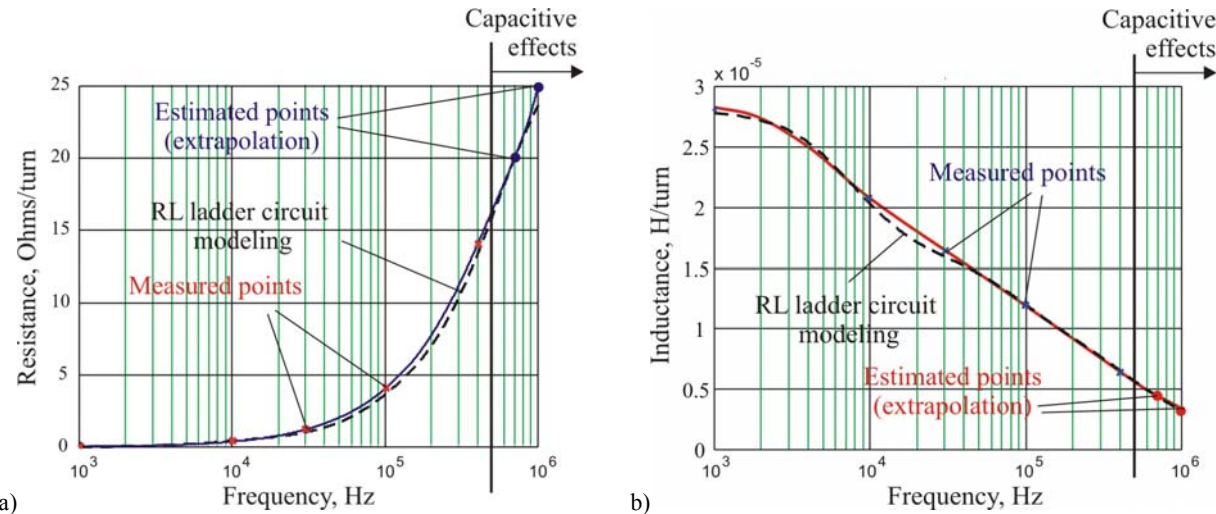


Fig. 7. Measured and calculated average values of the resistance and inductance per turn of a 7.5 kW cage induction motor

Due to of the series and ground capacities of the winding, the measurements showed has several resonance frequencies. So the measured values of the inductance and resistance are considered only up to the first resonance frequency [10]. The resonance frequency has been measured at 450 kHz for the stator coils of the 7.5 kW induction motor. The resistances and inductances at frequencies bigger than 450 kHz are taken by extrapolation. The resistances and inductances modelled by 6 RL ladder elements are represented with dashed lines. Different measurements for different configuration setups have shown that for small machines there is a short spike of the CM current in the very first moment of the voltage switching [3]. Consequently, when the CM current is predicted for small motors, a RC circuit (Fig. 3a), with $R = R_{g1}$ and $C = C_{g1}$ calculated for HF bigger than 1MHz, should be added in parallel to the circuit from Fig. 6b. For big motors, the frame resistance R and the stator winding-to-stator frame capacitance C are relative big and the first spike of the CM current may not occur.

5.5. CM current calculation

At each voltage step (Fig. 8a) of the DC link voltage at the motor terminals, which is caused by the switching of the inverter as a voltage source and the voltage reflection at the motor terminals, a ground current impulse (Fig. 8b) is generated. The CM current is constituted by the superposition of all the generated impulses. Hence, in Fig. 8b and 8c, only one measured CM current impulse for the 7.5 kW induction motor (Fig. 4a) is presented in comparison with the calculated ones by the SHF and DHF circuits respectively, showing good results for the circuits of Fig. 3b and 6b during the first 5 μ s, whereas the results from the circuits of Fig. 3a and 6b differ from measurements. For a larger time scale, only the circuit of Fig. 3b coincides with measurements.

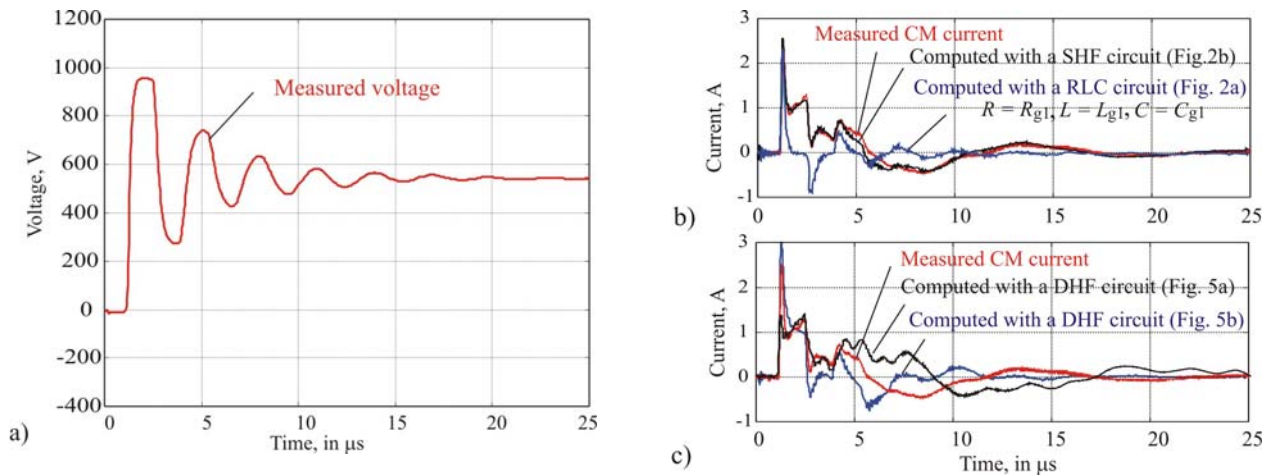


Fig. 8. 7.5 kW induction motor, motor cable length 100 m, DC link voltage 560V, 3 kHz switching frequency
 a) - Measured line-to-earth voltage, b) - CM current calculated with SHF and RLC lumped circuits,
 c) - CM current calculated with DHF circuits

In this section, the CM current has been calculated by the use of measured line-to-earth voltages at the motor terminals. To consider the voltage from the inverter output terminals in the simulation, an accurate model of the unshielded cable must be used, which is described next.

5.6. Cable modeling

The cable is the guideway of the voltage impulses that travel with about half of the vacuum velocity of light from inverter to motor, and by reflection back to the inverter in a repeated process forward-backward. The voltage steps at the inverter output terminals with a maximum constant value equal to the DC link voltage become an oscillating voltage with an amplitude of nearly twice DC link voltage, if the ratio of motor versus cable wave impedance is very big. The oscillating voltage and the resulting CM current may be calculated by the use of the cable equivalent circuit models containing those cable parameters.

5.6.1. Cable models

The earlier cable models proposed in the literature [17] are based on the transmission line theory. They consider a series of equivalent circuits (Fig. 9a or Fig. 9b) connected like in Fig. 10, having constant parameters per unit length of each section, which can be evaluated by measurements or calculated by FEM [18], [19]. The proposed methodologies for the modeling of the cable parameter variation with the frequency use ladder circuit networks (Fig. 10) implemented inside of each elementary section of Fig. 9b. Since the analytical evaluation of the ladder circuit parameters was only developed for simple geometries of cable conductors [20], a more practically methodology which requires the measured cable parameters for the entire frequency spectrum was proposed in [21] to identify the RL-ladder circuit parameters (Fig. 10a). This methodology may be used also, when the cable parameters are determined by FEM. In this research the algorithm given in [21], which allows a convenient way to calculate the parameters of the RL-ladder circuit (Fig. 10a), has been extended to the calculation of the CG-ladder circuit parameters (Fig. 10b). If the ladder circuits of Fig. 10 are connected as in Fig. 12, the cable model may be used for the prediction of the cable behavior also at HF, e.g. at frequency of 100 MHz [22].

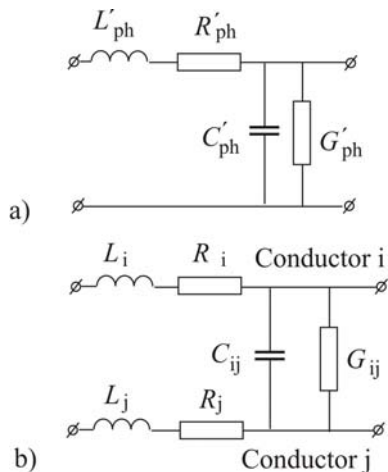


Fig. 9. Equivalent circuit elements for modeling of cables: a) - Γ - section, b) - Elementary section for representation of two cable conductors

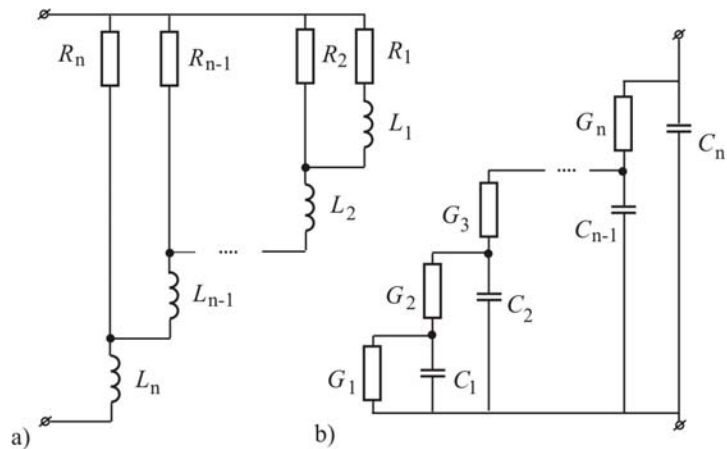


Fig. 10. Ladder circuits for modeling of cables at a high frequency:
a) – RL-ladder circuit, b) – CG-ladder circuit

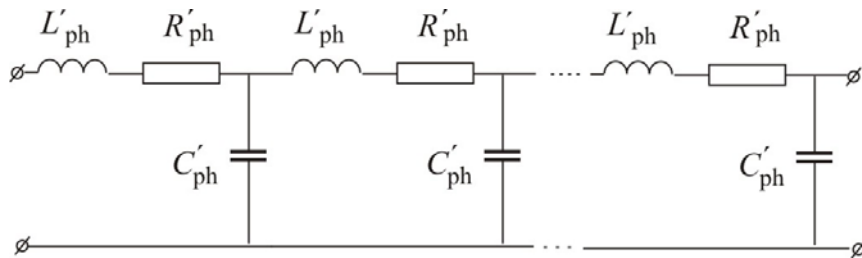


Fig. 11. Cascaded RLC Γ -sections for modeling of cables

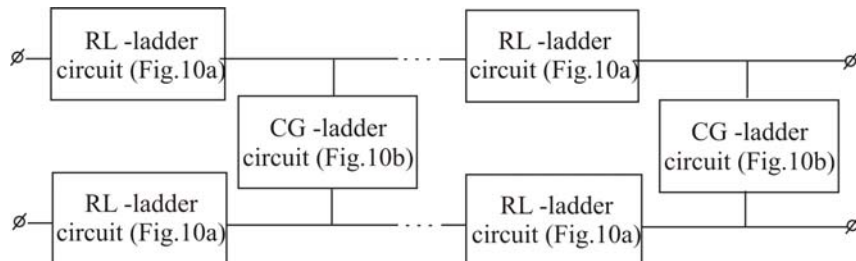


Fig. 12. Network ladder circuits for cable modeling

5.6.2. Evaluation of cable parameters

An asymmetrical unshielded cable PURWIL 4 x 6 mm² with the cross-section given in Fig. 13 is investigated. Via an RLC-meter, the methods proposed in the literature [19], [22], [23] are used to measure the cable parameters, which are compared to the calculated ones by FEM (Fig. 14 and 5.14). Applying the algorithm from [21], the equivalent circuit parameters of Fig. 12 are found (Table 3 and 4). In *TP4-Hinrichsen*, a run time-impulse method has been used to determine the cable parameters per phase L'_{ph} and C'_{ph} (Table 2). They result from measurements, when a rectangular pulse train of 10 kHz is applied at the cable input terminals. The voltage reflection at the cable output terminals is eliminated by a potentiometer resistance equal to the cable wave impedance ($Z_t = Z_c$). To compare the results, the capacitances of the 4-conductor cable (Fig. 13) can be calculated by the mirror images method, and the self and mutual inductance for a 4-conductor cable are calculated analytically by relations adapted from [24] (see *TP5-Mutschler*).

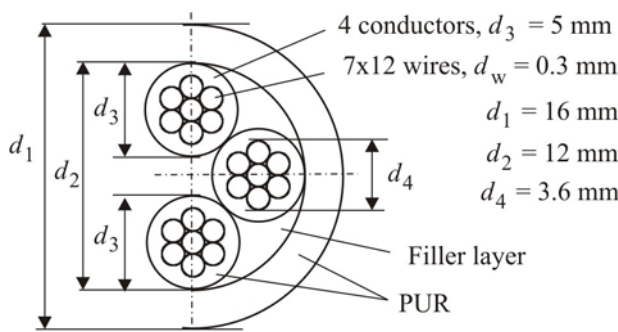


Fig. 13. Cross-section of a PURWIL 4 x 6 mm² unshielded cable

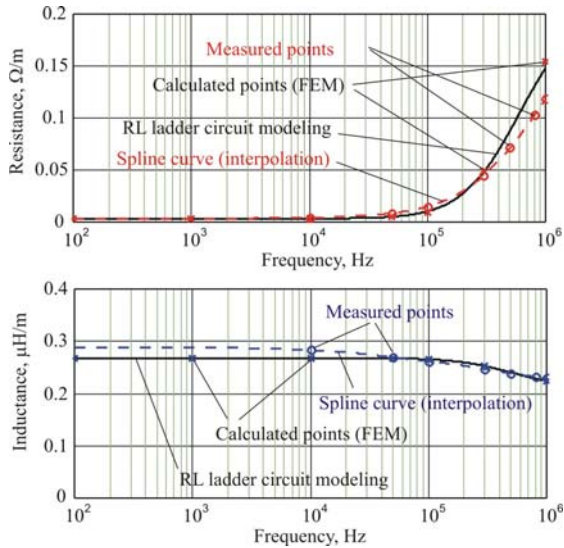


Fig. 14: Measured and calculated resistance R_1 and inductance L_1 (Fig. 10b) for the cable of Fig. 13

Table 3: RL-Ladder circuit parameters for the cable of Fig. 13, which are used in Fig. 10

n	1	2	3	4	5	6
R_n mΩ/m	545.48	545.51	73.557	4.397	18.278	201.19
L_n nH/m	0.0378	436.65	51.472	7.747	53.782	210.83

Table 2: Measured parameters v_c , Z_c by the run-time impulse method and calculated parameters L'_{ph} , C'_{ph} for the cable of Fig. 11, $l_c = 100$ m (see TP4-Hinrichsen)

l_c m	Z_c Ω/m	v_c m/μs	L'_{ph} μH/m	C'_{ph} pF/m
100	71	158	0.45	89

$$v_c \cong 1/\sqrt{L'_{ph} \cdot C'_{ph}}, Z_c \cong \sqrt{L'_{ph}/C'_{ph}}$$

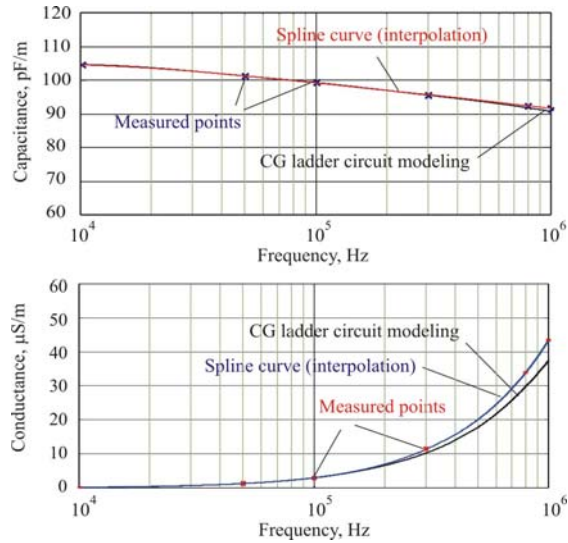


Fig. 15: Measured and calculated capacitance and conductance for the cable of Fig. 13

Table 4: CG-Ladder circuit parameters for the cable of Fig. 13, which are used in Fig. 10

n	1	2	3	4	5	6
C_n pF/m	0.0088	2.81	4.187	4.067	10.497	83.81
G_n μS/m	0.0108	0.0109	0.663	5.106	19.804	122.29

5.6.3. CM current calculation

The CM current is calculated using both the equivalent circuit of Fig. 11, which is done by the Γ -equivalent circuits Fig. 9a, and the equivalent circuit of Fig. 12, which is done by the ladder network circuits Fig. 10a and 10b. A HF model of a 7.5 kW induction motor (Fig. 3b) is added at the end of the cable model. Two cases for CM current calculation are presented, when the circuit of Fig. 11 is used:

a) The circuit parameters are taken by the spline extrapolation at 10 MHz of the parameter values calculated by FEM (Fig. 14 and 15) $R'_{ph} = 2 \cdot R_1 = 0.72 \Omega/m$, $L'_{ph} = 2 \cdot L_1 = 0.4 \mu H/m$, $C'_{ph} = 84 \text{ pF/m}$.

b) Between 1 MHz and 10 MHz, the capacitance and inductance per phase do not change significantly; the calculation is done as example for the cable parameters at 1 MHz, with the same

capacitance and inductance from a), but with a much smaller resistance $R'_{ph}=0.3 \Omega/m$ as the resistance is decreased.

When an imposed trapezoidal voltage is applied at the cable entry terminals, the calculated CM current (Fig. 16b) is relative close to the measured one for each case a) or b), but the line-to-earth voltage at the motor input terminals (Fig. 16a) is not well predicted. To obtain a correct line-to-earth voltage calculation, the circuit of Fig. 12 must be used instead of the circuit of Fig. 11. In this case the CM current is also calculated with better accuracy (Fig. 16b).

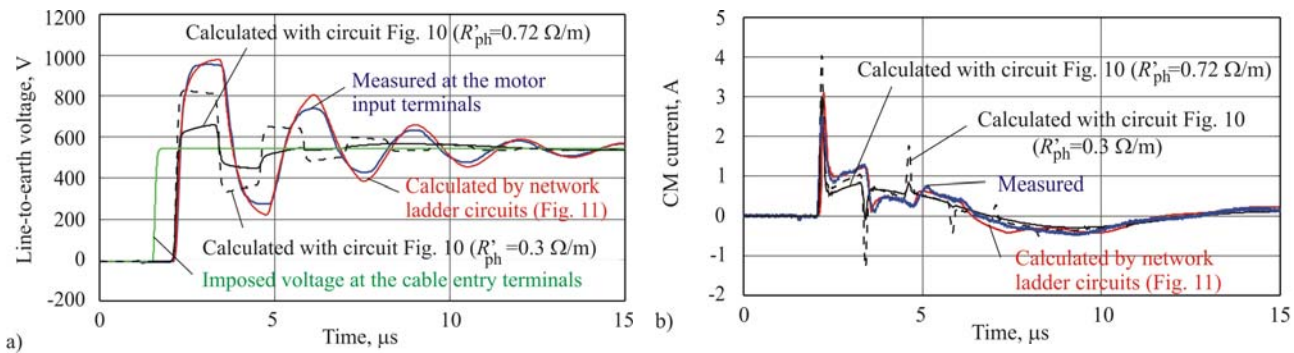


Fig. 16. Measured and calculated: a) - line-to-earth voltages at the motor input terminals and b) - CM currents for a 7.5 kW induction motor drive

5.7. Conclusion

The SHF circuit of the induction motors may be used for an exact preliminary calculation of CM currents for motors, which are already manufactured. The DHF circuits are recommended only for the prediction of CM currents in the design stage. The first spike of the CM current can only be determined exactly with DHF circuits with an additional RLC-branch at the entrance. This effect occurs especially with smaller motors used with long motor cables.

The cable has a strong influence on the line-to-earth voltage at the motor terminals and consequently on the CM current, which occurs in AC electric drive systems. The CM current can be well calculated if the cables are modelled either by cascaded RLC circuits or by network ladder circuits. But the line-to-earth voltage at the motor terminals may be calculated accurately only by network ladder circuit models of the cable. The cascaded RLC circuits have the advantage of their simplicity, compared to the network ladder circuits, which requires different algorithms for the calculation of the frequency-dependent cable parameters. The cable parameters can be simply measured by RLC-meter devices, or they may be calculated either by FEM or analytically. The parameters of the cascaded RLC circuits may be measured from the run-time parameters of the impulse propagation along the cable.

References

- [1] D. Busse, J. Erdman, R. Kerkman, D. Schlegel, G. Skibinski, "System Electrical Parameters and their Influence Effect on Bearing Currents", IEEE Transaction on Industry Application, vol. 32, pp. 21-32, 1997
- [2] H. Toliyat, G. Kliman, *Handbook of Electric Motors*, CRC Press, New York, 2004
- [3] A. Muetze, *Bearing Currents in Inverter-Fed AC Motors*, Ph.D. thesis, Darmstadt Univ. of Technology, Shaker Verlag, Aachen 2004.
- [4] A. Muetze, A. Binder, "Calculation of Circulating Bearing Currents in Machines of Inverter-Based Drive Systems", IEEE Transactions on Industrial Electronics, vol. 54, no. 2, pp. 932-938, April 2007.
- [5] S. Chen, T. Lipo, D. Fitzgerald, „Modeling of Motor Bearing Currents in PWM Inverter Drives“, IEEE Transaction on Industry Applications, vol.32, no. 6, pp.1365-1370, November/December 1996
- [6] S. Ogasawara, H. Akagi, "Modeling and Damping of High-Frequency Leakage Currents in PWM Inverter-Fed AC Motor Drive Systems", IEEE Transactions on Industry Applications, vol. 32, no. 5, pp. 29-36, September/October 1996.

- [7] M. Schinkel, S. Weber, S. Guttowski, W. John, H. Reichl, "Efficient HF modeling and model parameterization of induction machines for time and frequency domain simulations", Proceedings of APEC '06, pp. 1181-1186, 19-23 March 2006, Dallas, USA.
- [8] E. Zhong, T. Lipo, "Improvements in EMC Performance of Inverter-Fed Motor Drives", IEEE Transaction on Industry Applications, vol. 31, no. 6, pp. 1247-1256, November/December 1995.
- [9] B. S. Oyegoke, "Voltage distribution in the stator winding of an induction motor following a voltage source", Electrical Engineering, vol. 82, pp. 199 – 205, 2000.
- [10] M. T. Wright, S. J. Yang, K. McLeay, "General Theory of Fast-Fronted Interturn Voltage Distribution in Electrical Machine Windings", IEE Proceedings, vol.130, Pt. B, no. 4, pp. 245-256, July 1983.
- [11] S. G. Suresh, H. A. Tolyat, D. A. Rensdussara, P. N. Enjeti, "Predicting the Transient Effects of PWM Voltage Waveform on the Stator Windings of Random Wound Induction Motors", IEEE Transaction on Power Electronic, vol. 14, Issue 1, pp. 135-141, Jan. 1999.
- [12] P. J. Tavner, R. J. Jackson, "Coupling of discharge currents between conductors of electrical machines owing to laminated steel core", IEE Proceeding, Pt. B, vol. 135, no. 6, pp. 84-90, November 1988.
- [13] O. Magdun, A. Binder, A. Rocks, O. Henze, "Prediction of common mode ground current in motors of inverter-based drive systems", Proceedings of ACEMP'07, pp.806-811, Bodrum, Turkey, 10-12 September 2007.
- [14] R. Asensi, J.A. Cobos, O. Garcia, R. Prieto, J. Uceda, "A full procedure to model high frequency transformer windings", Proceedings of PESC '96, vol.2, pp.856-863, 20-25 June 1996, Taipei, Taiwan.
- [15] F. Clark, *Insulating Materials for Design and Engineering Practice*, John Wiley & Sons, New York, 1962.
- [16] E. Bjerkan, *High frequency modeling of power transformers*, Ph.D. thesis, Norwegian University of Science and Technology, Trondheim, November 2005, Norway.
- [17] A. E. Engin, W. Mathis, W. John, G. Sommer, H. Reichl, "Closed-form network representation of frequency-dependent RLCG parameters", International Journal of Circuit Theory and Applications, vol.3, pp. 463-485, John Wiley & Sons, Ltd., 2005.
- [18] A. Darcherif, A. Raizer, G. Meunier, J. F. Imhoff, and J. C. Sabonnadiere, "New techniques in FEM Field calculation applied to power cable characteristic computation", IEEE Transaction on Magnetics, vol. 26, no. 5, pp. 2388-2390, September 1990.
- [19] P. Mäki-Ontto, H. Kinnunen, J. Luomi "AC motor cable model suitable for bearing current and over-voltage analysis", International Conference on Electrical Machines ICEM'04, CD-ROM, no. 365, 6 pages, Cracow, Poland, 2004.
- [20] S. Kim, D.P. Neikirk, "Compact Equivalent Circuit Model for the Skin Effect", IEEE-MMT-S International Microwave Symposium Digest, vol.3, pp.1815-1818, San Francisco, USA, 17-21 June 1996.
- [21] H. De Paula, D. A. de Andrade, M. L. R. Chaves, J. L. Domingos, M. A. A. de Freitas, "Methodology for Cable Modeling and Simulation for High-Frequency Phenomena Studies in PWM Motor Drives", IEEE Transaction on Power Electronics, vol. 23, no. 2, pp. 774-752, March 2008.
- [22] G. Skibinski, R. Tallam, R. Reese, B. Bucholz, R. Lukaszewski, „Common mode and differential mode analysis of three phase cables for PWM AC drives“, Proceedings of IEEE 41st, Industry Applications Society Annual Meeting, pp.880-888, 8-12 October 2007, Tampa, USA.
- [23] A. Boglietti, A. Cavagnino, "Induction Motor Model for Low and High Frequency Analysisysis", ICEM'06, CD-ROM, 6 pages, Creta , Greece, 2-5 September 2006.
- [24] K. Kuepfmueller, *Einfuehrung in die theoretische Elektrotechnik*, 10. Auflage, Springer Verlag, Heidelberg 1973.

6. Subproject 2: Comparative analysis of losses in inverter-fed machines caused by high frequency current components using time-stepping

Prof. Dr.-Ing. habil. Dr.h.c. Andreas Binder

Dipl.-Ing. Mehran Mirzaei

Institut für Elektrische Energiewandlung, TU Darmstadt

E-Mail: mmirzaei@ew.tu-darmstadt.de

6.1. Introduction

Permanent magnet (PM) synchronous machines with concentrated windings are used nowadays for a large variety of applications in the smaller power range up to several kW [1], [2]. If concentrated windings are used also in the MW range (e.g. for wind power generation) or for higher rated speed, the eddy current losses in rotor conductive parts and iron cores - due to the increased number of inducing stator field space harmonics and sub-harmonics, caused by the concentrated winding distribution and the slot openings even at sinusoidal supply -, may become a

problem for overheating the conductive rotor magnets [3]. Especially, the NdFeB magnets are very sensitive to an increased temperature, losing their remanence irreversible. The thermal calculations and modeling are therefore very important in design processes of these types of machines. Hence, the losses in thermal computations are inputs or sources that should be studied in detail. In cage induction machines, concentrated windings are not used, as the increased number of space harmonics will induce the rotor cage strongly, causing high losses and parasitic forces. But even with distributed windings the remaining space harmonics at sinusoidal supply and the additional fields at inverter supply are inducing the rotor cage, causing increased losses. The field is compressed in the air gap and tooth tip region due to the shielding effect of the cage, causing additional iron losses in the tooth tips and mainly stator tooth shafts due to flux penetration.

The calculation of losses in different parts of PM synchronous with concentrated windings and in a special cage machines with a distributed winding for hybrid and electrical vehicles is evaluated in this report using analytical and numerical methods. The PM machines have been designed and implemented at the Institute for Electrical Energy Conversion. They are highly utilized electrical machines with intensive cooling. These machines are 45 kW, 400V, 1000 / min, 16 poles [1], but were also operated with field-weakening at constant voltage 400 V, at an elevated speed 3000 / min to provoke considerable eddy currents. The 15 kW cage induction motor was manufactured at ATB and was measured at the Universität der Bundeswehr München.

In the first part of report, additional losses in the windings due to the current displacement are evaluated by numerical and analytical calculations using 2D MAXWELL and by one modified one-dimensional analytical method. In the second part of the report, the eddy current losses analysis in magnets is presented using analytical calculation. The axial segmentation effect on the eddy current losses in the magnets is taken into account. In this method, the induced eddy current effect on the source field is neglected because of large penetration depth in comparison with the magnet thickness at the slot and switching frequencies.

The fundamental frequencies are 133.33 Hz and 400 Hz at 1000 /min and 3000 /min and switching frequency is always 4 kHz. The 3D finite element analysis ANSYS 3D is used to verify the proposed analytical method. In the third part of the report, core losses and magnet losses are calculated using FLUX 2D. In this simulation, the *Bertotti* model is used for the loss calculation in the iron core. The software uses the time-stepping finite element method with the rotor moving capability, which is very important to take into account the harmonic losses in the rotor, especially in the magnets. This has been done by Mr. Petrovic for no load and loading with sinusoidal source. In this report, the load calculations with inverter and short circuit simulations are presented. The calculations are compared with experimental results to evaluate the accuracy of the analysis and assumption.

6.2. Additional losses in windings

Two different stators I and EW2 for synchronous PM machines with 16 poles are analyzed at 1000 / min (rated speed) and 3000 / min (flux-weakening) with a sinusoidal current source. A simple and a detailed one-dimensional analytical method are presented to take into account induced eddy current effect on the windings losses. A numerical analysis using *Maxwell* 2D and *Flux* 2D finite element analysis softwares is done. Two models are simulated in the finite element calculations. First a simple model is simulated, which is just a one slot model in the *Maxwell* environment. The whole machine is calculated in *Flux* software at 3000 / min with and without consideration of saturation and rotor effects. The number of conductors per coil in each slot is 96 and 60 for stator EW2 and I, respectively. The width of the slot in stator I is 9 mm and the average width in stator EW2 is 18.76 mm. Fig. 1 shows 3D views of the motors EW2-D and I-D, where the stators I and EW2 are combined with rotor D with surface mounted rotor magnet shields.

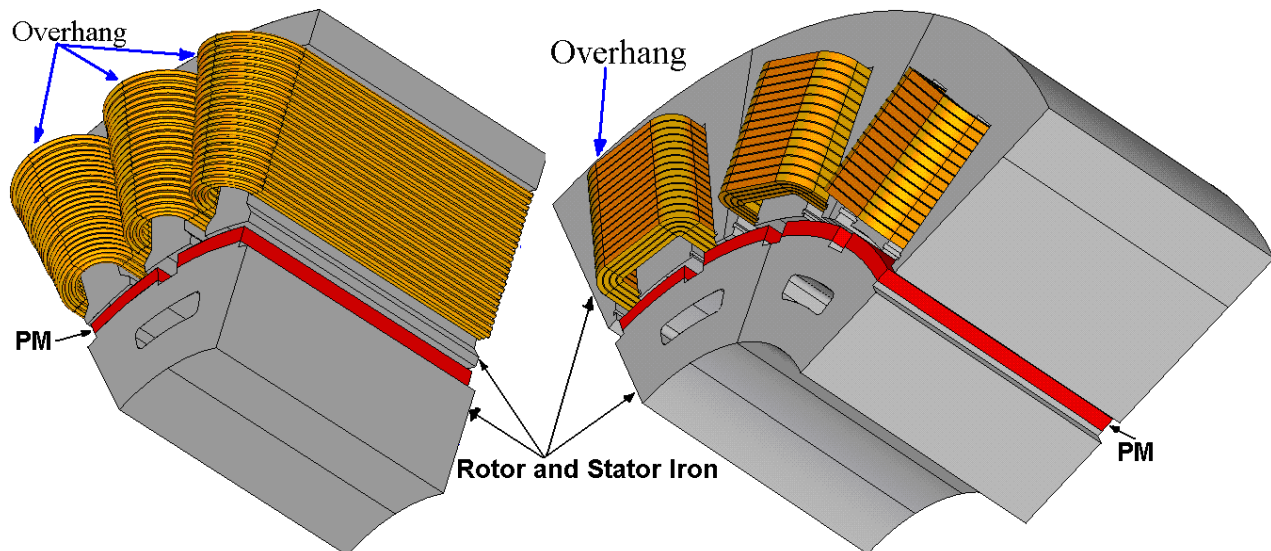


Fig. 1. 3D models of a permanent magnet machine with Stators I and EW2 and rotor D

The eddy current losses in the winding overhang are negligible, because the magnetic flux closes its path in the air and the flux density has a small value relative to the magnetic flux density inside the slot. Due to the series connection of all wires inside the slots, second order effect is the main factor in producing additional copper losses in windings. The end winding I^2R losses are considered for the whole copper losses as an additional value. The increase of winding losses at increased frequency leads to the AC losses coefficient, which is calculated using (1):

$$k_R = \frac{P_{AC}}{P_{DC}} \quad (1)$$

First, the losses in the winding of stator I are computed. According to Fig. 1 and with consideration of the number of poles 16, the factor k_R at 20°C for stator I at 1000 /min ($f=133.33$ Hz) and 3000 / min ($f = 400$ Hz) is 1.3 and 4.01 using classical formula [3], respectively. The analytical calculation is modified for EW2 with round wire random wound coils to calculate the copper losses in the windings. The wire shape is changed from a circular cross section to the rectangular shape (Fig. 2). The square side size (h_{Cu}) is calculated from circular wires diameter (d_{Cu}) as follows:

$$h_{Cu} = \frac{\sqrt{\pi}}{2} d_{Cu} \quad (2)$$

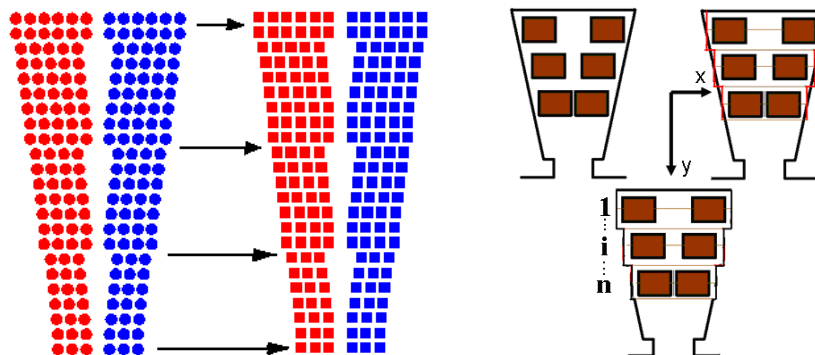


Fig. 2. Reshape of circular wire cross section to the rectangular conductor cross section and proposed model for a modified one-dimensional method

For stator EW2, the factor k_R is 1.1 and 1.6 using the modified analytical method. The factor k_R is considerably less in the EW2 than stator I because the equivalent width of the slot is bigger in EW2 and the two-layer winding from two different phases in one slot causes a smaller magnetic flux density and finally smaller additional eddy current losses in windings inside the slots. Fig. 3 shows the calculated current distribution in one simplified slot model for stator I and EW2 using *Maxwell FEM*. The amplitude of current per conductor is 1 A. The factor k_R for stator I is 1.33 and 4.01, respectively.

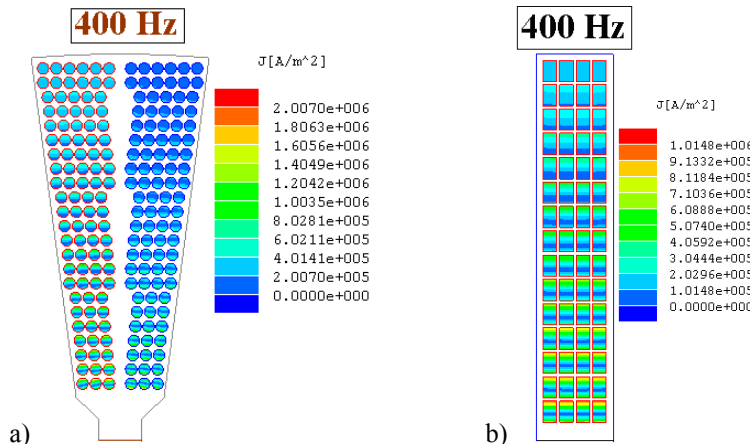


Fig. 3. The current density plot in stators a) EW2 and b) I, at 3000 /min

Hence the analytical results coincide well with FEM results. Finally the machines EW2-D and I-D are simulated with *Flux 2D* software, taking into account the current displacement and the rotor field and iron saturation (Fig. 4 and 5). It is shown that the simplified analytical and numerical methods of Fig. 2, 3 are sufficient to calculate the additional eddy current losses in windings up to 3000 /min. The saturation and rotor field do not affect the results.

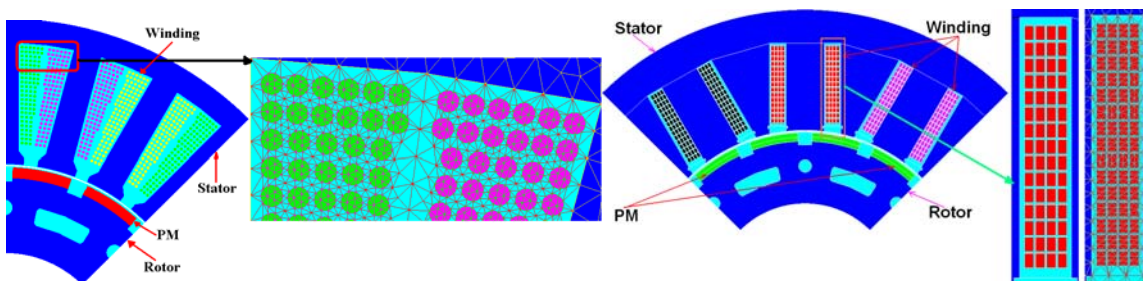


Fig. 4. Models of stators EW2 and I with rotor D, showing the mesh density in the conductors

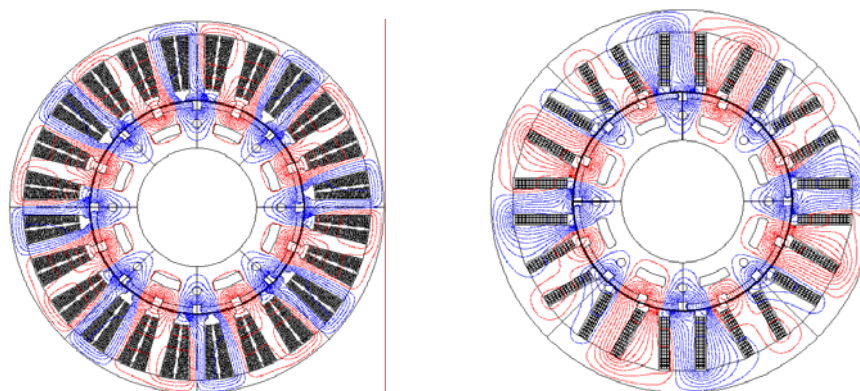


Fig. 5. Calculated magnetic flux distribution in the PM synchronous machines EW2-D and I-D at 3000 / min at full load

6.3. Eddy current losses in the magnets

The calculation of the circumferential magnet segmentation effect to reduce the eddy currents can be done with two-dimensional methods. For the consideration of the axial magnet segmentation a three-dimensional model is needed [4], [5]. Often the axial segmentation effect is considered by a correcting end factor to decrease the magnet electrical conductivity like in solid rotors and linear induction machines [8], but this method is less precise. On axial segmentation effect computations, several papers are published with 3D transient FEM methods, e.g. [4], [5], with analytical methods, e.g. [10], [11] or combined 2D analytical with 3D static FEM methods like [6]. The 3D FEM methods are rather time consuming procedures, whereas the analytical methods like [9], [10], which consider also the reaction field of the eddy currents, consider only the axial segmentation, but no segmentation in circumference direction.

For a rather simple simultaneous consideration of the axial and circumference segmentation the reaction field of the eddy currents must be neglected. Then a simplified 3D analytical calculation of the eddy currents is possible [8]. For typical PM synchronous machines applications with concentrated windings the dominant stator field harmonics induce the rotor magnets with frequencies low enough, that the characteristic penetration depth d_E of the eddy currents in the magnets is usually bigger than the magnet height h_M . This is due to the low electrical conductivity of rare earth magnets (NdFeB: typically 0.625 MS/m). Hence the reaction field of the induced eddy current is negligible in comparison to the penetrating stator field. The method [8] is applied to two different types of PM synchronous machine with concentrated windings and surface-mounted, non-skewed NdFeB rotor magnets (rotors A and D). The influence of the segmentation on the steady state rotor temperature at no-load operation was checked experimentally. The method [7] was checked with a time-consuming 3D FEM time-harmonic analysis.

Stator EW2 has a concentrated double layer winding with round-wire coils, semi-closed slots and $q = 0.5$ slots per pole per phase. Stator I has a concentrated single layer winding with prefabricated profile wire tooth coils, open stator slots of alternating different width, and $q = 0.25$. Hence in the stator field *Fourier* spectrum not only higher harmonics with ordinal numbers $|v| > 1$, but also a sub-harmonic $v = -1/2$ with double wave length of the fundamental $v = 1$ occurs, causing additional eddy current losses.

Two rotors with surface mounted magnets were built (Fig. 6). Rotor D has one magnet per pole in circumference direction and 4 segments in axial direction. Rotor A has 7 segments per pole in circumferential direction and six segments in axial direction. The stator bore diameter is $d_{si} = 180$ mm, the stator stack length is $l_{Fe} = 180$ mm, the magnet height is $h_M = 4.7$ mm, the magnet width $b_M = 27.2$ mm (Rotor D), 3.9 mm (Rotor A), the magnet length $l_M = 45$ m (Rotor D), 30 mm (Rotor A), the pole pitch is $\tau_p = 35.3$ mm and the magnetic air gap width is $\delta = 1.4$ mm.

The number of turns per coil and the rated current are for Stator EW2 : $N_c = 12$, $I_{s,N} = 94.5$ A, for Stator I: $N_c = 15$, $I_{s,N} = 128$ A [2]. The current layer distribution for two pole pairs is shown in Fig. 7 for the two stators at rated current for $I_U = \sqrt{2} \cdot I_{s,N}$, $I_V = I_W = -I_U/2$. The ordinal numbers of the current loading *Fourier* wave spectrum for stator EW2 are $v = 1, -2, 4, -5, 7, \dots = 1 + 3g$, $g = 0, \pm 1, \pm 2, \dots$, where the fundamental $v = 1$ produces the torque with the rotor fundamental field wave.

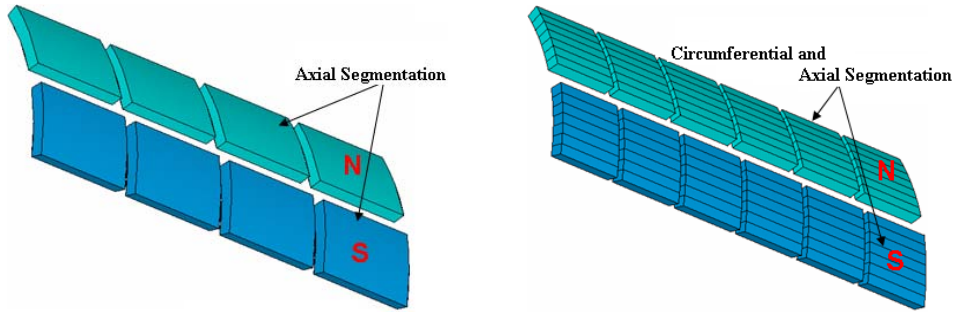
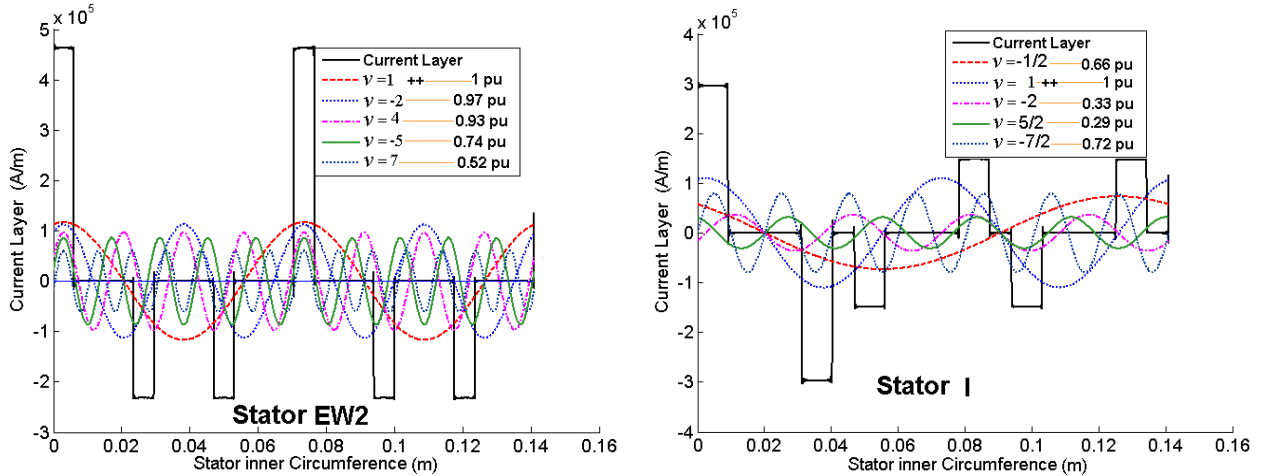


Fig. 6. 3D models of the segmented magnets of one pole pair: Left: Rotor D, Right: Rotor A

Fig. 7. Current layer distribution and their *Fourier* wave spectrum for the two Stators EW2 and I along two pole pairs at rated current for $I_V = I_W = -I_U/2$.

With Stator I the ordinal numbers are $\nu = -1/2, 1, -2, -5/2, 7/2, \dots = -(1+3g)/2, g = 0, \pm 1, \pm 2, \dots$. While $\nu = 1$ produces the torque, the sub-harmonic $\nu = -1/2$ causes additional eddy current losses in the magnets. The stator field harmonics, excited by a sinusoidal stator current with the frequency f_s , induce the rotor with frequencies $f_{rv} = (1-\nu) \cdot f_s$. In comparison to the concentrated winding a symmetrical distributed three-phase winding would have more than 50% less harmonics with ordinal numbers $\nu = 1, -5, 7, -11, 13, \dots = 1+6g$ and much smaller amplitudes, as the higher number of slots demands much smaller slot openings. Hence much lower losses occur. But the distributed winding is more expensive, has a longer winding overhang and for a high pole count in small machines even the simplest distributed winding $q = 1$ slots per pole and phase is difficult to manufacture. In the *Cartesian* coordinate systems according to [8] the magnets are treated as thin plates in the y -direction, lying in the x - z -plane. Hence the eddy current density vector consists of an x - and z -component: $\vec{J}(x, z, t) = (J_x, 0, J_z)$. The closed eddy current loops demand $\text{div} \vec{J} = \nabla \cdot \vec{J} = 0$. So \vec{J} can be calculated as $\vec{J} = \text{rot} \vec{I} = \nabla \times \vec{I}$ due to the identity $\nabla \cdot (\nabla \times \vec{I}) = 0$. The vector potential $\vec{I}(x, z, t)$ has only a y -component: $\vec{I} = (0, I_y, 0)$. We chose for the vector potential \vec{I} the additional condition $\nabla \cdot \vec{I} = 0$ to define it completely. From *Faraday's* law we derive the differential equation for the unknown $I_y(x, z, t)$. The boundary conditions must give vanishing eddy currents at the magnet boundaries (Fig. 8): $I_y(x=0) = I_y(x=b_M) = 0, I_y(z=-l_M/2) = I_y(z=l_M/2) = 0$.

The reaction field of the eddy current is neglected. Like in [9], [10] the inducing normal component of the air gap field B_y is developed as a *Fourier* series in z -direction with assumed

alternating field direction for axially adjacent magnets (Fig. 8). This assumption leads to ordinal numbers $\lambda = 1, 3, 5, 7, \dots$ and allows within the boundaries $-l_M/2 \leq z \leq l_M/2$ a correct mathematical description of the complete amplitude $B_y(x, z)$ at a frequency f .

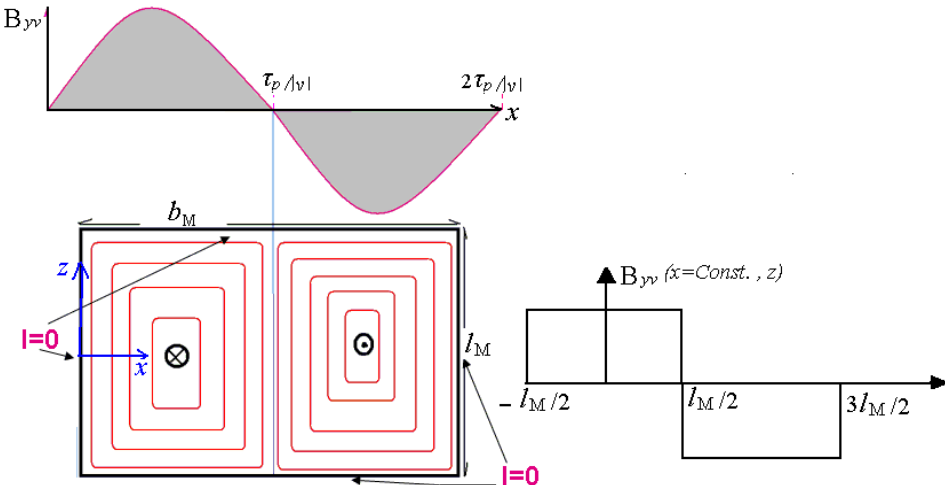


Fig.8. Penetrating v -th air gap field wave B_y , induced 2D eddy current density distribution in the surface mounted magnets, treated as thin plates, and periodical expansion of the air gap field in axial direction

From $\vec{J} = \text{rot} \vec{I} = \nabla \times \vec{I}$ we derive the current density components $J_x = -\partial I_y / \partial z$, $J_z = \partial I_y / \partial x$ as a *Fourier* sum with harmonic amplitudes $J_{xv\lambda}$ and $J_{zv\lambda}$. The eddy current losses for z magnets per machine are calculated. In the following dominant field waves with the ordinal numbers $v = -2$ (Stator EW2) and $v = -1/2$ (Stator I) are discussed. Figs. 9 and 10 show the current distribution, which one calculated by the proposed analytical method.

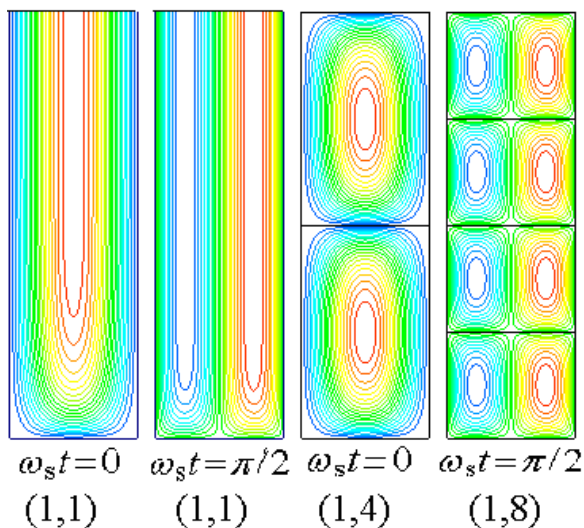


Fig.9. Stator EW2, 45 kW, 1000/min: Analytically calculated eddy current field lines per pole, induced by the second field harmonic $v = -2$ in a surface mounted PM rotor with one magnet segment per pole in circumference and three different axial magnet segmentations; (from left to right): One segment per pole at two different time instants, four and eight axial segments. One axial half depicted!

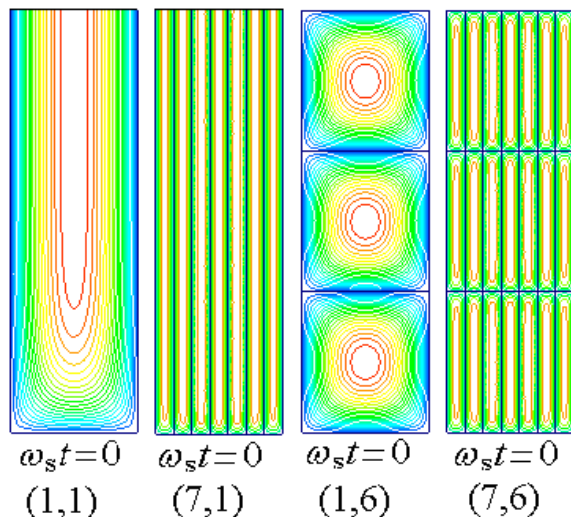


Fig.10. Stator I, 45 kW, 1000/min: Analytically calculated eddy current field lines per pole, induced by the sub-harmonic $v = -1/2$ in a surface mounted PM rotor and one vs. seven magnet segments per pole in circumference, (from left to right): no axial segmentation, 6 axial segment rows. One axial half depicted!

With the 3D FEM *Ansys* package the analytical solutions for the eddy current distribution and the eddy current losses are checked for the field waves $\nu = -2$ (Stator EW2) and $\nu = -1/2$ (Stator I) with the time harmonic method. As infinite iron permeability is assumed, only the air gap and the magnets must be modeled. One wave length of the considered field harmonic is modeled. For $\nu = -2$ this is one pole pitch, for $\nu = -1/2$ this comprises four pole pitches. The bore curvature and the eddy current reaction field are taken into account. The field waves are excited by current layers, located on the stator bore. The theoretically perfect sinusoidal current layer distribution of each considered harmonic was replaced by a 9-phase and alternatively by a three-phase system excitation, each with $q = 1$, which gave similar results. In Fig. 11 the iso-areas of constant axial eddy current density values are compared with Stator EW2, $\nu = -2$, for one magnet per pole with infinite and finite length. There is only a small difference of 2 % in losses between both cases. In Fig. 12 the axial segmentation effect with 4 segments as configuration (1,4) is compared to (1,1) for the inducing effect of the sub-harmonic of Stator I. The calculated axial eddy current density component, depicted per one axial half of a magnet segment, is reduced slightly from 3.2 A/mm^2 to 2.8 A/mm^2 . Fig. 13 shows, that for one magnet per pole in circumference and an axial segmentation a reduction by 50% of the losses of the dominant field waves needs 6 to 8 axial segments with axial segment lengths of 30 ... 22 mm. The analytical and the 3D FEM method yield similar results. The circumference segmentation (Fig. 14) is far more effective: With two instead of one segment the losses are reduced by 50% to 80%, leading to a magnet a) width of 17 mm. Obviously up to 1000/min 4 circumference segments per poles are sufficient, although 7 will bring a further reduction of 50% in losses.

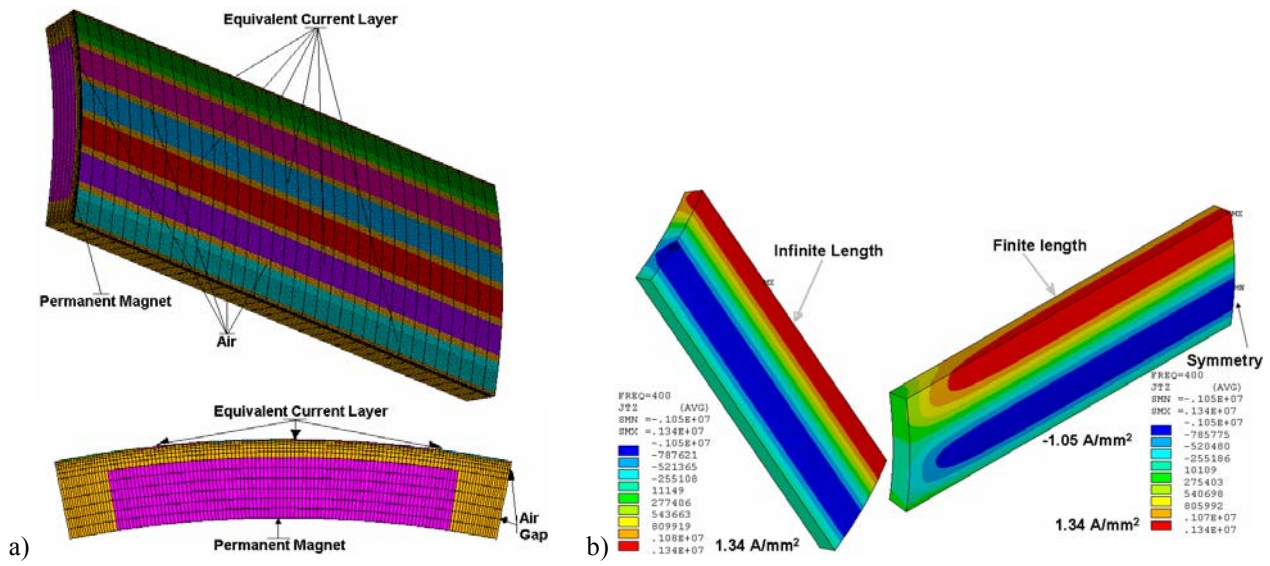


Fig. 11. One pole pitch of Stator EW2: a) above: 3D mesh for; below: 2D side view of the meshing with magnet, air gap and current layer region. A three phase equivalent current layer was used to excite the second field harmonic and numerically calculated axial component of the eddy current density for one pole pitch, induced by the second field harmonic, b) one magnet per pole: Infinite left) vs. finite right) magnet length, depicting only one axial half of the magnet segment

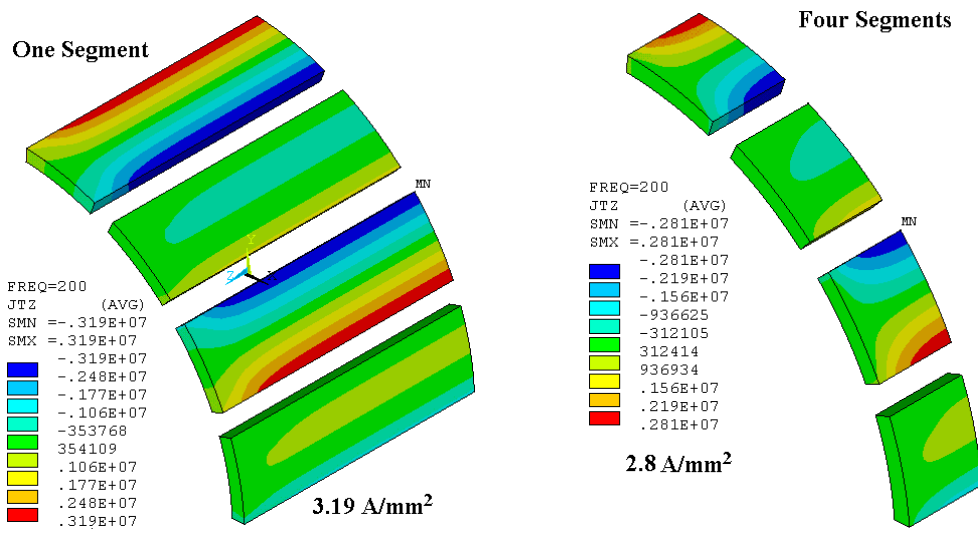


Fig. 12. Stator I, 45 kW, 1000/min: Numerically calculated axial component of the eddy current density for four pole pitches, induced by the sub-harmonic field $v = -\frac{1}{2}$, one magnet per pole in circumference: Left: No axial segmentation, Right: 4 axial segments, depending only one axial half of a segment

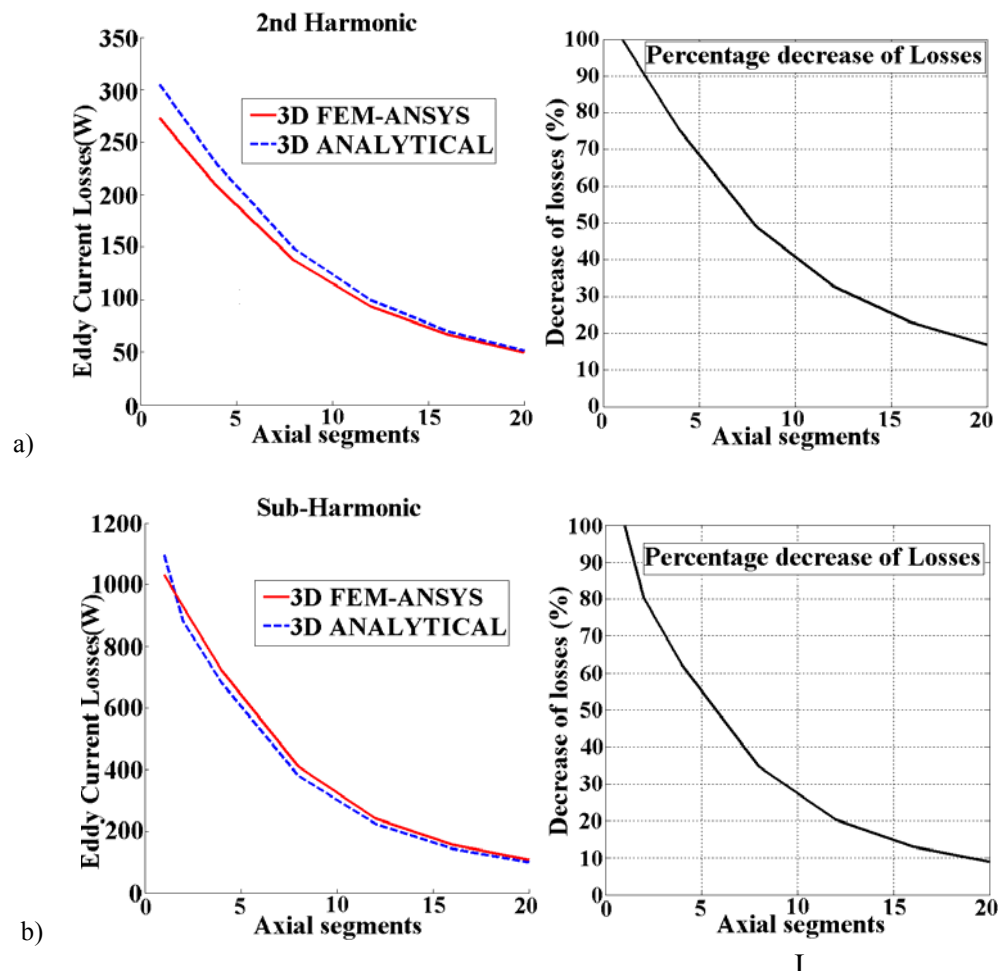


Fig. 13. Axial segmentation, 45 kW, 1000/min: Numerically and analytically calculated eddy current loss reduction with axial segmentation a) stator EW2, $v = 2$ and b) stator I, $v = -\frac{1}{2}$

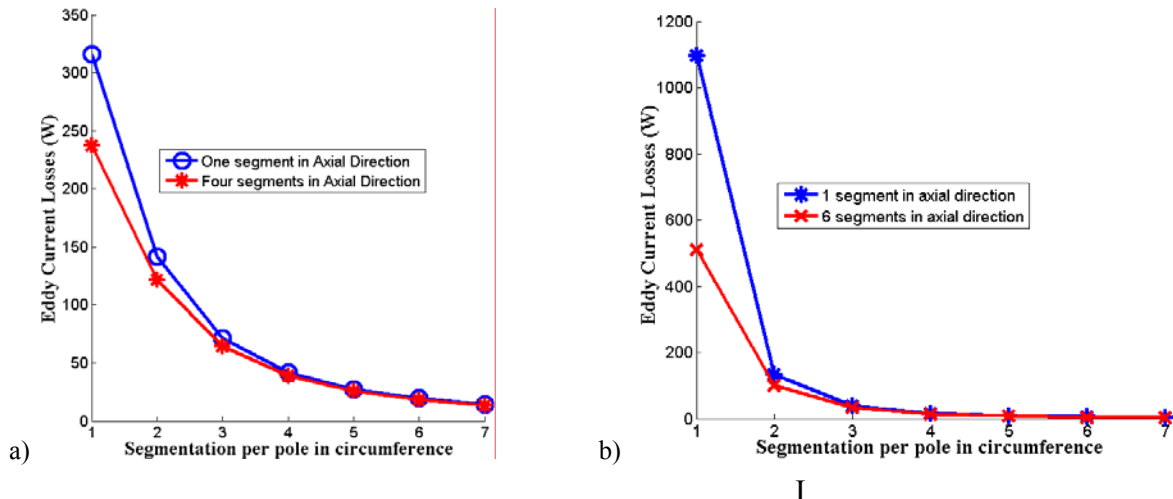


Fig. 14. Segmentation in circumference, 45 kW, 1000/min: Numerically and analytically calculated eddy current losses of the dominant field harmonic a) stator EW2, $v = 2$ and b) stator I , $v = -1/2$

With stators EW2&I and rotors D&A four motor configurations were tested experimentally at full load 45 kW, 1000/min with inverter-feeding. The switching frequency 4 kHz and the big stator inductance of the concentrated windings gave a nearly sinusoidal stator current. The magnet eddy current losses cannot be measured directly. They were estimated from the local temperature rise $d\vartheta/dt$ from cold start, where one can assume adiabatic heating. Then the eddy current losses P are obtained via the magnet mass m and their heat capacity c according to $P = m \cdot c \cdot d\vartheta/dt$, directly related to $d\vartheta/dt$. The local temperature was measured with a Pt100 probe and slip rings. The measured losses (Table I) are for the segmented Rotor A (7 segment per pole in circumference, 6 segments per pole in axial direction) in good concordance with the calculations, whereas for Rotor D (1 magnet per pole in circumference, 4 magnets in axial direction) the calculated losses are by a factor 10 bigger. With the ANSYS FEM 3D similar big losses for the Motors EW2-A and I-A are derived. The measured loss balance at the generator short circuit test showed a similar big loss increase, so the somewhat uncertain determination of the initial temperature tangent $d\vartheta/dt$ may be an explanation for the difference.

Table I- Comparison between calculated and measured results

Motor	EW2-D	EW2-A	I-D	I-A
Current	94.5 A	94.5 A	128 A	128 A
Measured losses from $d\vartheta/dt$	27 W	9 W	70 W	18 W
Measured losses from short circuit test	317 W	0	814 W	0
Analytically calculated losses	237 W	13 W	682 W	21 W
Calculated losses ANSYS 3D	208 W	-	723 W	-

As a conclusion, we state that based on published methods for analytical eddy current calculation in thin plates, the eddy current losses in surface-mounted permanent magnets may be calculated, neglecting the self-field of the eddy currents, the iron reluctance and the bore curvature. The results are in good concordance solutions from with 3D FEM time-harmonic with consideration of the eddy current self field. The proposed analytical model can be applied to the PM synchronous machines design to evaluate the losses in the magnets especially with concentrated windings, at high speed applications or in machines of big size, because it is fast and accurate.

6.4. Calculation of losses in different parts of machines including iron losses

The loss calculation in PM synchronous machines using *Flux-2D* has been done at inverter-fed loading at 1000 / min and 3000 / min. Also the short circuit for calculations are presented at 1000 / min and 3000 / min. The Russel end effect factor was used to take into account the third dimension effect on eddy current losses in the magnets [14]. The copper losses have been determined by a formula with consideration of the skin effects. The iron losses in *Flux-2D* are calculated by the Bertotti model for iron losses [13]. This means that the rotating and pulsation losses are taken into account as classical and excess eddy current losses and classical pulsating hysteresis losses in the iron laminations. Fig. 15 shows the comparison between FEM results and experimental values at loading. Almost in all cases except with rotor D, the FEM calculations coincide well with experimental ones for different PM synchronous machines, which consist of the combinations of the two stators EW2 and I with the 3 rotors A, C, D, where C has buried magnets with 7 segments per pole in circumference and 6 segments in axial direction. In the generator short circuit cases, the calculation results show good accuracy in comparison with the measurement.

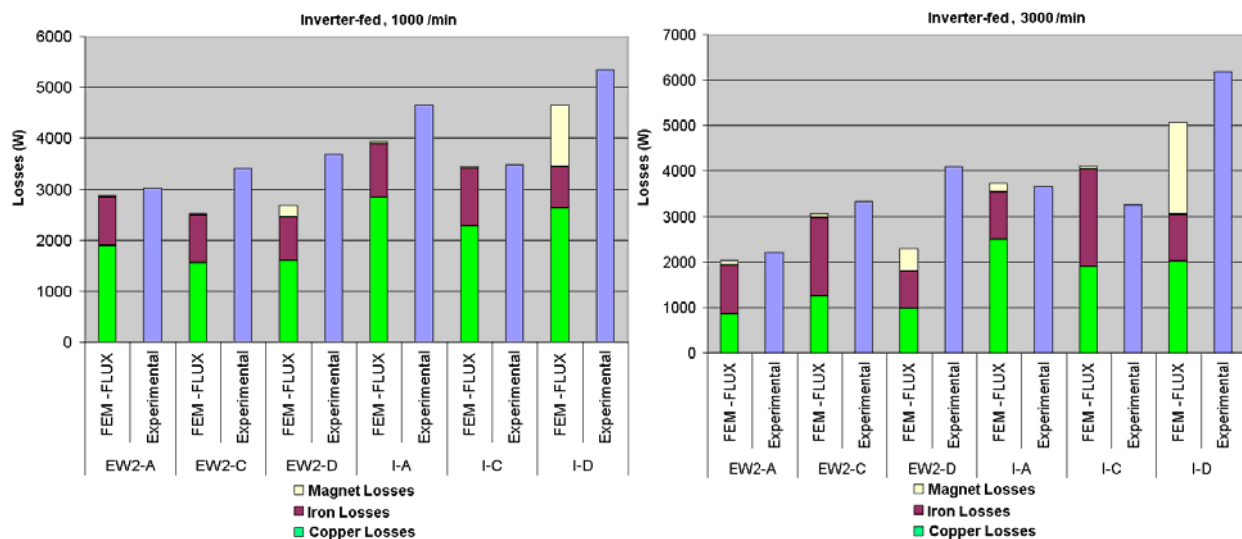


Fig. 15. Losses in PM synchronous machines with inverter operation

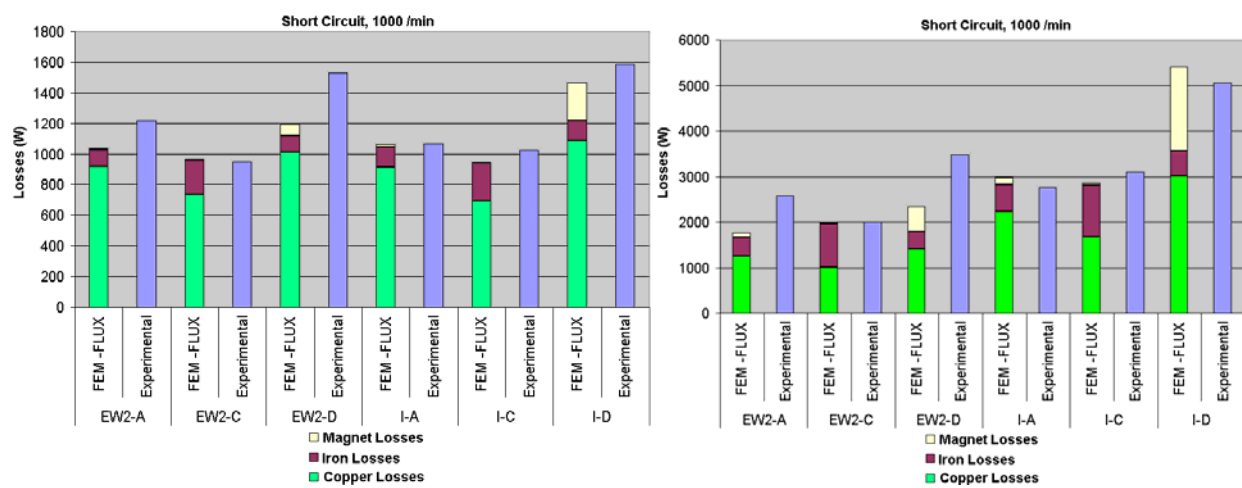


Fig. 16. Losses in PM synchronous machines at generator short circuit conditions

6.5. High Speed Induction Motor

In this part, a high speed induction motor for hybrid vehicle is analyzed using *Flux-2D*. The losses including classical copper and iron losses, rotor cage losses and additional losses due to the space and time harmonics are very important in high power density and high speed induction machines [15]-[17]. High losses, especially in the rotor mean high temperature especially at the bearings and make the motor unusable in the proposed application of an electric vehicle drive at high speed of 12500 / min. The structure of the machine is shown in Fig. 17. The induction machine is a high power density motor that needs an intensive jacket cooling by water. The nominal power of the induction motor is 15 kW, but it can work under overload at 35 kW. The maximum speed of the machine is 12500 /min. The induction motor has 4 poles, 3 phases with 48 stator slots and 40 rotor slots without any skewing.

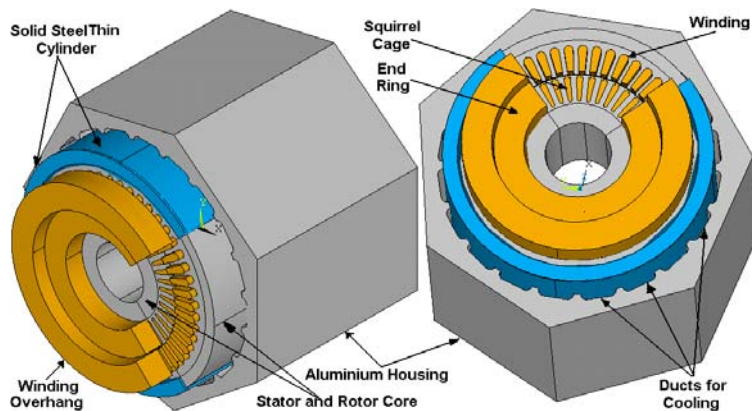


Fig. 17. 3D model of the simulated high speed induction motor

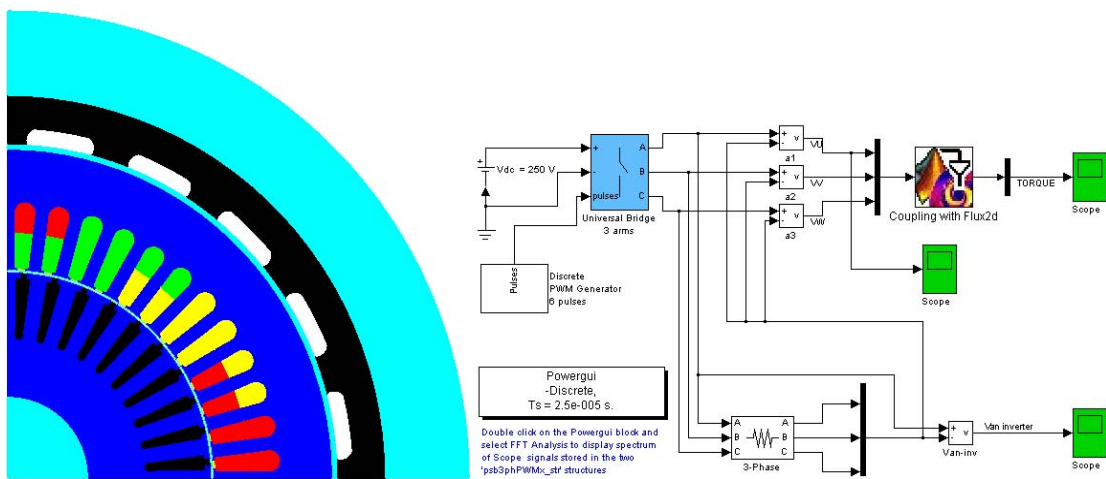


Fig. 18. 2D FLUX model and coupling with Matlab/Simulink for the inverter-fed modelling

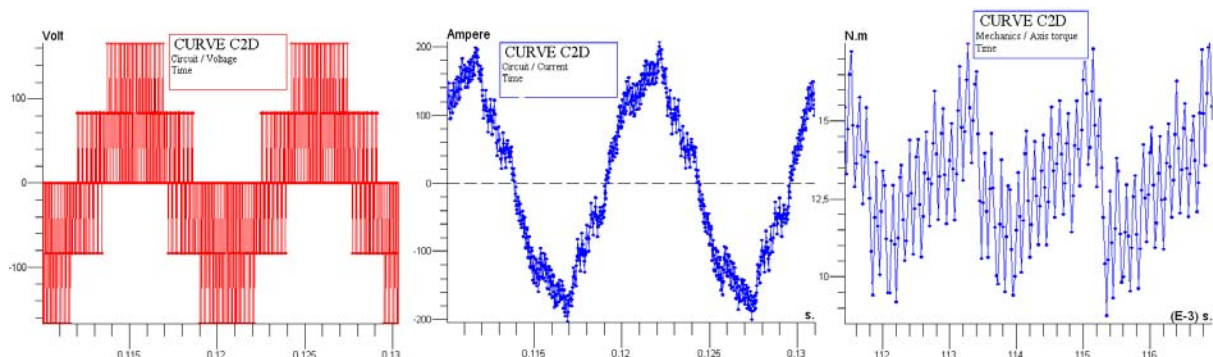


Fig. 19. Input voltage, current and output torque at nominal speed 2760 /min, switching frequency 4 kHz

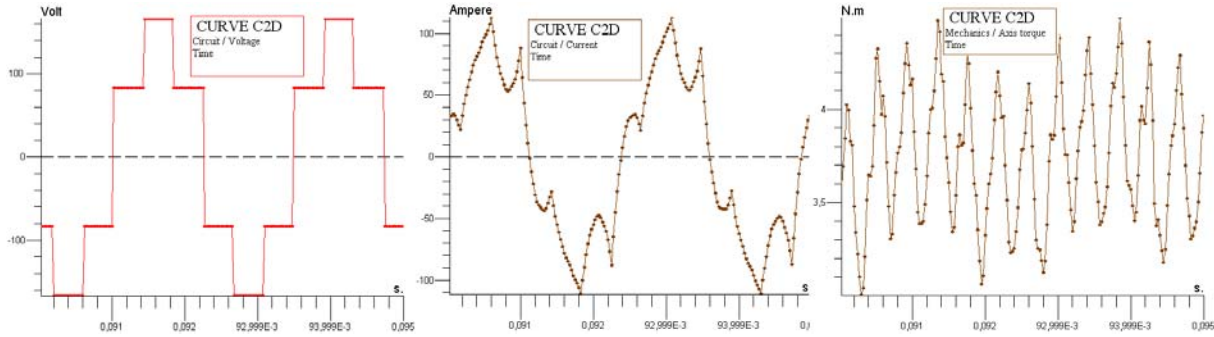


Fig. 20. Calculated input voltage, current and output torque at high speed 12000 /min, switching frequency 4 kHz

The machine model in *Flux-2D* is shown in Fig. 18. For the modelling of the inverter, the coupling between *Matlab/Simulink* and *Flux-2D* has been used (Fig. 18). The voltage and current shapes at nominal and high speed are shown in Figs. 19 and 20. The output voltage of the inverter in Fig. 20 is a square wave because it works with maximum output voltage. The loss diagrams for nominal speed and high speed (11000, 12000 and 12500 /min) are shown in Figs. 21-22 for the considered induction motor. The FEM results show higher values for the total losses than the experimental ones. But in most cases, the results coincide well. A thin cylinder of a solid iron can is shown in Fig. 17, which is placed between the stator core and the aluminium housing. At high torque and at overload points especially at low speed due the saturation in stator core, the magnetic flux penetrates into the solid iron cylinder and produces considerable eddy current losses in this region. At nominal speed 2762 /min and rated load, the losses in the solid iron cylinder are approximately 100 W.

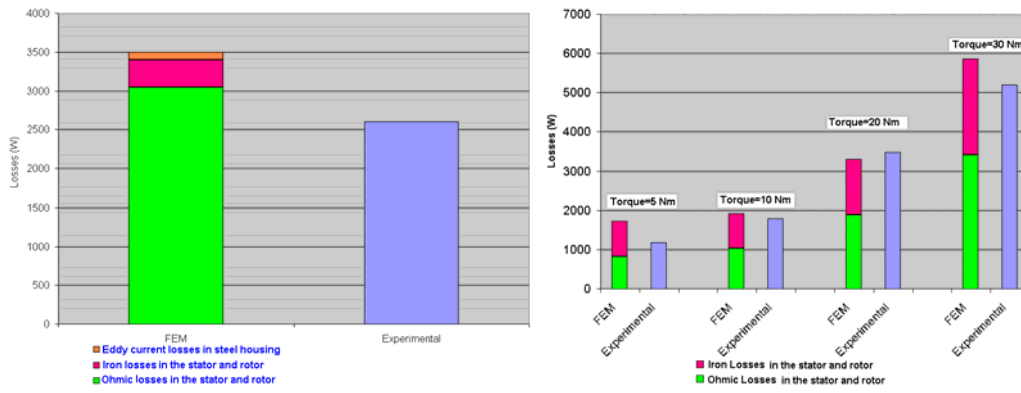


Fig. 21. Losses diagram for nominal speed (2762 /min) and rated output power (15 kW) and at 11000 /min speed with different torques

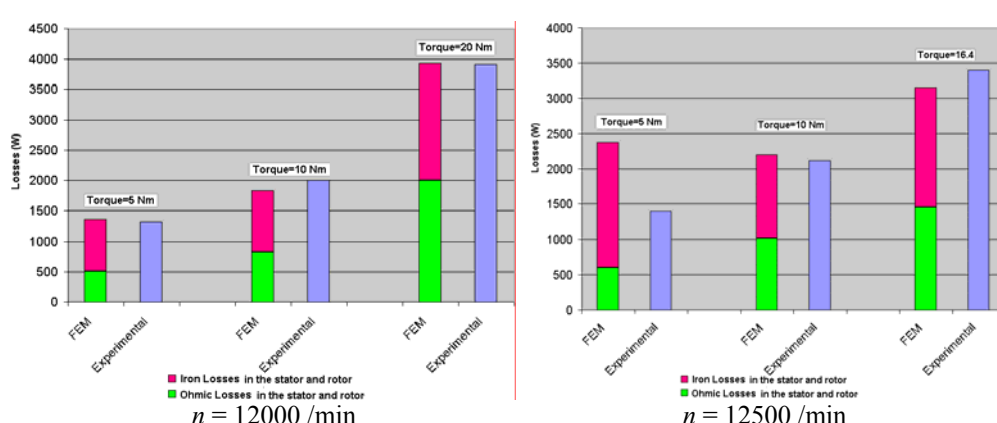


Fig. 22. Losses diagram for 12000 /min and at 12500 /min speed with different torques

6.6. Conclusions

The additional losses due to slotting and winding space harmonics at sinusoidal supply and due to current time harmonics due to inverters supply were investigated by numerical field analysis and by experiment. The investigation showed for high power density PM synchronous motors with concentrated windings already at sinus supply considerable additional losses especially at high speed, which made a magnet segmentation necessary. The additional losses due to inverter supply were rather low due to the low current ripple, which was smoothed by the big stator inductance of the concentrated winding.

In the cage induction machine the concentrated winding cannot be used due to otherwise extremely high additional losses. With distributed winding and a high slot count per pole the additional losses at sinusoidal supply are low. The additional losses at inverter supply are independent of the load. A solid stator iron can should be avoided, because at high saturation high eddy current losses may occur then.

The additional losses were analysed with 2D FLUX software in comparison to analytical calculation. As there is no skewing, no additional losses due to inter-bar currents in the aluminium die-cast cage and rotor can occur. The high number of 12 slots per pole in the stator gives a very sinusoidal field distribution, which is only disturbed by the slot harmonics. But their amplitudes are small due to the semi-closed slots. So the additional losses at sinusoidal supply are dominated by the eddy current losses in the thin solid iron stator cylinder, which was used to seal the stator from the water jacket. These additional losses in the can increase already at no-load and high stator flux when the stator iron yoke is saturated and the field penetrates the core with stator fundamental frequency. Apart from that effect the additional losses at sinus supply are typically below 1% of the output power. The measured increase of the losses at inverter operation depend mainly on the switching frequency, are more or less independent of load and speed range typically below 300 W.

References

- [1] C. Deak, A. Binder, K. Magyari: "Magnet Loss Analysis of Permanent-Magnet Synchronous Motors with Concentrated Windings", ICEM 2006, Chania, Greece, September 2006, 6 pages, CD-ROM
- [2] C. Deak and A. Binder, "Highly utilised permanent magnet synchronous machines with tooth-wound coils for industrial applications," in Proc. Electromotion'05, Lausanne, Switzerland, September 2005, CD-ROM, 6 pages
- [3] F. Laube, H. Mosebach and W. Canders, "Skin Effect in Large Polyphase Machines with Concentrated Windings", ICEM Conference 2008, Vilamoura, Portugal, 6 pages, CD-ROM
- [4] Y. Aoyama, K. Miyata and K. Ohashi, "Simulation and Experiments on Eddy Current in NdFeB Magnet", IEEE Trans. on Magnetics, Vol. 41, no.10, 2005, p.3790-3792
- [5] Y. Kawase, T. Ota and H. Fukunaga, "3-D Eddy Current Analysis in Permanent Magnet of Interior Permanent Magnet Motors", IEEE Trans. on Magnetics, Vol. 36, no.4, 2000, p.1863-1866
- [6] J. D. Ede, K. Atallah, G. W. Jewell, J. B. Wang, and D. Howe, "Effect of Axial Segmentation of Permanent Magnets on Rotor Loss in Modular Permanent-Magnet Brushless Machines," IEEE Transactions on Industry Application, Vol. 43, No. 5, pp. 1207-1213, September 2007.
- [7] K. Yamazaki and, S. Watari, "Loss Analysis of Permanent-Magnet Motor Considering Carrier Harmonics of PWM Inverter Using Combination of 2-D and 3-D Finite-Element Method," IEEE Transactions on Magnetics, Vol. 41, No. 5, pp. 1980-1983, May 2005.
- [8] S. Sikora, J. Purczynski, W. Lipinski, and M. Gramz, "Use of Variational Methods to The Eddy Currents Calculation in Thin Conducting Plates," IEEE Transactions on Magnetics, Vol. 14, No. 5, pp. 383-385, September 1978
- [9] C. Deak, L. Petrovic, A. Binder, M. Mirzaei, D. Irimie and B. Funieru, "Calculation of eddy current losses in permanent magnets of synchronous machines", Proc. of the Symp. on Power Electronics, Electrical Drives, Automation & Motion (SPEEDAM), 11.-13.6.2008, Ischia, Italy, paper no. MEM201, p. 26-31, CD-ROM
- [10] K. Oberretl, "Dreidimensionale Berechnung des Linearmotors mit Berücksichtigung der Endeffekte und der Wicklungsverteilung", Archiv f. Elektrotechn. (Electr. Engin.) 55, 1973, p. 181-190
- [11] U. Beckert, "Berechnung zweidimensionaler Wirbelstroeme in kurzen Permanentmagneten von Synchronmaschinen", antriebstechnik 6, 2007, p.44-48
- [12] H. Lee, C. Y. Chin, "A theoretical analysis of linear induction motors", IEEE Trans. On Power Apparatus and Systems, 1979, Vol. PAS-98, no.2, p. 679-688

- [13] G. Bertotti, "General properties of power losses in soft ferromagnetic materials", IEEE Trans. Mag., Vol. MAG-24 No. 1, 1988, pages 621-630
- [14] L. Petrovic, A. Binder, C. Deak, D. Irimie, K. Reichert, C. Purcarea: "Numerical methods for calculation of eddy current losses in permanent magnets of synchronous machines", ISEF 2007, Prague, Czech Republic, September 2007, CD-ROM, 6 pages
- [15] G. Joksimovic, A. Binder, "Additional no-load losses in inverter-fed high-speed cage induction motors", Electrical Engineering (Archiv für Elektrotechnik), Vol. 84, 2004, pp.105-116
- [16] M. Aoulkadi, A. Binder, G. Joksimovic, "Additional losses in high-speed induction machines- removed rotor test", EPE 2005, Dresden, 10 pages
- [17] H. B. Ertan, K. Leblebicioglu, B. Avenoglu, M. Pirgaip, "High-Frequency Loss Calculation in a Smooth Rotor Induction Motor Using FEM", IEEE Transactions on Energy Conversion, Vol. 22, No. 3, September 2007, pp. 566-575.

7. Subproject 3: Simulation of wave propagation phenomena in inverter-fed drives

Dr. Olaf Henze

Institut für Theorie Elektromagnetischer Felder, TU Darmstadt

E-Mail: henze@temf.tu-darmstadt.de

Prof. Dr.-Ir. Herbert De Gersem
Catholic University of Leuven, Belgium,

7.1. Network-Model

The first step of the project was to develop a rather simple network model, which describes the complete system "inverter-cable-motor". This model is the basis of deeper research of the different parts of the drive. The goal is to determine the steady-state HF behavior of the cable and the motor. This results in a model which allows the calculation of the voltage at the motor side in the frequency domain. The voltage at the motor terminals, caused by a general periodic signal like an inverter signal, can be calculated by using Fast Fourier Transformation.

a) Cable

The cable is modelled by the approach presented in [1]. It is important that in our case a three-phase cable is needed to connect the inverter to the motor. Hence a General Transmission- Line Model of the cable is needed, which considers the coupling of the inductors and the capacitors between the three phases of the cable. A decoupling of the 3 phases can be achieved by finding the Eigenvectors and –values of the coupling matrix. It results in three different modes: the common-mode (0-mode), and two differential modes (1-mode, 2-mode). It is significant that the propagation constant and the wave impedance of the common mode are different from the constants of the differential modes.

The decoupling of the three phases in the three modes makes it possible to apply the common transmission line theory to the three modes. It results in three transfer functions, which connect the three input voltages to the three phase voltages at the induction motor.

b) Induction-Motor

The model of the induction motor is based on the (abc)-approach [2]. In the stationary case the system of six differential equations can be reduced to a linear algebraic system, which connects the stator voltages to the stator currents. The obtained matrix is an impedance matrix. Also in this case, a transformation in the (012)-system results in a decoupling of the currents and the voltages. The new impedances can be identified as the impedances, which arise in the three transfer functions, which describe the behavior of the three-phase cable. In this simplified motor model, only the ohmic and inductive coupling behavior is described. The HF stray capacitances are

missing. Hence only the Differential Mode is described rather properly, whereas the CM winding capacities is missing.

c) Inverter

To create the inverter signal a triangle pulse is compared with a sinusoidal signal. This procedure is the most simple basis of the Pulse-Wide-Modulation (PWM). If the sinusoidal pulse is bigger than the triangular pulse, the line-to-line output voltage of the inverter is set to the DC link voltage $+U$; in the other case the voltage is $-U$. The resulting signal is a sequence of rectangular pulses with different pulse lengths [3]. After interaction with the cable-motor system operating as a low-pass filter, the pulse train more or less decays to the sinusoidal signal. To calculate the voltages at the motor side it is necessary to transform the inverter signal into the frequency-domain. This can be performed by Fast-Fourier-Transformation. After transformation into the (012)-system, multiplication with the transfer-functions and back transformation into the (abc)-system, the voltages at the induction motor can be obtained. The network model has been compared with measurements from Mr. Rocks (TP4). The simulation results are compared to measurements for a case where the direct current link voltage of the inverter is 780 V and the cable length is 130 m. The experimental and simulation results are shown in [10]. The voltage reflection at the motor terminals is predicted quite well, but it is not possible to predict a HF CM ground current in the motor.

7.2. Stator coil model of an induction motor

From 7.1, it is obvious that the network model gives only a rough description of the behavior of the whole drive. In the network-model of the induction motor capacitive effects, which should arise in the high frequency domain, are missing completely. Hence in a next step a more accurate modeling of the stator coils is necessary to get insight into the behavior of high frequency effects. For modelling the stator coils in an induction motor, the wires of one slot of the coils are considered as a Transmission Line in axial z-direction. By considering of one slot of the stator coils and using the basic equations of the Transmission-Line Theory, it is possible to calculate the voltage and current values at each position within the coil. The capacitances of the model are determined by electrostatic field solutions and the outer inductances can be derived by the capacitances by assuming TEM-waves. For the calculation of the resistance, the skin effect occurring at high frequencies is considered. The conductivity of the insulating material is neglected. It is obvious that in this equation all wires are still independent of each other. To interconnect the wires to coils, further conditions are necessary. To get the additional coil conditions, it is necessary to consider that in one coil certain current and potentials of the end of one forward wire in one slot are equal to the potentials and currents of the beginning of a certain backward wire in another slot. The principle of this method is explained in [4]. The three phases of the winding are connected in star.

The impedance of one phase of a coil system of a given 110 kW 4 pole motor, which was measured at TU Darmstadt, is calculated. While the first phase is set on a positive potential $+U$ and the second phase is set on a negative potential $-U$, the third phase is grounded. The input impedance is calculated for different frequencies. The results are compared with experimental values (Figure 1). They are obtained from the described motor without a rotor (removed rotor test) and with a star connected stator winding. The measurement is carried out by a voltage excitation between two phases while the third phase is grounded. The magnitude and the phase of the impedance are measured in dependence on the frequency by an LRC-meter [11].

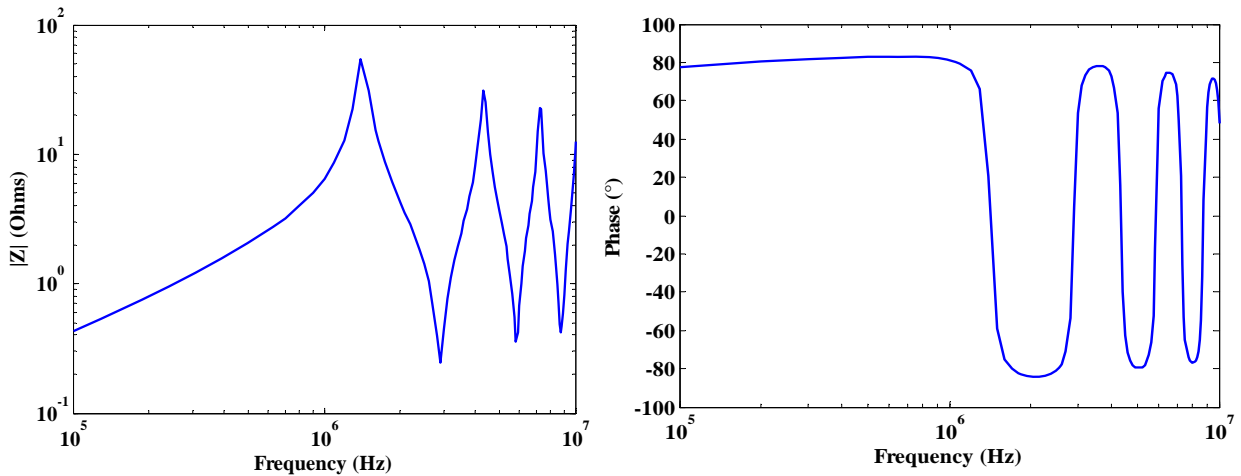


Fig.1a. Impedance and phase shift of stator-coil system (Simulation) of a 110 kW – 4 pole, 3 phase cage induction motor

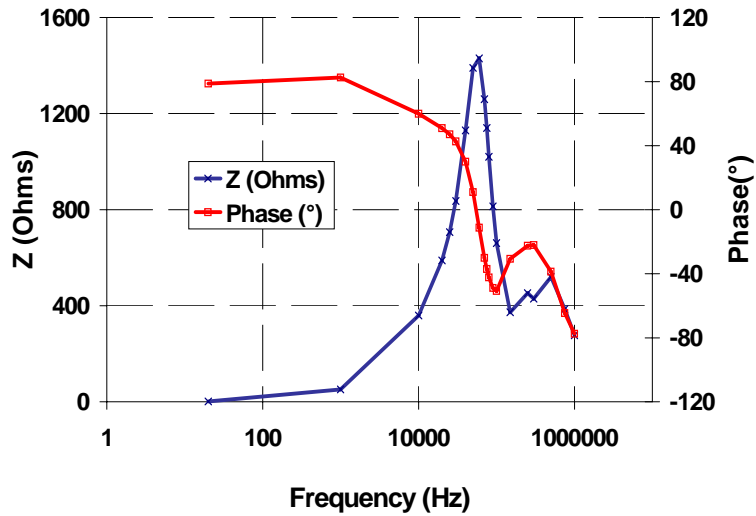


Fig.1b. Impedance and phase shift of the stator-coil system (Experiment)

In the measurement and in the simulation inductive effects are dominating at low frequencies and capacitive effects are dominating at high frequencies. But while the measurement shows only one sharp resonance, many resonances occur at higher frequencies in the simulation. The resonance frequencies and the resistance at the resonance are different. One reason of these discrepancies is that the used slot geometry in our model is an approximation. Further on the determination of the resistance in the model is in general dependent on the boundary conditions. First analytical calculations show that for higher resistances resonant frequencies become smaller. Therefore a better approximation of the resistance is necessary, which could be a numerical calculation of the different resistances by FEM at different frequencies, which is a cumbersome process. Furthermore the influence of the overhang is not considered yet in the model. While the inductive coupling between different phases is neglected inside the slot, this effect is not negligible in the overhang any more. Another reason of the difference is that the confinement of the fields in the slot due to shielding eddy current in the iron stack is also just an approximation. Because of the laminated yoke of the motor there are only small eddy currents at low frequency, which increase with frequency. The next steps are therefore 3D-field simulations, which are considering this case.

7. 3. Dimensional slot-yoke model

a) Introduction

To examine the influence of the iron core on the common-mode effects, it is necessary to model the stator with a part of the iron core in three dimensions. In two dimensions this is done in [5], [6]. A 3D high frequency simulation of a complete motor is too complicated, in particular due to the presence of small relevant geometrical details like the iron sheet thickness of 0.5 mm. Instead, a model consisting of one stator slot, the slot insulation and a fraction of the surrounding iron core is considered. High frequency effects mainly arise due to the capacitive coupling between coil and iron core. In case of a sinusoidal excitation, the calculation of voltage and current distributions can be done in a steady-state case, where the relation between the current and voltages are obtained in the frequency domain. Another possibility is to carry out transient simulations via time stepping, where the voltage and current distribution of an input voltage surge with a short rise time can be analysed.

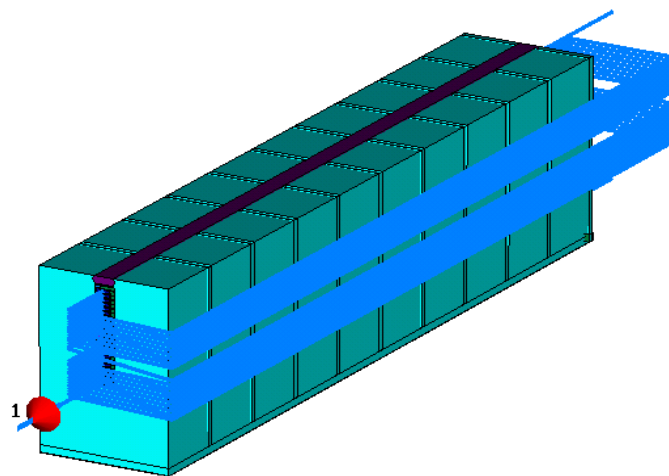


Fig. 2. 3D model of one slot with parts of the iron core

b) Motor Model

In a realistic motor iron core the thickness of the iron sheets is with 0.5 mm very thin in the direction of wave propagation. This would lead to very small grid steps. To reduce the grid steps and to equalize the grid the iron sheet thickness is enlarged in axial direction of current propagation in the slot. The iron core is, therefore, modelled by 10 sheets which consist of a conductive part and an insulating part (Fig. 2). The characteristic properties of the materials are adapted, respectively: The iron conductivity is decreased such that the field damping in the material remains unchanged with the increased thickness of one sheet.

The excitation voltage is the line-to-iron core voltage at 1 MHz. To get the sinusoidal amplitude of the voltage at this frequency, a theoretical voltage signal (Fig. 3) is decomposed in a *Fourier* series. With a given switching frequency of 5 kHz, one can find a voltage of approximately 0.5 % of the fundamental component amplitude.

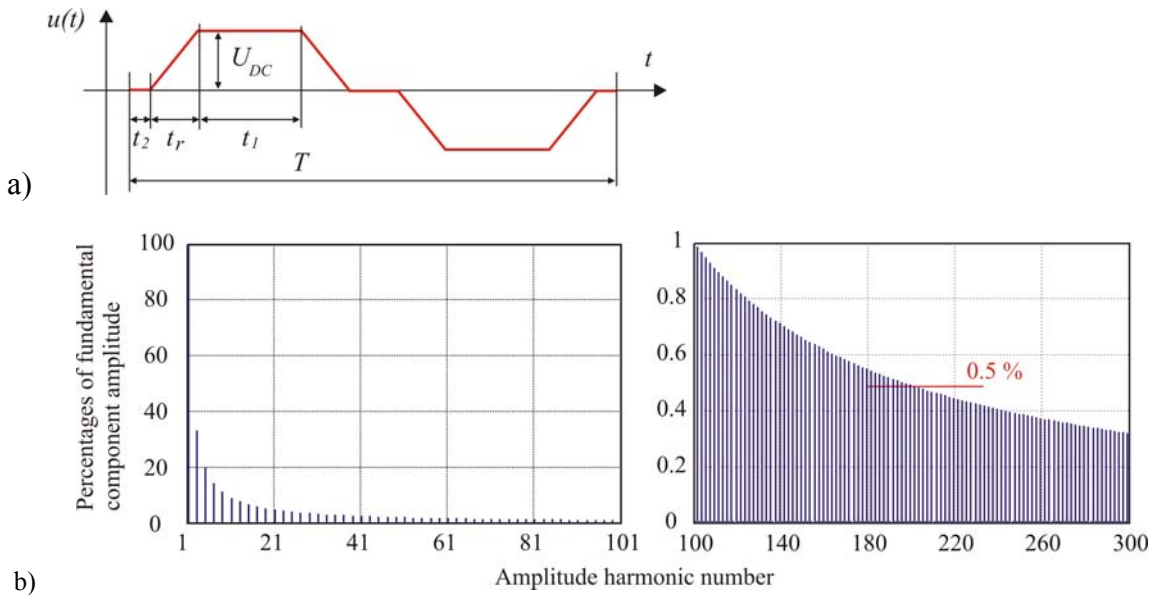


Fig.3. a) Theoretical voltage signal for the harmonic determination of the line-to-iron core voltage, and
b) Frequency spectrum for $T = 0.2$ ms, $t_r = 50$ ns, $t_2 = 0$

c) Steady State Calculations

The input impedance and the earth current of Fig. 2 are calculated for different frequencies. At each frequency the mesh has to be adapted due to the skin effect in the conductive materials. Figure 4 shows the magnitude of the input impedance over the selected frequency range.

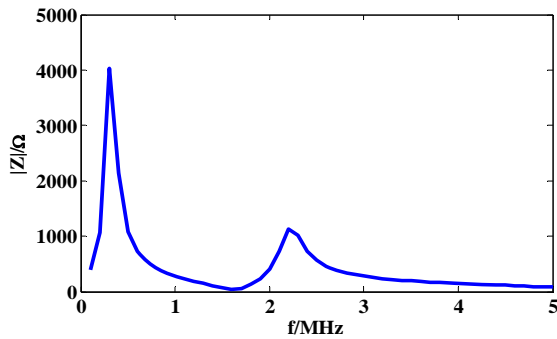


Fig.4. Magnitude of the calculated input impedance of the coil of Fig. 2

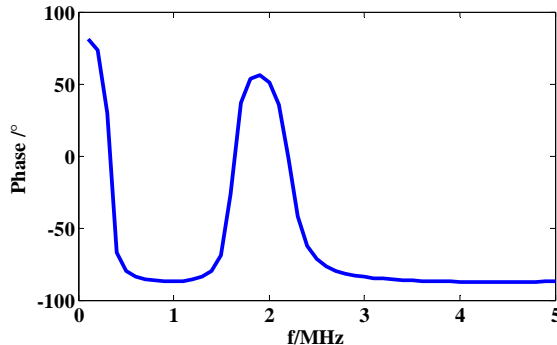


Fig.5. Phase of the calculated input impedance of the simulated coil of Fig. 2

The iron core is directly connected to the boundary, which represents the ground. The impedance increases at frequencies between 0 and 300 kHz, indicating the dominance of inductive effects. Then one distinctive resonance is observed, whereas the maximum impedance is 4000 ohms. Between 300 kHz and 1.6 MHz the impedance decreases, which indicates that the winding

inductance gets compensated by the capacitance between winding and iron core. Capacitive effects are dominating in the next fraction of the selected frequency range. Starting from 1.6 MHz the impedance increases again. A second resonance is found at 2.2 MHz at an impedance of 1100Ω . Also in the phase diagram (Fig. 5) an oscillation between inductive regions and capacitive regions is obvious.

Figure 6 shows the calculated current between iron core and ground. While at low frequencies it is zero, the current increases for higher frequencies. There is one resonance at 1.6 MHz. Then the current decreases until it reaches nearly zero again. After reaching a minimum at 2.8 MHz the current increases linearly. Notice that the resonance of the earth current is occurring at the minimum of the input impedance (compare Fig.6 to Fig.4).

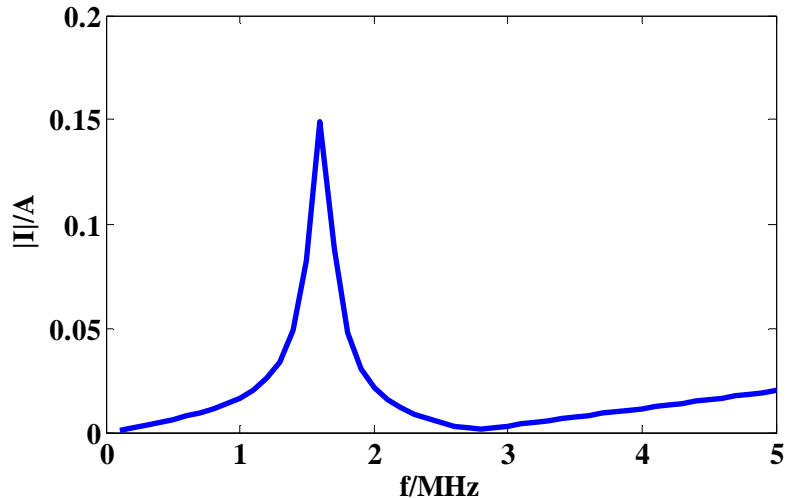


Fig.6. Magnitude of calculated earth current in the selected frequency range of Fig. 2

d) Current and Voltage Distributions

To examine the behavior of the current and voltage inside the turns of the winding at different turns, ports are built in to determine the voltage and current amplitude and phase at a frequency of 1.6 MHz, which corresponds to the minimum of the input impedance and the maximum earth current.

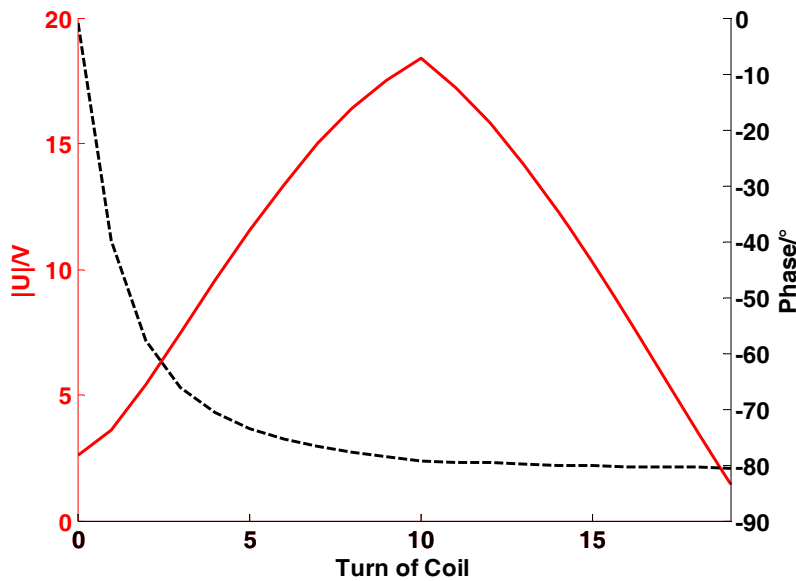


Fig.7. Voltage amplitude and phase distribution at a frequency of 1.6 MHz

If the coil is excited by a sinusoidal pulse with a certain frequency, the results are standing wave distributions of voltage and current. The results can be seen in Figure 7 and 8. The voltage increases up to nearly 18 volts, which is more than 6 times higher than the excitation voltage. After that the voltage decreases to zero. The phase decreases steadily from 0° to -80°.

Also the current distribution forms a standing wave. After the current amplitude reaches its minimum, the phase jumps by 180°, which means that after that the resulting current amplitude becomes negative. The difference between the input and the output current is 0.07A-(-0.08A) = 0.15A, which is equivalent to the simulated earth current at a frequency of 1.6 MHz (Fig.6).

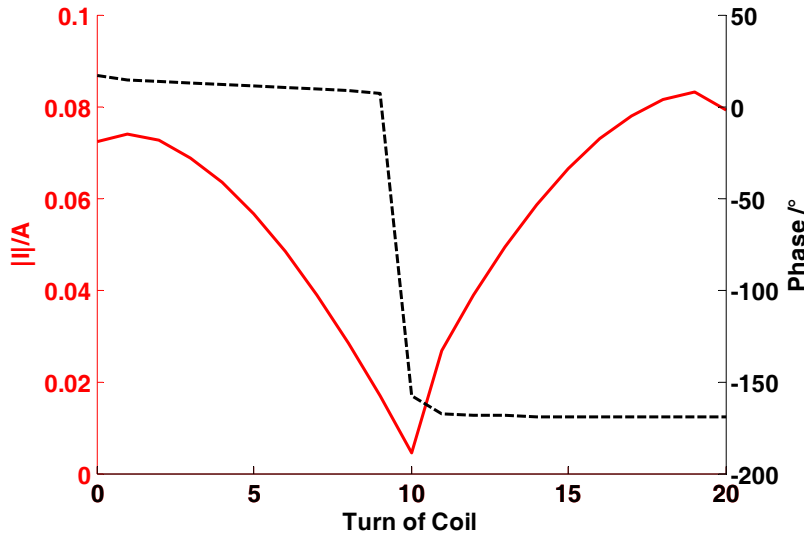


Fig. 8. Current amplitude (bold) and phase distribution (dashed) at a frequency of 1.6 MHz.

e) Transient Calculations

Different examinations of surge phenomena can be found in the literature [7, 8]. To examine the behaviour of the voltage inside the coil (Fig. 2) when a surge impinges the coil terminals, transient calculations are carried out. The skin effect can be considered by using surface-impedance-boundary-conditions.

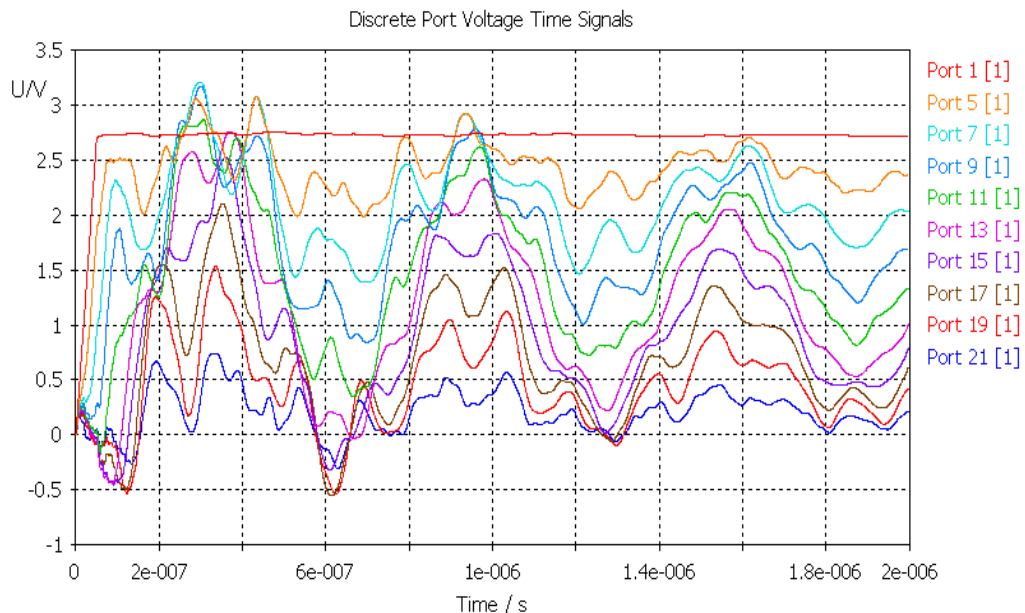


Fig. 9. Calculated time dependence of the voltage in different turns of the coil of Fig. 2

The excitation signal is defined as a rectangular surge with a voltage of 2.7 volts and a rise time of 50 ns. The complete simulated time frame is 2 μ s. The resulting voltage distributions with respect to the coil turn and to time are shown in Figure 9. While on the input terminal (Port 1) the rectangular signal is visible, the voltages at the different turns (Port 5, 7 ..., 21) are oscillating, whereas damping is observed. The voltage distribution is calculated a) at 50 ns, which is directly after the rising time of the surge and b) at the end of simulation time (2 μ s) (Figure 10). The dotted curve is the voltage distribution after 50 ns. It is obvious that the whole voltage drop occurs over the first 8 turns of the windings. After 2 μ s the voltage is distributed nearly linearly in the whole coil.

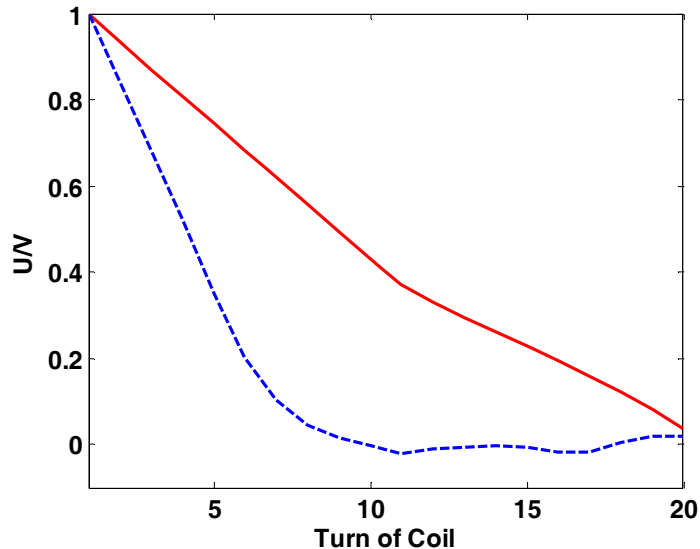


Fig.10. Calculated initial (dotted line) and final (solid line) voltage distribution in different turns of the coil of Fig. 2

The results can be compared with the theoretical approach [9,12]. Both results show good agreement. The time behaviour of the coil current is shown in Figure 11.

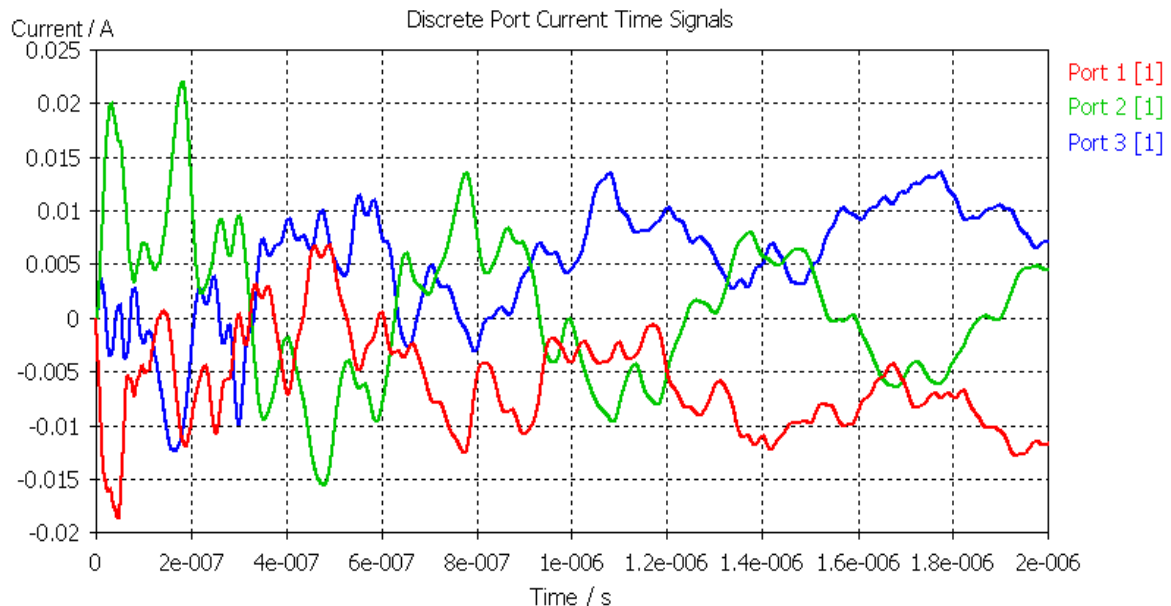


Fig.11. Calculated time dependence of the coil current at the input (port 1), the output (port 3) and between frame and boundary (port 2) of the coil of Fig. 2

Because at small time instances capacitance effects are dominating, the behaviour of the current at the input can be compared there by a simple RC network model, pulsed by a voltage jump with an increasing time of 50 ns. The results are shown in Figure 12.

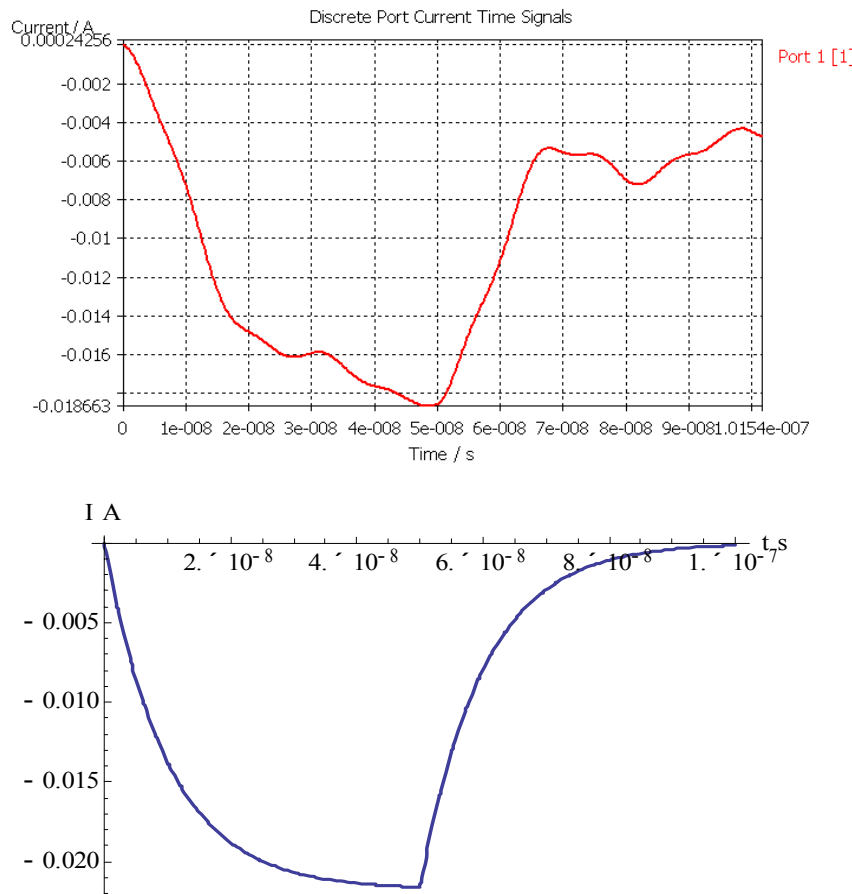


Fig.12. Time dependence of the input current: above: simulation of one-slot model, bottom: RC-network model

Both figures show good agreement. The current is increasing between 0 and 50 ns. With constant voltage the current is decreasing between 50 and 100 ns. In the network-model the capacitance and resistance are estimated to 400 pF and 25 Ω.

7.4. Conclusions

The numerical models for HF effects in inverter-fed electrical machines have to big demands: A large frequency scale between fundamental frequency and HF voltage and current oscillation; and a large space scale between 0.5 mm for iron sheet thickness and the big motor and cable dimensions in the m-range. Hence it was not possible to develop a model with sufficient refinement for HF effects on a system scale of inverter cable and motor. Therefore, different refinement levels were investigated with different mathematical models: the transmission line model for the motor-cable system and the stator winding and the FE model for the coil-iron coil system. Even then, the iron core had to be modelled in a simplified wavy by thicker sheets of reduced number and decreased conductivity.

References

- [1] Bolsens, De Brabandere et al., "Transmission Line Effects on Motor Feed Cables: Terminator Design and Analysis in the Laplace Domain", International Electric Machines and Drives Conference (IEMDC), CD-Rom, Madison, Wisconsin, USA, June 1-4, 2003
- [2] Pillay, Lewis, "Mathematical Models for Induction Machines", IEEE, IAS Annual Meeting October 1995, pp.606-616
- [3] P. Mutschler, "Grundlagen der Energietechnik", Vorlesungsskript SS1996
- [4] Luff, Norris, "High Frequency Theory of Power Transformers", School of Engineering and Applied Science, Aston University, Birmingham
- [5] Mäki-Ontto, Luomi, "Common-Mode Flux Calculation of AC-Machines", Proc. ICEM02, Bruges, Belgium, 25-28 August 2002, CD-Rom
- [6] Mäki-Ontto, Luomi, "Circumferential flux as a source of bearing current of converter-fed AC machines", Proc. Of 2002 Nordic Workshop on Power and Industrial Electronics, NORPIE/2002 Stockholm Sweden, CD-Rom
- [7] Guardado, Carrillo et al., "Calculation of Interturn Voltages in Machine Windings During Switching Transients Measured on Terminals", IEEE Transactions on Energy Conversion, Vol.10, No. 1, March 1995, pp.87-94
- [8] McLaren, Abdel-Rahman, "Modeling of Large AC Motor Coils for Steep-Fronted Surge Studies", IEEE Transactions on Industry Applications, Vol.24, No. 3, pp.422-426, May/June 1988
- [9] Heller, Veverka, "Surge Phenomena in Electrical Machines", ILIFE Books LTD Prag 1968

8. Subproject 4: Ageing mechanisms and energy handling capability of metal-oxide varistors for over-voltage protection in inverter-fed drives

Prof. Dr.-Ing. Volker Hinrichsen

Dipl.-Ing. Alexander Rocks

Fachgebiet Hochspannungstechnik, Institut für Elektrische Energiesysteme, TU Darmstadt

E-Mail: rocks@hst.tu-darmstadt.de

8.1. Einleitung

Beim Betrieb von Drehstromantrieben an Frequenzumrichtern entstehen in Folge von Wanderwelleneffekten auf der langen Zuleitung aufgrund der sehr steilen Schaltflanken des pulsweitenmodulierten Spannungsmusters des Umrichters Überspannungen an der Maschine, welche die Lebensdauer der Wicklungsisolation der Maschine erheblich minimieren können. Derartige Effekte müssen bei der Dimensionierung der Maschine berücksichtigt werden, wobei den Überspannungen auf verschiedene Art und Weise entgegengewirkt werden kann: neben der in der Regel nicht praktikablen Möglichkeit, mit einer kurzen Zuleitung die Amplitude der Überspannung klein zu halten, bietet sich hier besonders der Einsatz von Filtern an, mit denen ebenfalls Einfluss auf die Höhe der Überspannung genommen werden kann.

Im Rahmen des von der Fa. Hübner GmbH und der Stiftung Johannes Hübner geförderten Projekts, das fachlich und organisatorisch jedoch in die DFG-Forschergruppe FOR 575 eingebunden ist, wird ein neues Verfahren zur Reduktion der Überspannungen an der Maschine untersucht: Metalloxidvaristoren erfüllen aufgrund ihrer elektrischen Charakteristik und ihres hohen Energieaufnahmevermögens formal die wichtigsten Kriterien, um nachhaltig die Lebensdauer der Maschine beim Betrieb am Frequenzumrichter zu verlängern. Allerdings ist die dabei auftretende hochfrequente und repetierende Beanspruchung so ungewöhnlich, dass dazu keinerlei Bemessungsregeln und Betriebserfahrungen vorliegen und dass im Gegenteil sogar der Beweis anzutreten war, dass Varistoren überhaupt für diesen Einsatz geeignet sind.

Im vorliegenden Abschlussbericht wird in knapper Form über den Projektverlauf sowie über die aus den Untersuchungen hervorgegangenen relevanten Ergebnisse informiert.

8.2. Grundsätzliche Fragestellungen

Zu Beginn des Projektes galt es, folgende Fragestellungen zu klären:

- Wie sieht das grundsätzliche Betriebsverhalten von Varistoren bei schnell ansteigender und permanent repetierender Überspannung aus?
- In welchem Maß ist es möglich, positiv auf die Spannung an der Maschine durch den Einsatz von Varistoren Einfluss zu nehmen?
- Inwiefern wird die Spannungsverteilung in der Eingangssspule der Maschine durch die Varistoreigenkapazität beeinflusst?
- Nach welchen Kriterien sind Varistoren für die vorliegende Anwendung zu dimensionieren?
- Welche Lebensdauer ist für die Varistoren zu erwarten?

8.3. Zusammenfassung der Ergebnisse

Aufgrund der vergleichsweise hohen auftretenden Energien bei geringer anliegender Spannung am Varistor wurden Varistoren verwendet, die eigentlich für den Einsatz in Niederspannungs-Gleichstrombahnsystemen bestimmt sind. Sie zeichnen sich durch eine große Querschnittsfläche bei geringer Gesamthöhe aus (siehe Abb. 2.1), was bei eingeprägten Strömen für geringe Stromdichten und dementsprechend geringe Spannungen sorgt.



Abb. 2.1: Verwendete Varistoren

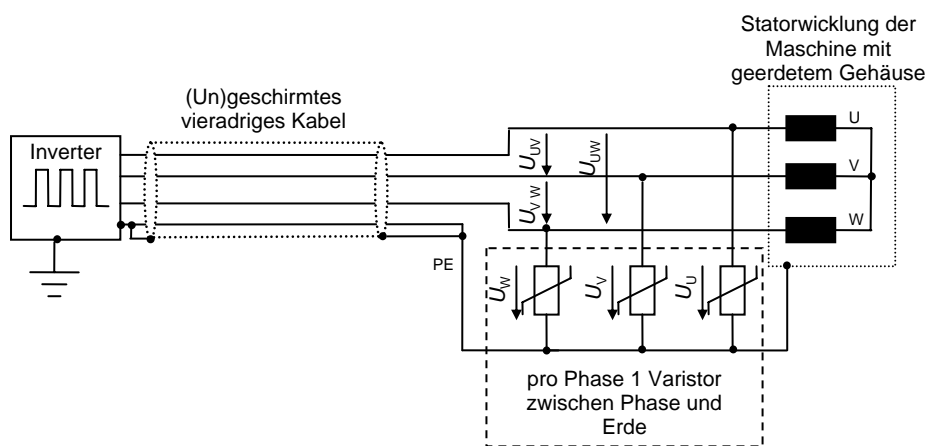


Abb. 2.2: Prinzipielle Schaltung der Varistoren im Antriebssystem

Das Isoliersystem einer Niederspannungsasynchronmaschine wird maßgeblich aus drei wichtigen Teilsolationen gebildet: zum ersten sind die drei Phasen gegeneinander isoliert, zum zweiten ist jede Phase gegen das auf Erdpotential liegende Gehäuse isoliert und zum dritten sind die Drähte der Windungen einer Phase gegeneinander isoliert, wobei die letztgenannte Isolation in der Regel

nur aus der dünnen Lackschicht auf dem Wicklungsdräht besteht und somit das schwächste Glied des Systems darstellt. Daher wurde entschieden, mit den Varistoren die Phase-Erde-Spannung zu begrenzen; das entsprechende Prinzipschaltbild ist in Abb. 2.2 gezeigt.

Das grundsätzliche elektrische Betriebsverhalten soll an Hand von Abb. 2.3 erklärt werden. Zu erkennen sind in grau die verkettete Spannung am Umrichter und die Spannung an der Maschine, wobei der überlagerte, abklingende Wanderwellenvorgang die Amplitude der Maschinenspannung im ersten Moment um ca. 80 % im Vergleich zur ursprünglichen Spannung am Umrichter erhöht. Durch Hinzufügen eines Varistors nach Abb. 2.2 wird die Spannung an der Maschine entsprechend der Spannungs-Strom-Charakteristik des Varistors reduziert – im gegebenen Fall um ca. 250 V. Der Strom durch den Varistor ist dabei zum größten Teil rein kapazitiv, da die Varistoreigenkapazität von ca. 10 nF im Zusammenspiel mit der sehr schnell ansteigenden Spannung zu einem ausgeprägten kapazitiven Strom führt. Lediglich im Bereich des Spannungsmaximums muss der Varistor wegen der hohen Spannung resistiven Strom führen, der zu Verlustleistung und so zu seiner Erwärmung führt. Der Varistor wird dabei im Kennlinienbereich mit der größten Nichtlinearität betrieben, was den gegebenen Anwendungsfall von konventionellen Applikationen grundsätzlich unterscheidet. Ströme im Bereich einiger Ampere kann der Varistor nur führen, da die Ströme sehr kurz (im Bereich weniger Mikrosekunden) fließen. Andernfalls würde die dann sehr hohe eingebrachte Energie schnell zur thermischen Zerstörung des Varistors führen.

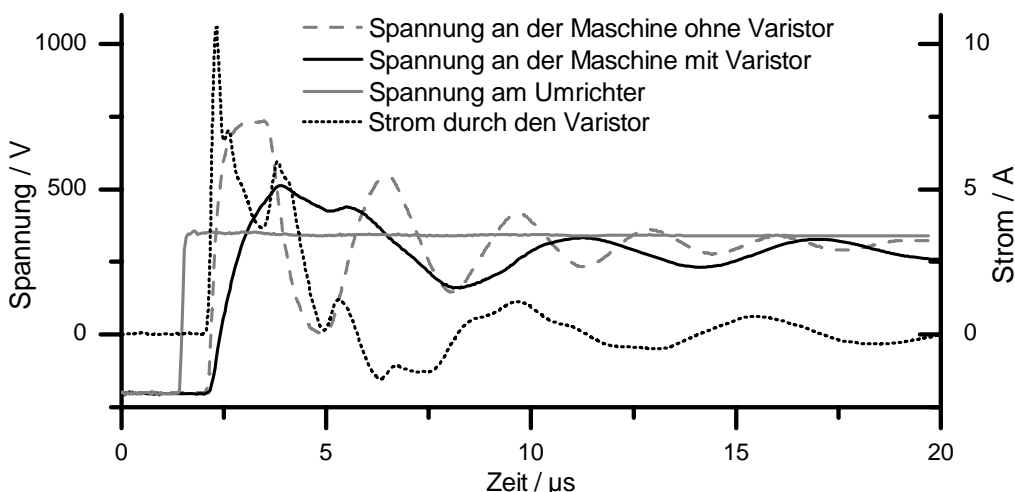


Abb. 2.3: Oszillogramm von Varistorspannung und –strom

Neben der Eigenschaft, die Spannung an der Maschine auf einen für die Wicklung unkritischen Wert zu reduzieren, verlängert der Einsatz von Varistoren die Anstiegszeit der Spannung hin zu Werten, bei denen die Verteilung der Spulenspannungen zwischen den Teilspulen einer Wicklung nahezu linear wird. Die Verlängerung der Anstiegszeit wird durch die große, zusätzliche Kapazität des Varistors hervorgerufen (Varistoren besitzen Dielektrizitätszahlen im Bereich von 300 bis 800). Alle oben beschriebenen Effekte sind in Abb. 2.3 zu erkennen: an einem Motor wurden die Teilspulen einer Phase herausgeführt (Spezialanfertigung der Fa. Hübner), um die einzelnen Spulenspannungen messen zu können. Es ist gut zu erkennen, dass im rechten Oszillogramm die maximale Differenz der Teilspannungen deutlich geringer ist als im linken Oszillogramm – genau das ist der Linearisierungseffekt der Varistorkapazität. Die maximal auftretende Spulenspannung ist zusätzlich in Abb. 2.4 gezeigt. Außerdem ist die Amplitude der Spannung im rechten Bild mit

weniger als 600 V um ca. 200 V geringer als die im linken Bild, was auf den spannungsbegrenzenden Effekt des Varistors zurückzuführen ist.

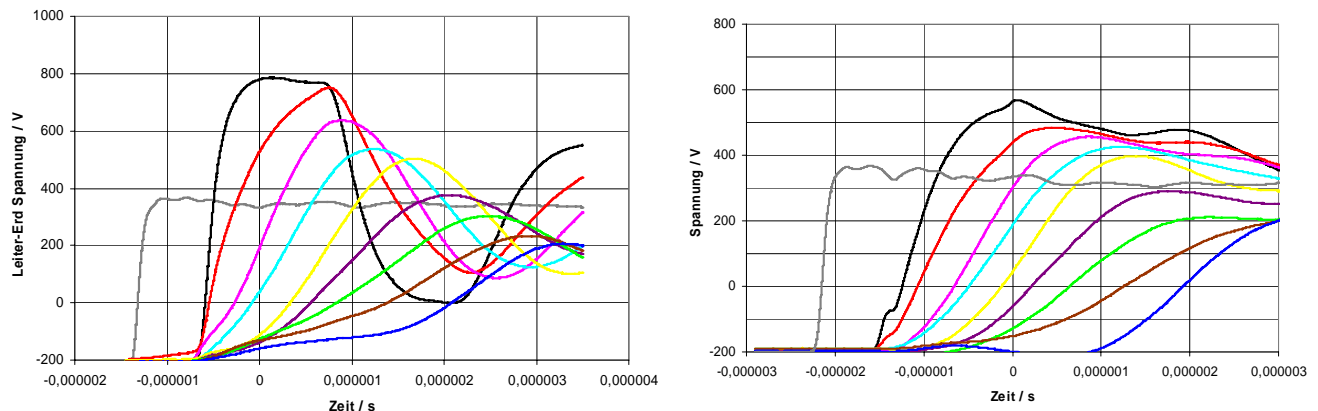


Abb. 2.4: Spannung am Umrichter (grau) und Spannung an der Maschine (schwarz) sowie Spulenspannungen (farbig) ohne Varistor (linkes Bild) und mit Varistor (rechtes Bild)

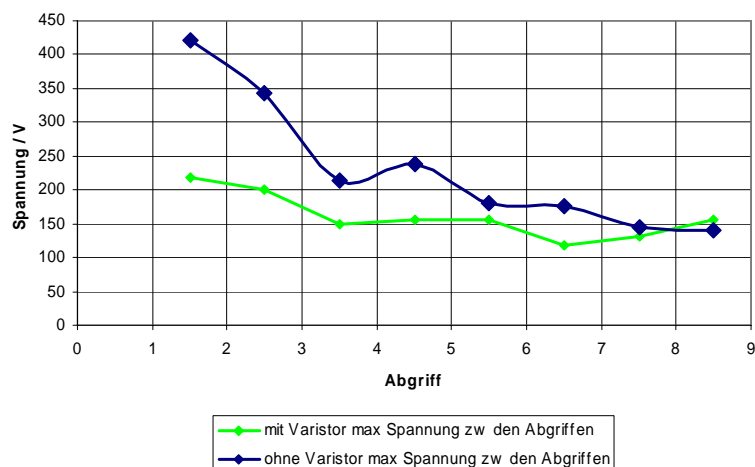
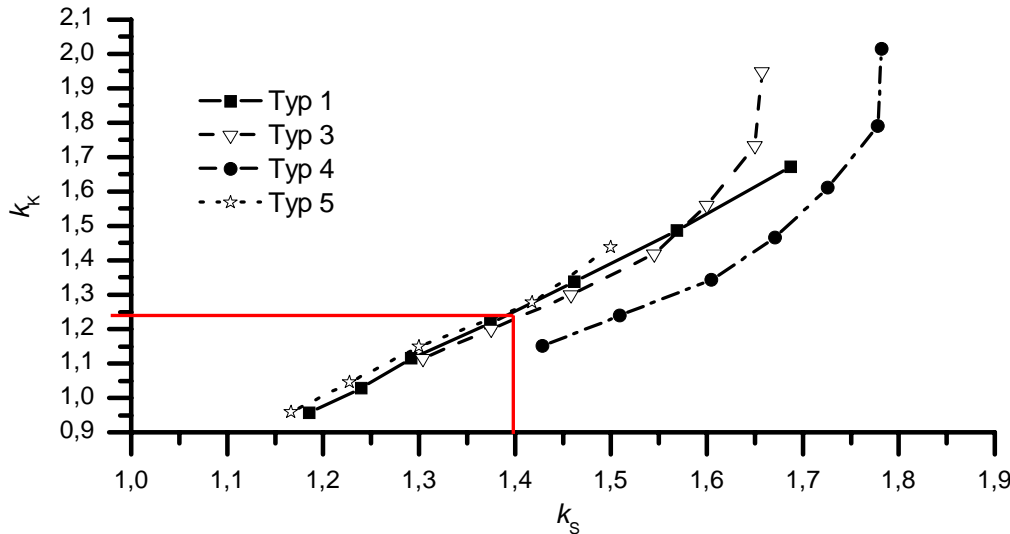


Abb. 2.5: Maximale Differenz der Spannungen zwischen den Abgriffen an der präparierten Maschine ohne und mit Varistor

Der in den Abb. 2.4 und 2.5 gezeigte Fall soll allgemein die Wirkungsweise der Varistoren zeigen. Darüber hinaus ist es notwendig, genaue Dimensionierungsregeln aufzustellen, nach denen die Varistoren an die vorliegende Antriebskonfiguration angepasst werden können. Damit ist es möglich, durch die Auswahl der Varistoren die an der Maschine noch auftretende Überspannung einzustellen bei entsprechender Berücksichtigung der zu erwartenden Lebensdauer der Varistoren selber. Die Dimensionierung ist dabei stark vom verwendeten Kabeltyp bzw. dessen Impedanz abhängig, da eine niedrigere Impedanz einen höheren resistiven Strom im Varistor zulässt und so den Schutzpegel des Varistors erhöht. Anhand der nachfolgenden Abb. 2.6 soll gezeigt werden, wie bei der Dimensionierung von Varistoren für den gegebenen Anwendungsfall vorgegangen werden muss. Dafür wird zunächst erklärt, wie sich die beiden Parameter k_K und k_S definieren: Bei k_K handelt es sich um den Kennlinienparameter, in dem die 10-kA-Restspannung des Varistor ins Verhältnis zur Zwischenkreisspannung des Umrichters gesetzt wird. Bei k_S handelt es sich um den Schutzpegelparameter, in dem die maximal zulässige Amplitude der Strangspannung ins Verhältnis zur Zwischenkreisspannung gesetzt wird: $k_K = U_{10\text{ kA}} / U_{DC}$ and $k_S = \Delta U / U_{DC}$.

Abb. 2.6: k_K in Abhängigkeit von k_S für ein geschirmtes Kabel 4 x 6 mm²

Mit Kenntnis der Zwischenkreisspannung und der maximal zulässigen Amplitude der Spannung an der Maschine lässt sich k_S bestimmen, z. B. $k_S = 1,4$. Aus Abb. 2.6 lässt sich nun für den verwendeten Varistortyp der entsprechende Parameter k_K ablesen, nach dem die 10-kA-Restspannung des Varistors berechnet wird.

Aus den Ergebnissen selbst entwickelter beschleunigter Alterungsprüfungen für Varistoren beim vorliegenden hochfrequenten Betriebsfall, die von der üblichen in den Normen vorgegebenen beschleunigten Alterungsprüfung stark abweicht, wurden Dimensionierungsregeln entwickelt. Details sind den Veröffentlichungen [3], [5] zu entnehmen. Insgesamt ist zu sagen, dass in den beschleunigten Alterungsprüfungen Varistoren verschiedener Hersteller und verschiedener Materialzusammensetzungen auf ihre Belastbarkeit bei schnell repetierenden Überspannungen hin untersucht wurden. Wie zu erwarten, haben neben dem gewählten Material die Spannungshöhe und die Umgebungstemperatur großen Einfluss auf das Alterungsverhalten der Varistoren. Der Grad der (elektrischen) Alterung wird an der Veränderung der $U-I$ Kennlinie festgemacht, wobei sowohl Materialien gefunden wurden, deren Kennlinie sich im Laufe der Prüfung verbessert, als auch solche, deren Kennlinie sich verschlechtert (vgl. Abb. 2.7). Verbesserung bedeutet dabei eine Zunahme der sogenannten Varistorspannung (Klemmenspannung bei 1 mA Gleichstrom), Verschlechterung dementsprechend eine Abnahme

Aus dem zeitlichen Abstand der Alterungsverläufe in Abb. 2.7 lassen sich direkt die Beschleunigungsfaktoren durch die jeweilige Zusatzbelastung ablesen. So könnte man z. B. durch Erhöhung der Zwischenkreisspannung um 100 V, durch Erhöhung der Temperatur um 35 K und Erhöhung der Pulsfrequenz von 3 kHz auf 8 kHz eine Beschleunigung von etwa 30 erreichen, so dass durch eine Prüfzeit von 2000 h eine Realzeit von 6,8 Jahren simuliert wird. Wichtig ist hierbei, dass die Zeitraffung durch Parameterveränderung immer im Zusammenhang mit der angestrebten Belastung in der Realität gesehen werden muss, so dass keine generellen Beschleunigungsfaktoren definiert werden können.

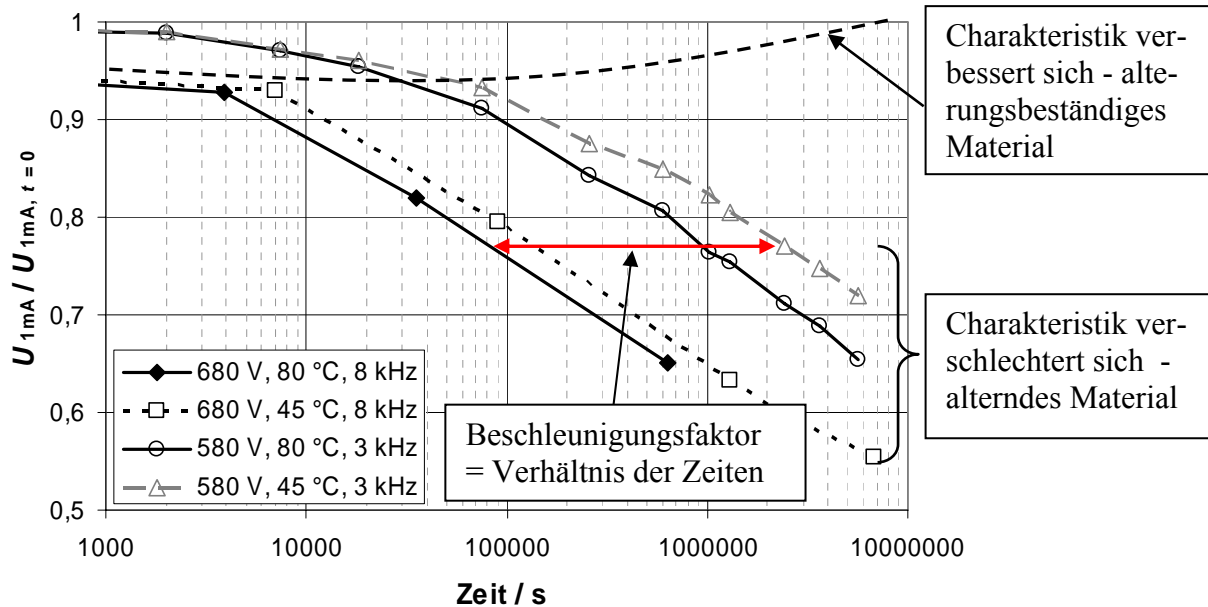


Abb. 2.7: Veränderung der Varistorspannung bei 1 mA Gleichstrom während hochfrequenter Belastung bei verschiedenen Zwischenkreisspannungen, verschiedenen Temperaturen und verschiedenen Taktfrequenzen für Varistortyp 1 (alterndes Material) und Varistortyp 3 (alterungsbeständiges Material)

8.4. Einordnung und Beurteilung der Ergebnisse

Insgesamt sind im Laufe des Projektes alle eingangs gestellten zentralen Fragestellungen beantwortet worden, wobei besonders die Klärung des grundsätzlichen Betriebsverhaltens von Varistoren bei schnell repetierenden Überspannungen sehr zeitintensiv war. Hierbei stellte die Messung von Varistorspannung und -strom sowie die Bestimmung der Verlustleistung im Varistor eine große Herausforderung dar. Darüber hinaus wurde der Einfluss der Systemsparameter wie Kabeltyp, Taktfrequenz und Anstiegszeit der Umrichterspannung anfangs als weniger wichtig eingeordnet, was sich im Fortgang des Projektes als falsch herausgestellt hat, denn eben genau der starke Einfluss der Systemparameter macht die Aufstellung allgemeiner Dimensionierungsregeln für Varistoren äußerst schwierig, so dass versucht wurde, einen Kompromiss zwischen allgemein gültigen Regeln und speziell auf den Anwendungsfall gerichteten Besonderheiten zu finden.

Sehr positiv wird beurteilt, dass entgegen der anfänglichen Einschätzung durchaus Material am Markt erhältlich ist, das alterungsbeständig in Bezug auf hochfrequente Belastung ist. Negativ muss dagegen bewertet werden, dass es nicht möglich ist, näher zu quantifizieren, was genau einen Varistor für diese Anwendung geeignet macht. Von den Herstellern werden Details zum gelieferten Material zum einen grundsätzlich nicht zur Verfügung gestellt, zum anderen haben sie vermutlich selber noch nicht im Detail verstanden, was die charakteristischen Merkmale eines Materials sind, welches in der Anwendung nicht altert. Eigene Analysemöglichkeiten sind bei weitem nicht ausreichend, um diese Fragen selbst zu klären, da nicht nur die Materialzusammensetzung, sondern auch das Herstellverfahren, wie z.B. Sprühtrocknung, Entkohlung und Sinterführung, die Eigenschaften des Materials beeinflussen. Es konnte aber ein Verfahren definiert werden, mit dem sich bereits nach 50 Stunden Versuchzeit die Eignung eines Varistortyps empirisch feststellen lässt.

Die Ergebnisse der beschleunigten Alterungsversuche sind für die Varistorhersteller besonders wertvoll, denn bislang sind noch keinerlei Untersuchungen zum Einsatz von Metalloxidvaristoren bei dauerhaft auftretenden Überspannungen durchgeführt worden. Frequenzumrichter halten in der Antriebstechnik zunehmend Einzug, so dass die hier gewonnen Erkenntnisse mit Sicherheit noch an anderer Stelle Verwendung finden werden.

8.5. Zusammenfassung und Ausblick

Es konnte gezeigt werden, dass Varistoren die in der Anwendung "umrichtergespeiste Antriebe" auftretenden repetierenden Überspannungen dauerhaft begrenzen können. Nach eingehender Klärung der Funktionsweise von Varistoren bei der vorliegenden Betriebsart konnten aus den Ergebnissen der selbst entwickelten beschleunigten Alterungsprüfung Dimensionierungsregeln entwickelt werden. Damit sind zwei wichtige für das Projekt gesetzte Ziele erreicht worden. Außerdem konnte die Langzeitstabilität der Varistoren unter bestimmten Voraussetzungen nachgewiesen werden. Für die Weiterarbeit besteht die Idee, das Überspannungsschutzkonzept auch auf die Mittelspannungsebene auszuweiten, was bis hierhin nur ansatzweise untersucht wurde. Besonders bei Großanrieben hätte der Einsatz von Varistoren gegenüber Filtern (z.B. Sinusfilter) wesentliche Vorteile, da Varistoren nicht im Strompfad der Maschine liegen und somit unabhängig von der Maschinenleistung dimensioniert werden können.

Aus dem Projekt hat sich außerdem ein Folgeprojekt entwickelt, in dem ab Beginn des Jahres 2009 untersucht werden soll, inwieweit es möglich ist, den Effekt der Varistoren als halbleitenden Isolierstoff unmittelbar in der Wicklungsisolation selbst mit Hilfe von Mikrovaristoren auszunutzen.

8.6. Industriepartner

Die Varistoren wurden von den Firmen Toshiba (Japan), Epcos/Siemens (Österreich/Deutschland) und ABB (Schweiz) zur Verfügung gestellt, wobei es sich z. T. um handelsübliche Varistoren und z. T. um für die Applikation optimierte Spezialanfertigungen gehandelt hat. Mit diesen Partnern fanden auch intensive Fachdiskussionen statt.

Die verschiedenen Ausfertigungen von langen Motorkabeln wurden von der Firma Brugg Kabel (Schweiz) gespendet. Außerdem kamen gespendete Frequenzumrichter der Firma Danfoss (Dänemark/Deutschland) und Motoren der Firma Getriebbau Nord (Deutschland) zum Einsatz.

Das gesamte Projekt wurde außerdem sehr intensiv sowohl durch Sachspenden und Personalmittel als auch durch fachlichen Rat durch die Johannes Hübner Stiftung, die Firma Johannes Hübner Elektrische Maschinen (Giessen) und durch deren Mitarbeiter gefördert.

9. Subproject 5: Influencing the voltage slope at the inverter output by modifying the switching behaviour of the IGBT power modules, accomplished by special gate drivers

Prof. Dr.-Ing. Peter Mutschler

Dipl.-Ing. Calin Purcarea

Institut für Stromrichtertechnik und Antriebsregelung, TU Darmstadt

E-Mail: purcarea@srt.tu-darmstadt.de

9.1. Aim of the work and motivation

High frequency phenomena arise at fast switching elements, which deliver high voltage slopes at motor-terminals of 1kV/100ns [1]. Besides the benefit of switching loss reduction and increased switching frequencies for lower harmonics in electrical machines, voltage reflection occurs at motor terminals when feeding the motor via long cables. Also additional parasitic effects like common mode (CM) ground currents and bearing currents occur at the motor side [2]. CM currents lead to a wrong function of protection elements, whereas repetitive bearing currents produce a failure to the bearings. In the frame of this research project simulation models for inverter, cable and motor, to study the problems which occur in adjustable speed drives (ASD) with long feeders, have been developed and adapted to reflect the reality as accurate as possible.

Of course some compromises must be taken into consideration not to increase the complexity and simulation burden. These models are simplified such that they can be easily parameterized from data sheets and characteristics measurements at the subjected device. Using such reliable simulation models, different methods for overvoltage and CM ground current suppression can be investigated “off-line” with minimal effort and time loss. Also using the “off-line” approach, optimum design can be realized by conducting simulations with variation of parameters and finally comparisons with real tests. Usually this methods can be classified corresponding to the considered part of the ASD.

9.2. Project stages and conducted work

A. Building of the Test-bench

In order to design suited time domain simulation models for electrical drive systems, measurements on a real system must be conducted. Thus, the entire system, including the inverter with necessary control equipment, the cable and the motor, was built. The main source of voltage overshoot at motor terminals represents the steep voltage gradient from the inverter output. This is achieved by hard commutated fast switching power semiconductors, e.g. Insulated Gate Bipolar Transistors (IGBTs). The influences of voltage slope are to be observed and measured at the motor terminals.

At the market there exist 6-pack module inverters, including the gate-control, DC-link circuit and the driver at very convenient prices (IPMs). But these IPMs cannot be used in this project, as the accessibility to measure intermediate quantities like the collector current I_C or the collector-emitter voltage V_{CE} for a single IGBT is rather poor or nonexistent. When measuring at output of the inverter module, the superposition of the parasitic module elements affects the measurement results. Also it is necessary to measure the gate-driver output quantities, which correspond directly to the IGBT module and to modify the gate-driver’s characteristic. Therefore, inverter and driving circuits have to be realized in this project in such a way that the necessary measurements are possible. The Inverter-Cable-Motor system was designed and constructed as shown in Fig. 1, where two main parts can be identified: power processing part and information processing part.

A1. Information processing part

The drive control system is PC based, where a real-time software program receives the phase currents from inverter and generates the switching timings, see Fig. 1 (b). To control the inverter via the PC, an interface hardware called AMI (a) (Antriebs-Module-Interface) is used. This hardware provides the switching impulses for each transistor of IGBT module and transforms the phase currents from analogue to digital values. The communication with the control PC is realized with a bus-system, where the data transmission is synchronised to the switching frequency of the inverter. The logic necessary to operate the AMI board is implemented in the CPLD unit. The switching times are calculated by the control-PC and sent from PCI board (b) via a 12 bit parallel PCI-bus interface, which is called “FZI”, to the AMI-board. Both communication protocols with AMI board and CPU are implemented in the FPGA. Also on FZI, the galvanic isolation between the control hardware and the PC using optocouplers is implemented.

It should be mentioned that both AMI board and FZI board were developed at the “Institut für Stromrichtertechnik und Antriebsregelung” within the framework of previous projects, partially supported by DFG funding, and were adapted for the actual test bench. The control itself consists of a C-code programme running under Linux, with a real time module included. A simple Voltage-Frequency characteristic algorithm is used to control the armature voltage as a function of nominal voltage, nominal speed and instant value of speed.

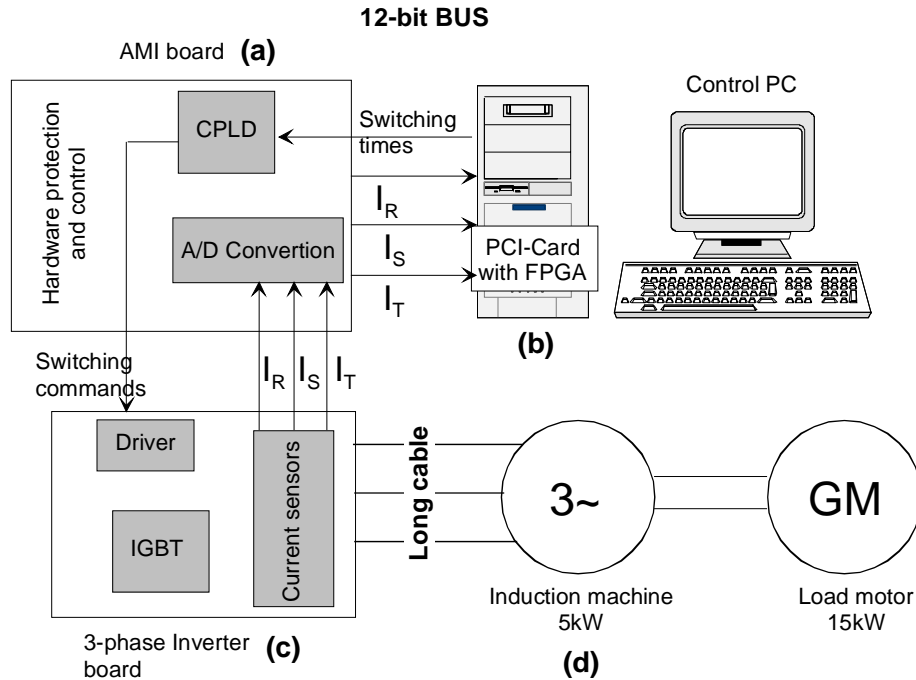


Fig. 1. Inverter-Cable-Motor system and control equipment

A2. Power processing part

On the Inverter Board, Fig. 1 (c), there are the 6-pack IGBT module, the driver, the DC-link capacitor, the bridge rectifier and the current sensors, see Fig. 2 (a).

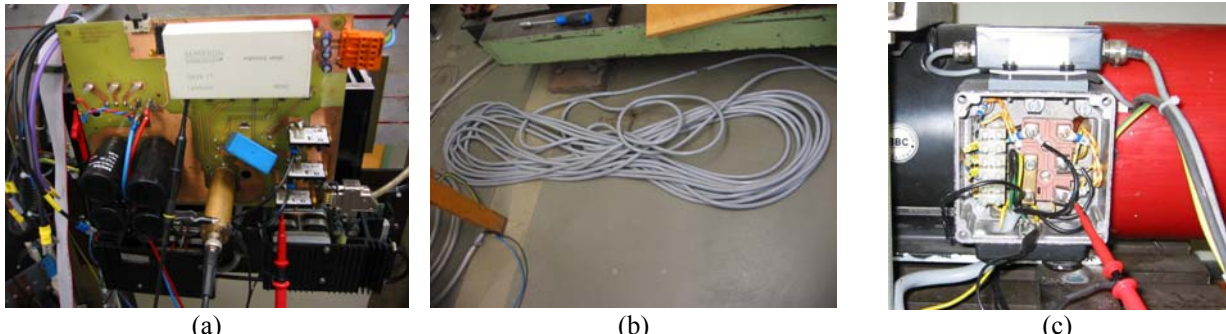


Fig. 2. Practical set-up for Inverter (a), Cable (b) and Motor (c) system.

The AMI board supplies the switching signals to the driver module, commutating further the gate of each IGBT. Gate resistors R_{Gon} for turn on and R_{Goff} for turn off transitions can be unplugged and their value changed, thus changing the switching behavior of the IGBT. The current acquisition is further sent to the AMI board where the measurements are digitized. From the inverter board the motor is fed by a cable, Fig. 2 (b), with variable configurations and lengths. The motor, Fig. 1 (d) and Fig. 2 (c), is a 5 kW squirrel cage induction machine having 17 A rated current. The pin configuration of the 6-pack IGBT module allows measuring of collector current for a single IGBT by means of a coaxial shunt resistor. A coaxial shunt resistor was chosen due to its suitability for high-frequency measurements. The designed value of total resistance (23 mΩ) represents a compromise between reasonable dimensions and voltage output level for maximum current (1.15V for a current of 50A). Manganin® composite (0.1mm layer thickness) was used due to its small temperature-dependency coefficient ($\alpha = 0.01 \cdot 10^{-3} K^{-1}$). This coaxial shunt was also developed at our institute.

B. Inverter simulation model

For the inverter a 6-pack IGBT module (FS35R12YT3 from Infineon®) was used for converting the DC-voltage into a PWM voltage. A behavior modeling of the semiconductor was chosen [3] due to parameterization simplicity, compared with physical properties based models [4]. On one hand, physical dimensions and material properties are very difficult to obtain from manufacturers and on the other hand such models are difficult and complex to implement, as many details and complex equations have to be considered. Therefore, a behavioral equivalent model is suited and the parameterization is realized by measurements and data sheet specifications. For this, several electrical components are used, like inductances, resistors, capacities and voltage controlled current sources.

Using a network simulation program (Simplorer v6.0), the model from Fig. 3 was implemented and simulated. Then the simulations are compared with measurements at the FS35R12YT3 module. There are two aspects to be considered, when creating a behavioral model:

- static and dynamic behavior.

First, the static behavior is characterized by following circuit elements: controlled current source I_{Trans} reflects $I_C = f(V_{GE})$, diode D_{Out_Char} stands for $V_{CE} = f(I_C)$ and for the anti-parallel diode characteristic, $V_F = f(I_F)$, diode D_{Diode} together with R_{ON} is used. Diode D_{Trans} is added to take the extra current I_{Trans} – the I_C as the current delivered by I_{Trans} has a constant value and I_C is conditioned by external circuitry.

Second, for the dynamic behavior one can identify the capacitances between the IGBT terminals: the voltage dependent gate-emitter C_{GE} and gate-collector C_{GC} capacitances, constant collector-emitter C_{CE} and anti-parallel diode junction $C_{D,j}$ capacitances. For simplification C_{CE} and $C_{D,j}$ were chosen constant, whereas the voltage dependence characteristics for C_{GE} and C_{GC} have been parameterized with constant current measurements on the IGBT module. More details on the voltage dependence characteristic and parameterization of gate-emitter C_{GE} and gate-collector C_{GC} capacitances are offered in [5] and the obtained values are shown in fig. 4.

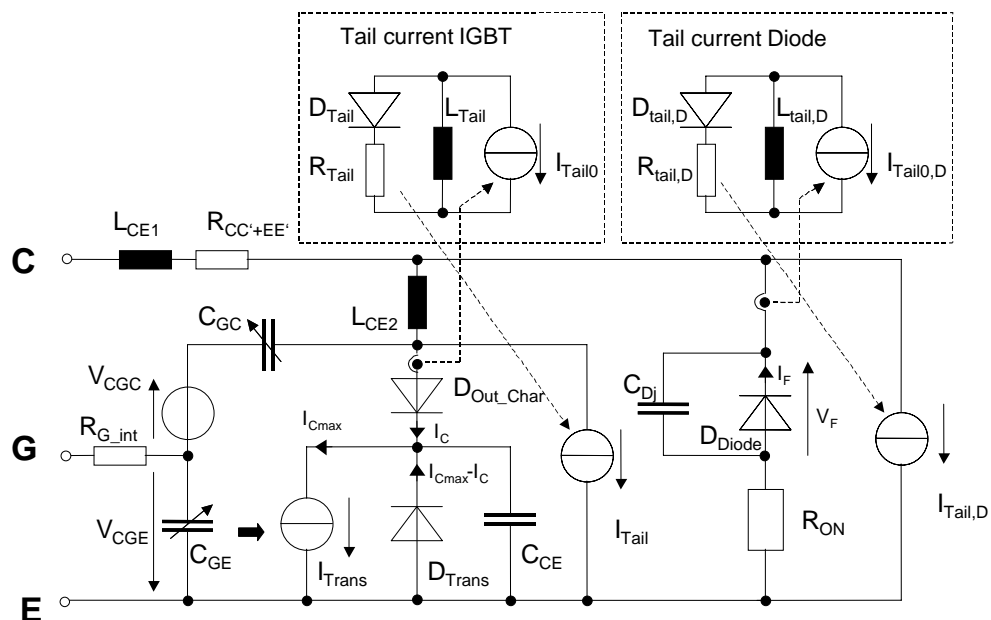
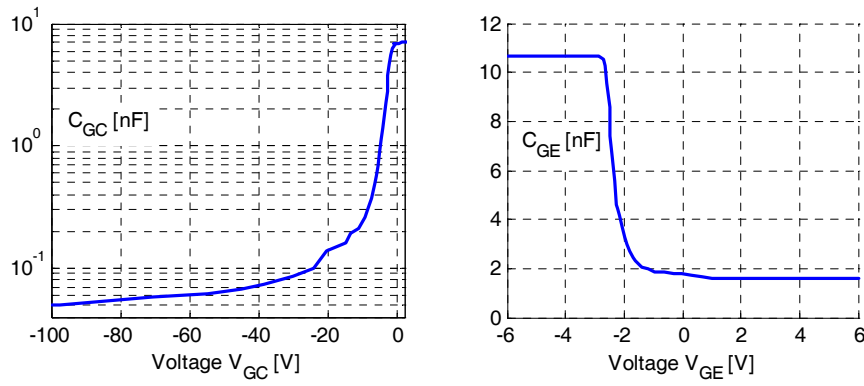
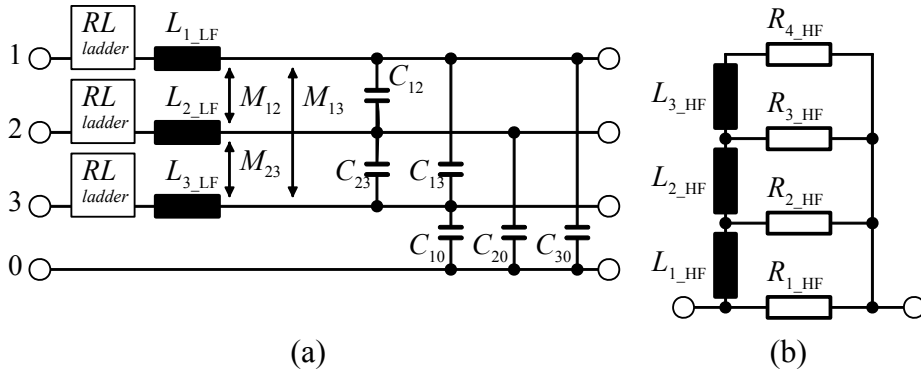


Fig. 3. The equivalent network model for behavioral description

Fig. 4. Voltage dependence capacities C_{GC} (left) and C_{GE} (right).

Further, the connection wire's stray inductances L_{CE_1} , (between out connector and chip), L_{CE_2} (connection between IGBT and anti-parallel diode chip) and resistances R_{CC+EE} are obtained from both data sheet and measurements and added to the model. Optional first order delay elements I_{Tail} and $I_{Tail,D}$ are implemented to simulate the tail current for the diode and the IGBT turn-off transitions. Because there is no significant tail current for the chosen IGBT type (Trench – Field Stop) these blocks are left deactivated. Finally by connecting six IGBT models into a 6-pack bridge and adding the DC-Link capacitors together with their stray resistances and inductances, the inverter model is built.

Fig. 5. Cable Γ -element (a) and ladder circuit for cable losses modeling (b).

C. Cable and Motor simulation model

To drive the induction machine a 34m long LAPP Classic 115CY cable is used. To model the cable, a Γ -circuit was adopted like in [6] (see Fig. 5 (a)) where the inductances for each phase and the coupling capacitances between phases are considered. This equivalent circuit characterizes the cable for 1m length, having totally 34 such segments connected together. To include cable losses a RL ladder circuit [6] was implemented, see Fig. 5 (b). To determine the parameters (summarized in Table I) of one segment three methods were applied in parallel:

- analytical calculation starting from the general equations [4] and applying them to the particular case (LAPP Classic 115CY, 5-core shielded cable);
- Numerical field simulations (FEM) for the same cable with the given geometry (this part was made by Mr. Magdun (TP1-Binder));
- direct measurements at the cable with the impedance analyzer HP 4192A (this part was made in collaboration with Mr. Rocks (TP4-Hinrichsen)).

Table I. Determined parameters per unit length for a 5 conductor shielded cable.

	Analytical method	Measurements	FEM simulations
$C_A = C_{10} + 2C_{12} + 2C_{13}$	167 pF/m	187 pF/m	189,33 pF/m
$C_B = 3C_{10} + 2C_{12} + 4C_{13}$	379,3 pF/m	399 pF/m	434,84 pF/m
$L_A = 2(L_1 - M_{12})$	560nH(LF) / 471nH(HF)	639nH(LF) / 421nH(HF)	560nH(LF) / 286nH(HF)
$L_B = 2(L_1 - M_{13})$	816nH(LF) / 597nH(HF)	815nH(LF) / 472nH(HF)	752nH(LF) / 328nH(HF)

An accurate modeling of the cage induction motor leads to a high precision in estimating the voltage overshoot and oscillation frequency at motor terminals. Same as for semiconductors there are two approaches in modeling an electrical machine: *physical structure* and “*behavior*” based. In this project the motor model from [7] was adopted due to the unknown structure of the available 5 kW asynchronous motor ASM, see Fig. 6. A drawback of this model is the impossibility of representing motor related phenomena like nonlinear voltage distribution along the stator windings and a bearing current estimation. Despite this, voltage reflections and common mode ground current are modeled accurately. Parameterization of this model is realized from direct input impedance measurements [7] using two connection types, i.e. common mode (all phases short circuited against the case) and differential connection (one phase against the other two short circuited). The circuit elements from Fig. 6 are then calculated based on resonant points from Fig. 7.

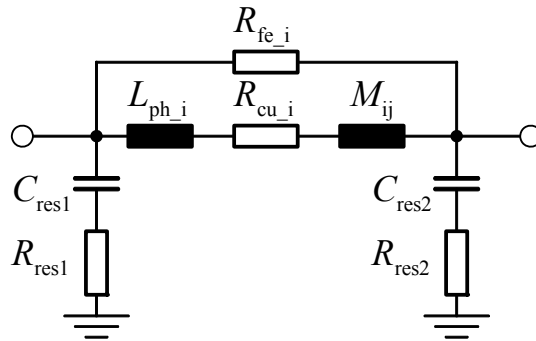


Fig. 6. Per phase electrical machine equivalent circuit model.

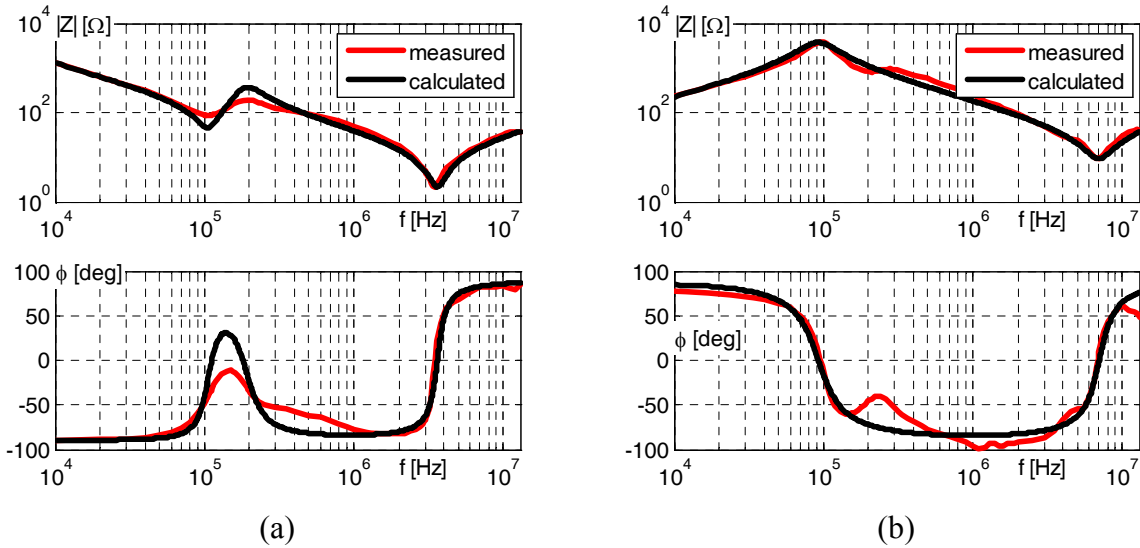


Fig. 7. Amplitude and phase frequency characteristic for a 5kW ASM: (a) common mode and (b) differential mode.

D. Measures against motor overvoltage and CM ground currents

In this research project methods to mitigate parasitic effects in electrical drives were investigated from the inverter point of view, i.e. methods related to the inverter output voltage gradient. Being

the main cause of voltage reflection at the motor terminal, the dV/dt can be either reduced or divided by changing the switching behavior of IGBTs. Also a gradient reduction can be achieved, using passive filters at the inverter output. At motor terminals, passive filters, also called terminators, have the task to match the cable impedance.

D1. Unconventional voltage slopes

New IGBTs offer relative short switching times, e.g. $t_{rise}=100$ ns. This time becomes critical for cable lengths starting with 15 m. Therefore a reduction of the voltage slope is necessary to maintain the rise time above a critical value.

First, the so called passive gate control consists of increasing the gate resistance, which determines the lower gate current level, especially during the *Miller Plateau* phase at turn-on/off and therefore a lower collector-emitter voltage slope dV_{CE}/dt . On the other hand, the switching times will be increased and hence increased switching losses inside the semiconductor will occur, making this solution unpractical. An alternative to the passive gate control of IGBT represents the active gate control [8]. This method requires a complex circuitry to control the gate current and thus the voltage slope. Schematic of such a control circuit is illustrated in Fig. 8 without the dashed-line block. Here the main two parts are observed: dV/dt and dI/dt control. Feedback to control is realized by an additional capacitor C_{dv} for voltage gradient control and an additional inductor L_{dl} (between main emitter and auxiliary emitter clamp) for current gradient control, respectively.

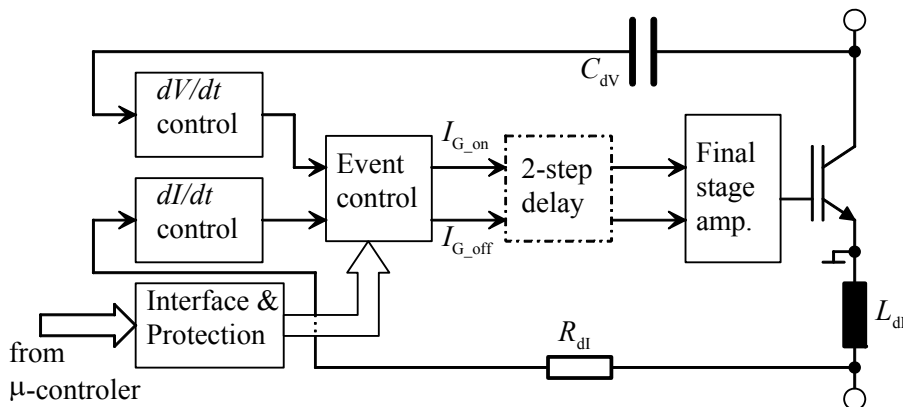


Fig. 8. Active IGBT driver schematic together with additional blocks for 2-step-rise voltage slope

A constant gate current is impressed to the gate and together with C_{GC} the value of dV_{CE}/dt is controlled, but the switching losses increase in same manner as with passive gate control. An improvement is realized, when unconventional voltage slopes are generated. Such voltage slopes, also called “2-step”, were presented in [9], where a mathematical analysis leads to following conclusion: To avoid voltage reflection at the cable, an intermediate step must be impressed at the middle of the slope, i.e. the voltage wave has a intermediary constant value of $V_{DC}/2$ for a determined time interval $T_{delay} = 2 \cdot t_p$, where t_p stands for the wave propagation delay on the cable. In other words, two traveling waves with the same magnitude are applied to the cable, but with a phase shift of 180° . After a traveling $3t_p$ the first wave returns to motor with minimal amplitude. At this instant the second wave traveled $3t_p - T_{delay} = t_p$ and has maximum amplitude, overlapping to the first wave and producing no reflection in the ideal case.

A similar principle can be implemented also by an active gate driving of the IGBT, when adding the “2-step delay” block, see Fig. 8. The task of this block is to cut off the gate current, when $V_{DC}/2$ level is reached and hold it close to 0 for the T_{delay} time interval. In this way the switching loss are reduced by 40%, compared to low constant dV/dt . This is obtained for 20%

overvoltage at 34 m long cable. On the other hand an enormous increase of losses will occur for very long cables. Thus, such a method is suitable for cables less than 30 m long.

D2. Pre- and Post-charge of cable stray elements

Traveling wave phenomena represents the effect of successive charging and discharging of cable stray inductive and capacitive elements. In [10] a method is proposed, where these stray elements of the cable are pre-charged, using a short electric pulse with the magnitude of the DC-link voltage and a pre-determined duration T_{pp} , followed by an off state T_{off} : $T_{pp} = T_{off} = T_{osc} / 6$, where T_{osc} represents the wave oscillation period along the cable.

Actually, the methods works only, if inverter output chokes, with a minimum inductance value, are present. The authors from [10] present the advantage of this method as minimizing factor for inverter output chokes. The value of inductors is directly related to voltage slope. Thus, finding an appropriate value for the output chokes represents a design constraint to assure a voltage slope smaller than the critical one ($t_{rise_crit} = t_p$). By using a pre-charge method, voltage slopes can be maintained bigger than critical values, while reflections are reduced, i.e. the values of inductors can be reduced. Of course there is a minimum value necessary to make this method working: $T_{pp} = T_{off} > t_p$.

If this condition is not fulfilled, the wave propagation delay t_p will have a major effect. In the worst case, when there are no output chokes, no damping is noticeable. Another drawback of this method is the increased switching frequency due to the additional pre-charging pulses, leading to additional losses, which limit the usable PWM switching frequency. Therefore, fast switching semiconductors like MOS-FETs are here preferred.

D3. Inverter output and motor terminal filters

Motor side filters, also called cable terminators, are based mainly on a cable impedance match at the motor terminals in order to avoid voltage reflections. Three topologies were considered and simulated: R-terminator [1], RC-terminator [1] and RC-Clamp filter [11], see Fig. 9. The effects on voltage overshoot reduction and power losses are presented in Table II. The R-terminator is not suitable due to high losses. The RC-terminator presents lower losses than the R-terminator due to a decoupling from HF harmonics through the capacitor. A better solution represents RC-Diode clamp filter, where the voltage overshoot is clamped by a pair of diodes for each phase, and the residual energy is then turned into heat by power Zener diodes. Note that unlike RC-terminator no change in dV/dt at motor terminal occurs.

An improved version of the RC-Diode clamp filter was built and tested on a 5kW induction machine. The upper and lower side of the diode bridge are connected to the DC-link via two additional conductors of the cable (3 conductors for phases L1-L3, 2 conductors for $\pm U_{dc}$). A buffer capacitor is responsible for a constant voltage at the diode bridge during clamping, as the voltage overshoot. Losses are minimized by feeding the energy back to the DC-link circuit. Inverter output filters, also called dV/dt filters, reduce the voltage slope to non-critical values, where only a harmless overvoltage occurs at the motor side. For that purpose a series inductor is used in all cases. From this category three topologies were designed and simulated: RL filter [12], RLC filter [1] and RL Diode clamping filter [11], see Fig. 10. Additional losses on inductive part must be considered to obtain the total losses for this type of filters, therefore no information is presented in Table II for inverter side filters.

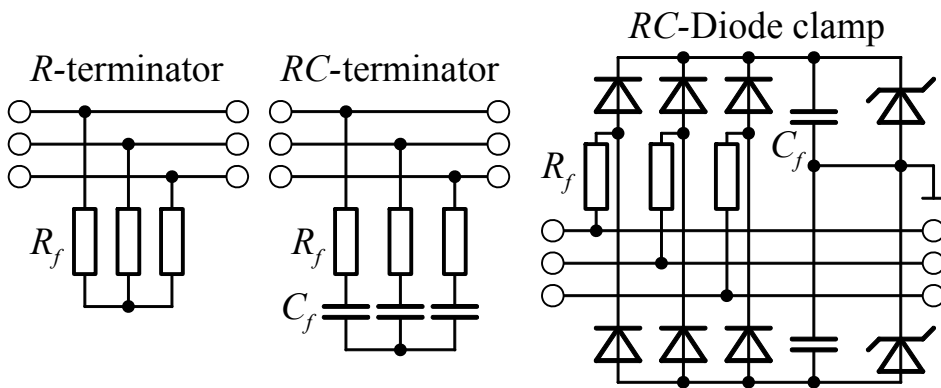


Fig. 9. Motor side filters

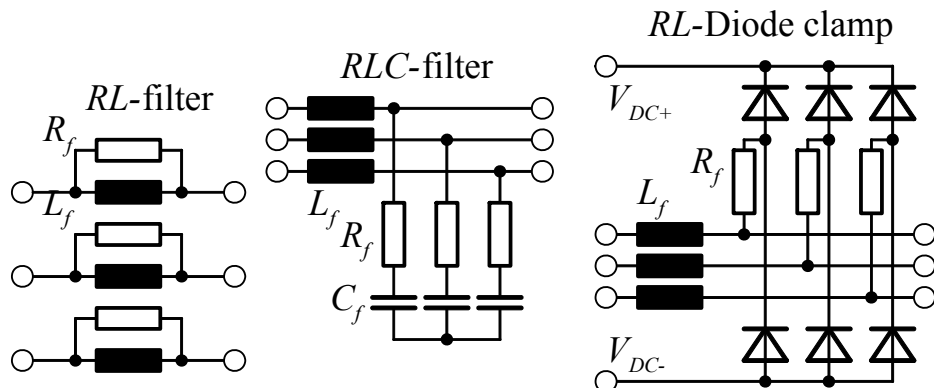


Fig. 10. Inverter output filters.

As a general rule in Table II the voltage overshoot was restricted to around 20 percent of the DC-link value and the IGBTs were switched at 5 kHz.

Table 2. Motor Side Filters for Overvoltage Suppression

	Losses [W]	Overvoltage [%]	
R-terminator	1300	23	simulated
RC-terminator	99,3	19	simulated
RC-Diode clamp	72,3	19,5	simulated
RC-Diode clamp with DC-Link connection	27,5	27	measured
	30	28	simulated

9.3. Simulation and measurement results

The entire inverter-cable-motor system was implemented in a simulation software (SIMPLORER) and the results are compared to measurements. The reliability of the inverter-cable-motor system model is verified by measurements at a real set-up. A 5 kW induction machine with squirrel cage rotor is driven by a voltage source inverter via 34 m long shielded cable. Simulations and measurements are presented in Fig. 11 and 12. A voltage reflection at the motor terminals together with a propagation delay is observed in fig. 11. The common mode ground current is presented in fig. 12. Good agreement between measurements and simulations results was obtained.

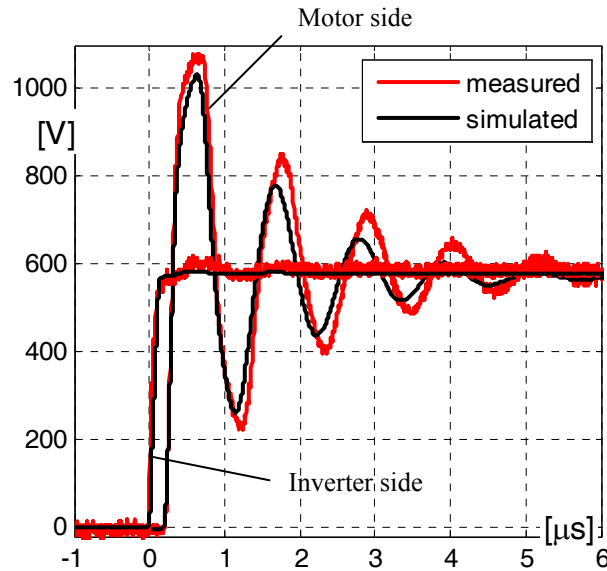


Fig.11. Voltage at inverter output and motor terminal

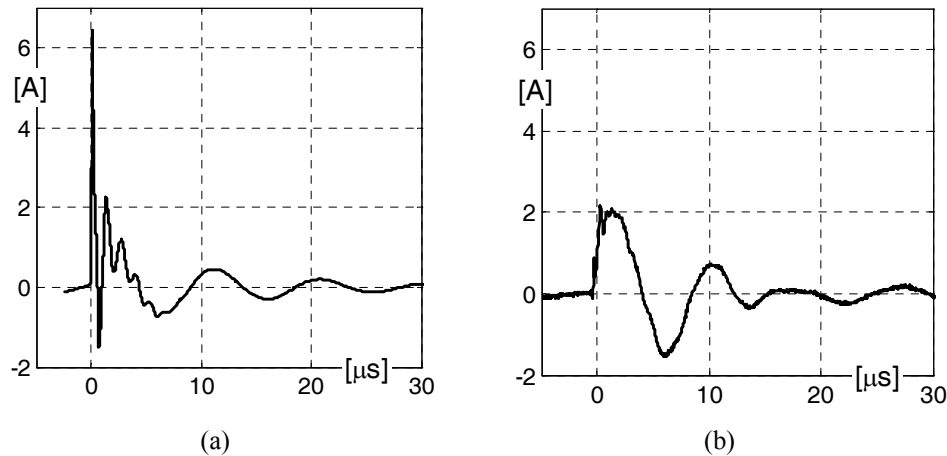


Fig. 12. Common mode ground current: (a) simulation and (b) measurement.

With the developed simulation model, corrective measures were investigated.

First, a “2-step” voltage gradient was implemented using one phase of a 3-level converter, i.e. a buck converter topology with an additional half DC-link switch. A different 100 m long unshielded cable was chosen to avoid output voltage slope distortions by using a large $T_{\text{delay}} \gg t_{\text{rise}}$. At the end of the 100 m long cable an inductive load was used. Simulation vs. measurement results are shown in Fig. 13.

Second, a **pre-charge** method of the cable stray elements was tested at the inverter-motor system, when connecting a 100 m long cable and an arbitrary inductance of 70 μH at inverter output. Thus following parameters are obtained: $T_{\text{pp}} = T_{\text{off}} = 0,933\mu\text{s} > t_p = 0,62\mu\text{s}$. In Fig. 14 simulations are compared with measurements. Notice that in Fig. 14 a small DC-link voltage level was used due to the EMI in the converter’s control electronic. A similar principle is valid for high V_{DC} .

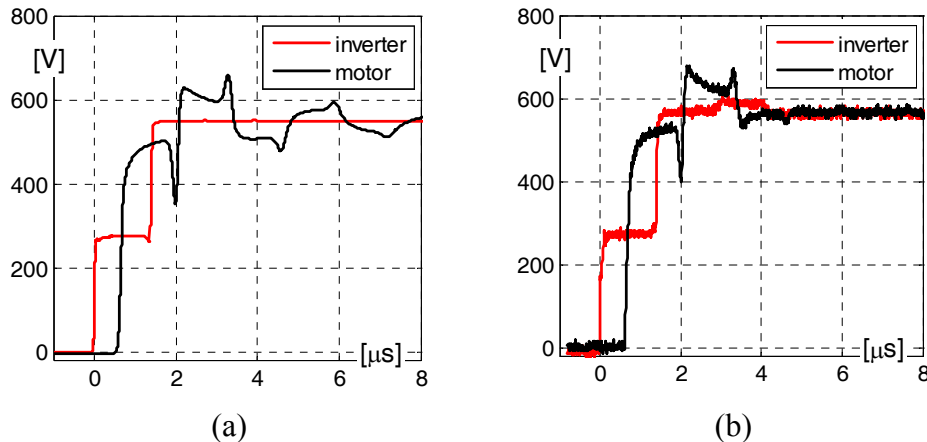


Fig. 13. Voltage at the inverter output and motor terminal by using a “2-step” voltage gradient:
(a) simulation and (b) measurement.

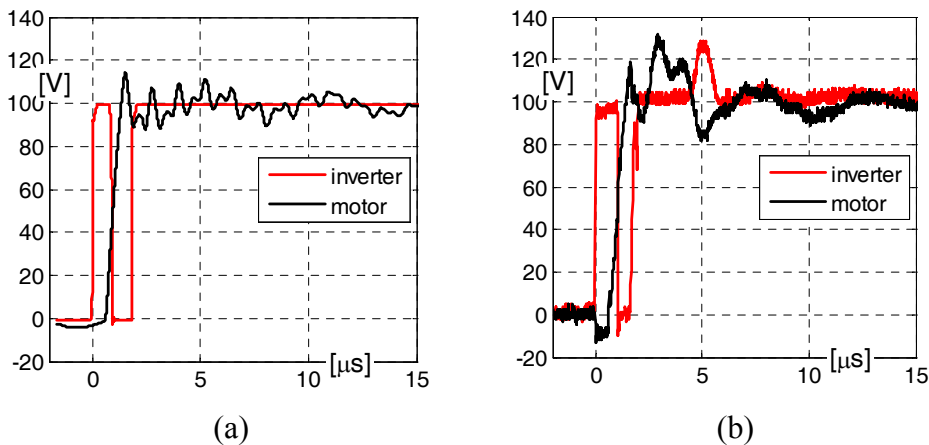


Fig. 14. Voltage at the inverter output and motor terminal, when using a pre-charge method of cable stray elements with an output choke per phase of $70\mu\text{H}$: (a) simulation and (b) measurement.

The use of cable terminators lead to an overvoltage reduction at the motor terminals by matching the motor cable impedance. From Table 2, the **RC-Diode clamp with DC-link connection** features the smallest losses from the studied topologies, therefore a prototype was built and measured. Simulations together with measurements are presented in Fig. 15.

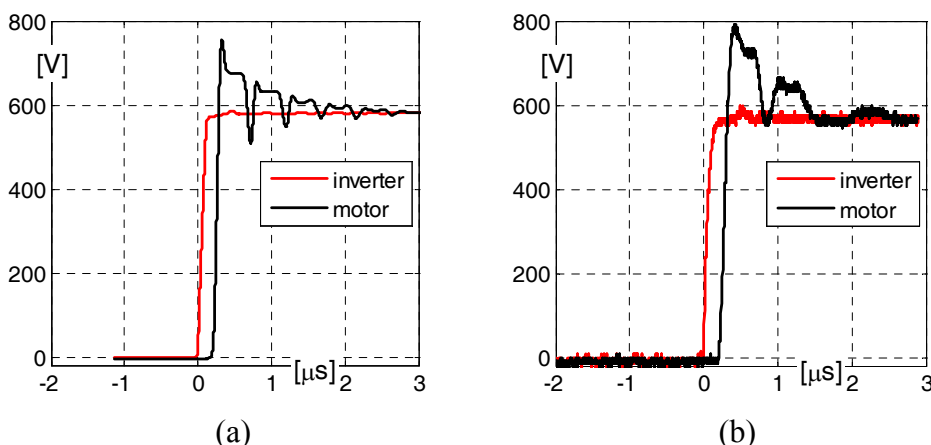


Fig. 15. Voltage at the inverter output and motor terminal, using a RC-Diode clamp filter with DC-link connections:
(a) simulations, (b) measurements.

In Table 3 a classification of inverter output filters [13] is offered, regarding their effects on the line-line and line-earth voltage gradient. Another important problem is the peak in the common mode (CM) voltage, being responsible for inverter-driven bearing currents [2].

Table 3. Motor Side Filters for Overvoltage Suppression

	Line-line voltage	Line-earth voltage
dV/dt filter	Reduced slope	No improvement
Sine-wave filter	Sinusoidal wave form	Slightly reduced slope
EMC filter	Sinusoidal wave form	Sinusoidal wave form

The most effective type of passive filter is the EMI-type, but at the same time it is the most expensive filter. It is able to reduce the voltage overshoot at the motor terminals and CM voltage. The losses however, cannot be avoided, and therefore an optimum design of this filter must be realized, using developed simulation models.

Different types of inverter topologies represent an alternative to a filter adoption. A small study reflects the benefits of resonant converter according to [14], where the voltage slope at the inverter output depends no longer on hard-switched semiconductors but on resonant passive elements. Also, by using the resonant operation as a zero vector voltage and disconnecting the DC-link from the inverter bridge during this period, the CM voltage is reduced to $V_{DC}/6$. Therefore, in a second phase of DFG research project, such type of inverter will be built and comparisons with hard-switched converters with output EMI filters regarding efficiency will be conducted.

9.4. Cooperation and included Diploma, Master and PhD Projects

The research project is part of the research group DFG FOR575 with the main topic “High-Frequency Parasitic Effects in Inverter-fed Electric Drives”. Close collaboration with all involved participants was effective during the whole research project. Important to mention is cooperation with TP1-Binder and TP4-Hinrichsen, regarding the determination of cable and motor parameters, see [15]. Also close cooperation with TP6-Weiland led to stray elements calculation and measurement for IGBT modules and inverter DC-Link construction, see[16]. A Master thesis project [17] was supervised during the research period to obtain a simulation model for active gate drives where a “2-step” voltage gradient control is implemented.

The research activity serves as a PhD project and graduation for the author, Mr. C. Purcarea.

9.5. Conclusions

In the frame of the presented DFG project simulation possibilities for HF phenomena in electric drives were investigated. This offers so called “off-line” investigation methods for common HF parasitic problems, often met in electric drives with long feeder cables. Simplified time domain simulation models based on equivalent networks were chosen and developed, because of difficulty in obtaining physical dimensions and properties for each part of drive system: semiconductors (responsible for the voltage slope), cables (responsible for the wave propagation) and motor (responsible for the wave reflection). Simple parameterization methods were investigated and applied with success and can be further generalized for other components, e.g. the same motor model is valid for induction machines from 2kW up to 200kW. Actually, the main part of the project represents the model description of parasitic effects in electrical drives. Therefore reliable simulation model have to be found and parameterized. Close cooperation in frame DFG FOR575

was very helpful because different parameterization methods were compared, and common results were obtained. Also, different equipment from different institutes was available for measurements and tests.

Being of great importance for HF phenomena investigation, the reliability of simulation models has been checked with measurements on a real setup. It was necessary to design and build of an inverter, because in commercially available inverters is impossible to measure specific quantities like collector current and collector-emitter voltage for single switches. Moreover the self-built setup offers the possibility to control individual switches from a 6-inverter bridge in order to investigate different corrective measures with unconventional voltage gradients against voltage reflections.

Several methods to reduce EMI in drives with long cables have been studied, using the developed simulation models. Comparisons with measurements showed a high reliability of these models presented in Fig. 11 – Fig. 15.

Investigated corrective methods regard the inverter output voltage slope and its influence on the overvoltage at the motor terminals. Thus, the reduction of the voltage gradient can be achieved either by passive gate control (simply increasing the gate resistance) or by active gate control. In both cases a significant increase of losses makes this methods unpractical. By breaking the transition into two, the voltage reflection is suppressed. Still the main drawback remains the accuracy for applying the two different pulses, as it varies strongly with cable length. The use of filters is the most common solution today. With the developed simulation models one can design the filters “off-line” and test them before the construction of a prototype, which results in important saving of time.

In a second phase of this project a resonant converter type will be built and its efficiency measured and verified by comparisons with commercially available EMI filtering solutions.

References

- [1] A. v. Jouanne and P. N. Enjeti, “Design considerations for an Inverter Output Filter to Mitigate the Effects of Long Motor Leads in ASD Applications,” IEEE Trans. On Ind. Appl., vol. 33, no. 5, pp. 1138-1145, September 1997.
- [2] A. Mütze, “Bearing currents in inverter-fed AC motors,” PhD Thesis at Technische Universität Darmstadt, Shaker Verlag, Aachen, 2004.
- [3] A. Wintrich "Verhaltensmodellierung von Leistungshalbleitern für den rechnergestützten Entwurf leistungselektronischer Schaltungen", PhD thesis at Technische Universität Chemnitz, Chemnitz, 1997.
- [4] A. R. Hefner, JR., “An Improved Understanding for the transient operation of the power insulated gate bipolar transistor (IGBT),” IEEE Trans. on Power Electronics, vol. 5, no. 4, pp. 459-468, October 1990.
- [5] S. H. Stier and P. Mutschler "An Investigation of a reliable behavioural IGBT Model in comparison to PSpice and measurement in Hard- and Softswitching applications", EPE'05, Dresden 2005, 6 pages, CD-ROM.
- [6] P. Mäki-Ontto, H. Kinnunen and J. Luomi, “AC motor cable model suitable for bearing current and over-voltage analysis,” Proceedings of International Conference on Electrical Machines, ICEM’04, CD-ROM, no. 365, Cracow, Poland, 2004.
- [7] M. Schinkel, S. Weber, S. Guttowski, W. John and H. Reichl, “Efficient HF modeling and model parameterization of induction machines for time and frequency domain simulations”, Proceedings of APEC '06, pp. 1181-1186, Dallas, USA, 19-23 March 2006.
- [8] C. Dörlemann, “Geregelte Ansteuerung von Insulated Gate Bipolar Transistoren (IGBT) – Anwendung im Frequenzumrichter,” PhD Thesis at Ruhr Universität Bochum, Shaker Verlag, Aachen, 2002.
- [9] S. Lee and K. Nam, “An overvoltage suppression scheme for AC motor drives using a half DC-link voltage level at each PWM transition,” IEEE Transaction on Industrial Electronics, vol. 49, no. 3, June 2002, pp. 549 -557
- [10] H. Deisenroth, “Vermeidung von Überspannungen bei Pulsumrichterantrieben,” ETZ, Bd. 114, Heft 17, 1993.
- [11] P. Feuerstack, and B. Orlik, “EMC filter for PWM inverter-fed motor drives to suppress travelling waves on long power lines between inverter and motor,” EPE'99, Lausanne, Switzerland 1999.
- [12] N. Aoki, K. Satoh and A. Nabae, “Damping circuit to suppress motor terminal overvoltage and ringing in PWM-inverter fed AC mootr drive systems with long motor leads,” IEEE Transactions on Industry Applications, vol. 35, no. 5, September/October 1999, pp.767 - 772
- [13] www.epcos.com, “Application Note on EMC Filters”, pp.18-24, January 2006.
- [14] J. W. Choi and S. K. Sul, “Resonant link bi-directional power converter: part I – resonant circuit,” IEEE Transaction on Power Electronics, vol. 10, no. 4, pp.479-484, July 1995.

- [15] O. Magdun, A. Binder, A. Rocks, .C. Purcarea, B. Funieru “Modeling of asymmetrical cables for an accurate calculation of common mode ground currents,” (accepted to be published at ECCE’09, San Jose, USA)
- [16] Z. Cay, O. Henze and T. Weiland, “Extraction of DC Busbar Parasitics in PWM Inverters”, Proceedings of the 13th International IGTE Symposium on Numerical Field Calculation in Electrical Engineering, pp. 212-217, 22-24 September, 2008, Austria.
- [17] K. S. Muratoglu, “Optimization of switching behaviors for IGBT gate drive units,” Master Thesis No. 1336, Technische Universität Darmstadt, July 2008.

10. Subproject 6: Multi-scale modelling and extraction of parameters in the simulation of inverter-fed drives

M.Sc. Zarife Çay

Prof. Dr. –Ing. Thomas Weiland

Institut für Theorie Elektromagnetischer Felder, TU Darmstadt

cay@temf.tu-darmstadt.de

As an introductory work a 3D model of an electrical machine was setup.

10.1. Simulation of a Reluctance Machine

A 3D finite-element simulation of an exemplary reluctance machine (Fig. 1) is carried out by CST EM Studio® which was developed at our institute to obtain the torque in dependence of the rotor angle. Spurious torque components attributed to the angular resolution of the finite-element mesh are filtered out using the FFT algorithm. A simple control scheme consists of applying a current to a coil whenever a positive contribution to the torque is expected. The equation of motion together with the angle-torque characteristic and the control strategy are integrated in time using a integrator for ordinary differential equations in Matlab.

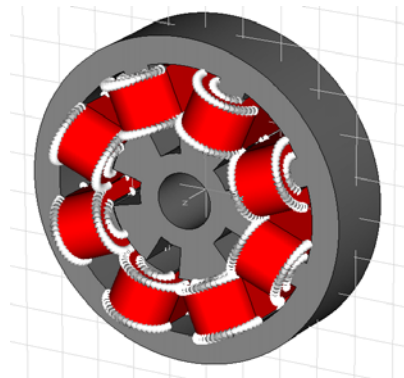


Fig. 1: Simulated reluctance machine

10.2. Electro-Thermal Computations using Finite Integration Technique

10.2.1 Static Electro-Thermal Coupled Simulations

In many electrical engineering applications, dealing with HF parasitic effects, temperature effects cannot be neglected. Then, in the simulation, the electromagnetic (EM) field equation has to be accompanied by the thermal one. Difficulties in their numerical solution arise from the coupling between them and from the nonlinear nature of this coupling. A computational approach is developed to be applied to such engineering problems. The algorithm is validated for a copper rod as an introductory example and a high-voltage varistor in cooperation with *TP-4 Prof. Hinrichsen*. The potential distribution at the steady-state (Fig. 2) indicates the higher resistivity due to the temperature increase in the middle of the rod.

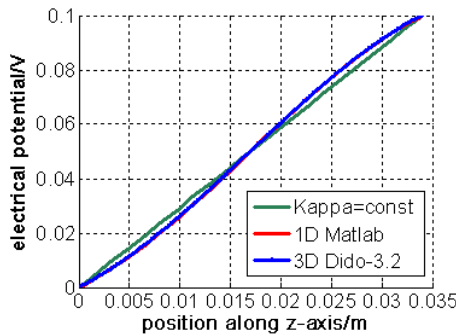
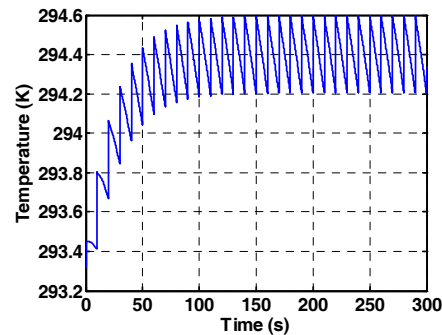


Fig. 2: Electrical potential variation of the copper rod

Fig. 3: Simulated temperature distribution monitored at the center point of the ZnO varistor excited by a voltage pulse train with $V = 1.5967 \times 10^4$ V, $T_{pulse} = 2$ ms and $T_{period} = 1$ s

10.2.2 Transient Electroquasistatic-Thermal Coupled Simulations

We have focused on the design and implementation of iterative algorithms for the solution of loosely coupled nonlinear transient electroquasistatic-thermal problems. The thermal excitations in this study are electromagnetic losses due to pulsed voltage excitations. The partial differential equations describing the system are discretized in 1D space using the finite integration technique (FIT). The spatial discretization results in ordinary differential equations that are further discretized in time by the theta method for the electroquasistatic (EQS) model and by an explicit scheme for the thermal model. The remaining nonlinearities are resolved by a *Picard* iteration. The simulations of the copper rod and the ZnO varistor reflect the multi-physical behavior of these devices (Fig. 3). The time integration procedure reaches a steady-state situation, indicating that the explicit method applied to the thermal system is stable.

10.2.3 Transient Electroquasistatic Simulations

The 2D transient EQS simulations of a feeding cable joint (Fig. 4) described in [4] are done for two different models (Fig. 5 and Fig. 6). The first model has linear material properties in each region whereas the second model has a nonlinear electrical conductivity $\kappa(E)$ in the mastix region.

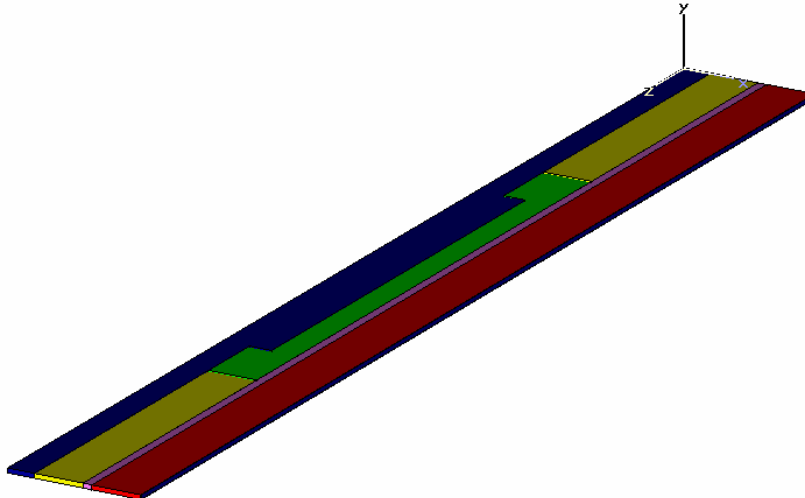


Fig. 4: 2D CST EM Studio® model of the distribution cable joint (The green region is the mastix region)

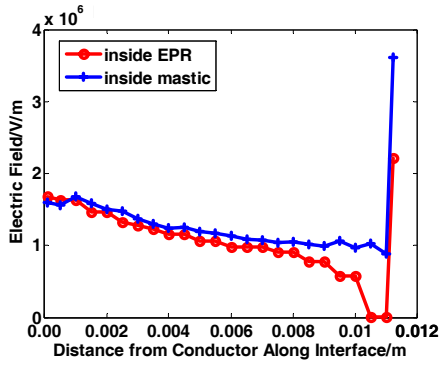


Fig. 5: Electrical field distribution of the linear distribution cable joint model with linear dependence of the conductivity of insulation matrix of the electric strength $\kappa(E)$

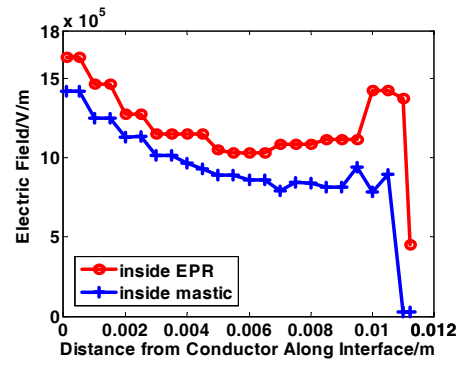


Fig. 6: Electrical field distribution of the linear distribution cable joint model with non-linear dependence of the conductivity of insulation matrix of the electric strength $\kappa(B)$

10.3 Modeling and Simulation of Rolling Element Bearings in Inverter-Fed AC Motors

Insulated Gate Bipolar Transistors (IGBTs) are the power switches of choice for many today's inverters. Fast switching of these devices enables much better operation performance. But it also induces harmful currents, which flow through the bearings, causing premature motor bearing failures. This study analyzes the linear electroquasistatic field behavior of motor bearings in 2D in the time harmonic and transient case. It computes the bearing capacitance for the EDM (Electric Discharge Machining) bearing current, as well. The calculation of the capacitance of motor bearings is essential to estimate the bearing voltage and the endangerment of the bearing due to EDM bearing currents. Based on these estimations, convenient mitigation methods could be determined already in the design phase of an inverter-fed ac motor, if necessary, which ensure safe drive operation,

10.3.1 An Extended Circuit Model of a Roller Bearing

An extended equivalent circuit model of a roller bearing is developed. Its parameters are evaluated analytically in 1D and computationally in 2D. Only half of the bearing is modeled by utilizing the symmetry property. It is partitioned into three sections. Each steel (white) subsection is represented as a resistor, each lubricant (yellow) subsection is represented as a capacitor (Fig. 7). So, no punch through of the bearing is considered, which is assumed to be in a healthy state.

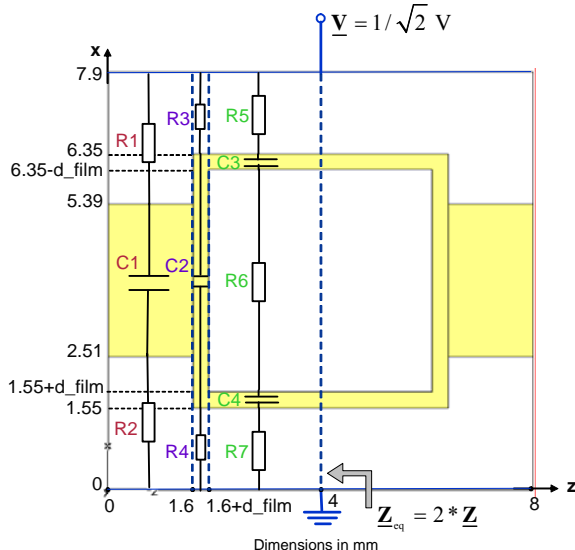


Fig. 7: Top view of the 2D CST EM Studio® model of a roller bearing with dimensions, and circuit parameters of each subsection

	Analytical	Computed
$R1 / \mu\Omega$	15.2	$10.8 \rightarrow 13.2 \rightarrow 487$
$X_{C1} / G\Omega$	9.11	$1.13 \rightarrow 15.8 \rightarrow 0.68$
$R2 / m\Omega$	0.31	$6.30 \rightarrow 0.22 \rightarrow 8.51$
$R3 / m\Omega$	6.95	$7.42 \rightarrow 7.21 \rightarrow 6.04$
$X_{C2} / T\Omega$	13.5	$0.014 \rightarrow 3520 \rightarrow 0.016$
$R4 / \Omega$	0.23	$0.14 \rightarrow 0.16 \rightarrow 6.29$
$R5 / \mu\Omega$	5.80	$5.97 \rightarrow 5.87 \rightarrow 5.51$
$X_{C3} / M\Omega$	2.51	$2.51 \rightarrow 2.50 \rightarrow 2.46$
$R6 / \mu\Omega$	37.4	0 (Due to the truncation error!)
$X_{C4} / M\Omega$	10.3	$10.3 \rightarrow 10.2 \rightarrow 10.1$
$R7 / m\Omega$	0.19	$0.12 \rightarrow 0.13 \rightarrow 5.40$

Table 1: Analytically and computationally calculated circuit parameters of the extended model for the roller bearing

Three different currents (current entering the subregion, current flowing through the intermediate cylinder of the subregion and current leaving the subregion) and the potential difference of each subregion are roughly estimated from the results of the time harmonic simulator. By dividing the voltage by three different currents, three different values are obtained for each circuit parameter. The real values must be somewhere in between. As seen from Table 1, the computed parameter values match the analytically calculated ones fairly well.

10.3.2 Time Harmonic and Transient Analyses of a Ball Bearing in 2D

a. Time Harmonic Analysis

A time harmonic bearing voltage, whose peak voltage is well below the breakdown threshold voltage of the lubrication film, is applied between the cylindrical surfaces at r_{\min} and at r_{\max} of the ball bearing. The potential distribution over the bearing cross section is simulated at different time instants (Fig. 8). The locations of the used monitor points a ÷ n are shown in Fig. 9. At these space points, the magnitude of the volume current density is monitored (Fig. 10). The calculated and computed bearing currents, impedances and capacitances for the roller and ball bearing are given in Table 2.

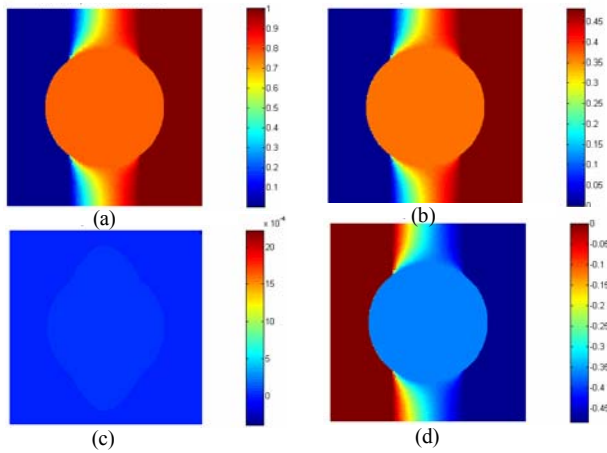


Fig. 8: Calculated potential distributions at: (a) $t = T$, (b) $t = T / 6$, (c) $t = T / 4$, (d) $t = 2 * T / 3$

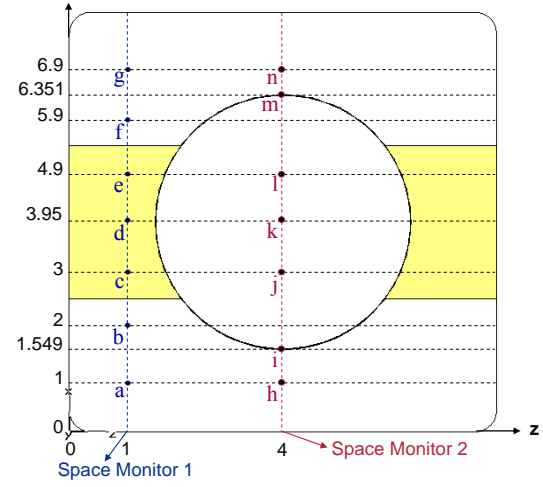


Fig. 9: Location of the monitor points a ÷ n
(Dimensions in mm)

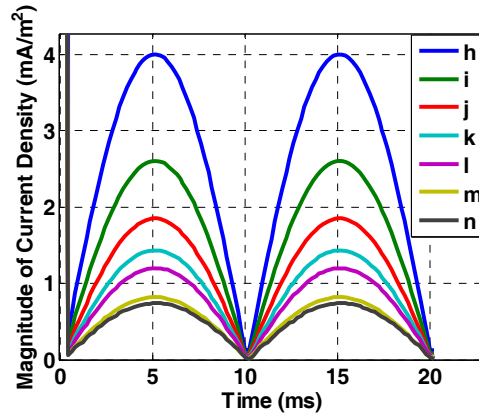
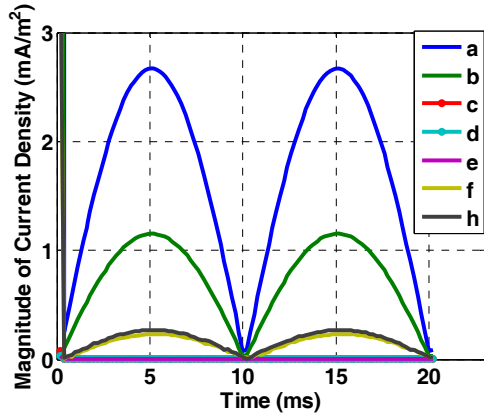


Fig. 10: Calculated magnitude of the volume current density at different locations a ÷ n

	Analytical	Computed	
	Roller Bearing	Roller Bearing	Ball Bearing
I_b / nA	$j * 111$	$j * 168$	$j * 113$
$Z_b / \text{M}\Omega$	$-j * 6.38$	$-j * 4.21$	$-j * 6.26$
C_b / pF	499	756	508

Table 2: Calculated capacitive bearing current, impedance and capacitance at 50 Hz

b. Transient Analysis

A pulse train bearing voltage, whose voltage level is well below the breakdown threshold voltage of the lubrication film, is applied between the cylindrical surfaces at r_{\min} and at r_{\max} of the ball bearing (Fig. 11). The potential distribution over the bearing cross section is simulated at different time instants (Fig. 12). The location of the used monitor points a ÷ n are shown in Fig. 9. At these space points, the magnitude of the volume current density is monitored (Fig. 13).

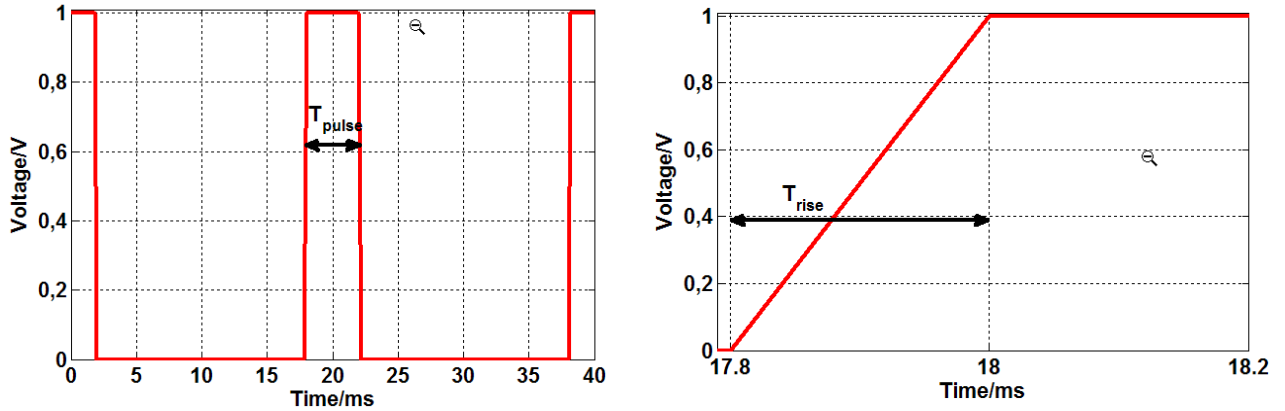
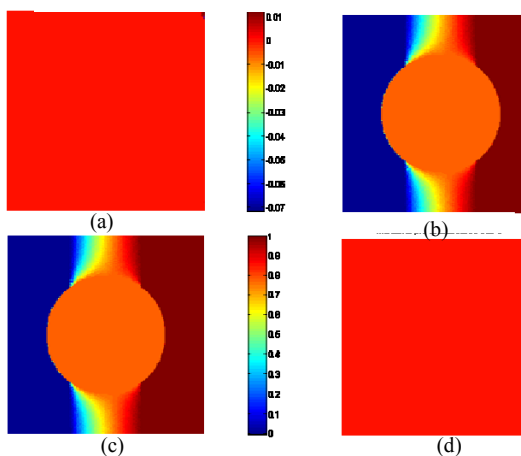
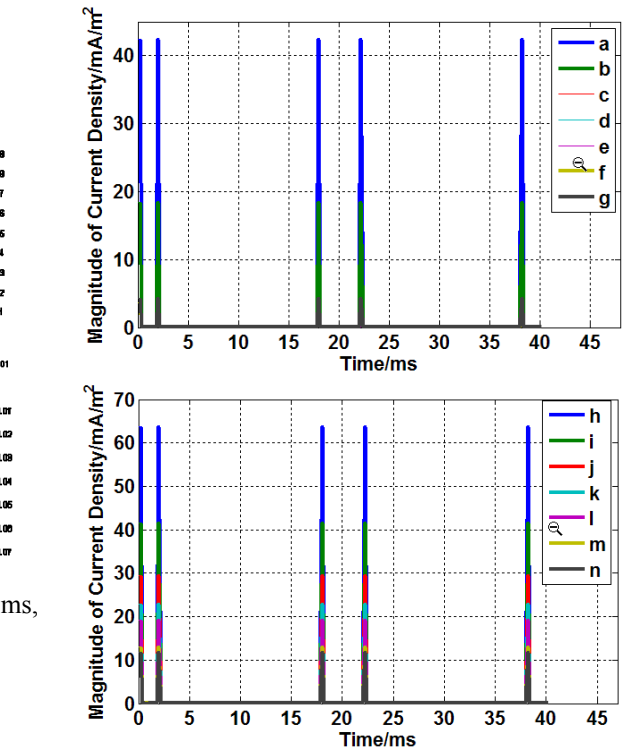
Fig. 12: Applied voltage: $V_{\text{peak}} = 1 \text{ V}$, $T = 20 \text{ ms}$, $T_{\text{pulse}} = T / 5 = 4 \text{ ms}$, $T_{\text{rise}} = T / 100 = 0.2 \text{ ms}$.Fig. 12: Potential distributions at: (a) $t = 17.8 \text{ ms}$, (b) $t = 18 \text{ ms}$, (c) $t = 22 \text{ ms}$, (d) $t = 22.2 \text{ ms}$ 

Fig. 13: Magnitude of the volume current density

c. Conclusions

Conclusions based on Table 2:

- The analytical and simulation results verify that a bearing can be modelled by a single capacitor without losing much accuracy, as long as the lubrication film is insulating.
- The bearing capacitances before the breakdown of the lubrication film are found to be several hundred picofarads. The values match the typical bearing capacitance values reported in [5] for a 2D model. In a 3D model, the contact area and hence the capacity of the bearing is smaller.
- The capacitive bearing current that flows through the bearing, before the lubrication film breaks down, has no unfavorable effects on bearing lifetime because of its low amplitude.

Conclusions based on Fig. 8, 10, 12 and 13:

- Since steel is a good conductor, the races and the rolling element of the ball bearing behave approximately like equipotential volumes.
- The electric field strength inside the steel parts produces very small conduction current density, which is comparable to the displacement current density in the insulating film. The displacement current density between the races, on the other hand, is extraordinarily small.
- The time derivative of potentials generates a phase shift between the time harmonic voltage applied and the resulting volume current density.
- The time derivative of potentials generates impulses in the volume current density at the on and off instants of the pulse train voltage source. The physical explanation of this phenomenon is as follows: The current flowing through a capacitor has an exponential decay during charging and discharging states. The electrical behaviour of the bearing can also be approximated by a capacitor in series to a small resistor. Since the time constant of the bearing is extremely small, the current has a form of an impulse, having extremely small duration, at on and off time instants.

10.3.3 Bearing Capacitance Computation in 3D

The thickness of the lubricating film is determined by the laws of hydrodynamics and depends on the operational parameters of the motor such as speed, bearing axial and radial load force, temperature and surface roughness, and on the mechanical properties of the grease [7]. This makes the accurate calculation of the bearing capacitance a rather complex task. A simplified approach assuming a fixed geometry and a constant minimum film thickness is used here for the prediction of the bearing capacitance. First, the bearing capacitance is evaluated for a minimum lubrication thickness of $10 \mu\text{m}$. Then, a second calculation is done assuming that due to the rotor movement the outer race is fixed, but the inner race is shifted $2*7 \mu\text{m}$, the cage and all balls are shifted $7 \mu\text{m}$ in $-y$ direction.

The capacitance is independent of the frequency of the source signal. Therefore, the electrostatic solver of the CST EM Studio® is used to compute the bearing capacitance. The inner race, outer race and rollers are put to constant potentials. The electric field energy stored in each component is calculated. From this energy, the total bearing capacitance is computed as 265 pF for the first case and 271 pF for the shifted case. The shifting effect on bearing capacitance is very small.

10.4 Extraction of DC Busbar Parasitics in PWM Inverters

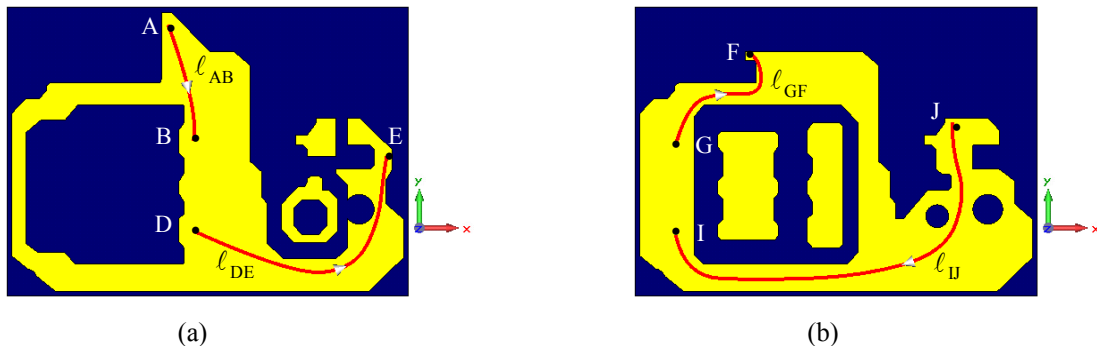
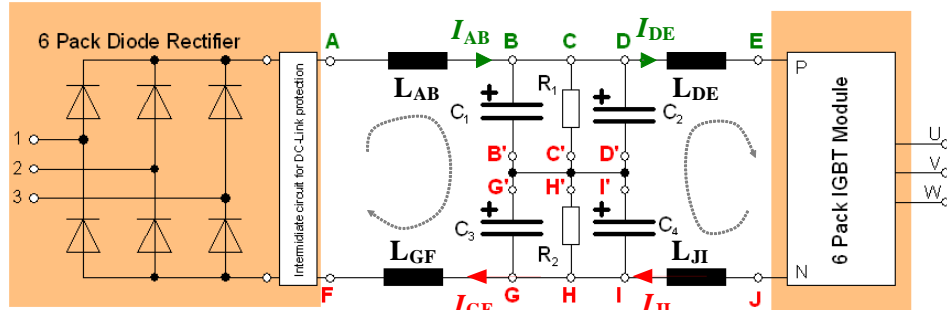
10.4.1 Power Busbar

The power busbar used in this study is a single printed circuit board (PCB), composed of two very thin copper layers and an insulating substrate between them. Table 3 displays the material properties and the thicknesses of each DC bus layer. The top and bottom view of the inverter PCB are depicted in Fig. 14.

The role of the busbar in an inverter is to link power devices electrically and to carry current. In Fig. 15, the corresponding network model is given for a better understanding of the functioning of the DC link. In both figures, the current flowing directions are depicted, as well as the pin layout. The pins A and F connect the rectifier diodes with the DC bus. The connection between the IGBT module and DC bus is provided via the pins E and J.

Material	ε_r	μ_r	$\sigma/(MS/m)$	Thickness/mm
Copper	-	1	58	0.035
Epoxy	4	1	0	1.5

Table 3: Material properties and dimensions of DC bus layers

Fig. 14: Current flowing paths l_{DE} , l_{AB} , l_{GF} , l_{IJ} and corresponding lengths on (a) top and (b) bottom copper layer of DC busFig. 15: Schematic of the 50A/600V (rated) busbar designed by Dipl. –Ing. C. Purcarea, TP5-Prof. Mutschler, showing the electrolytic capacitances C_1, \dots, C_4 and parasitic inductances L_{AB}, \dots, L_{JI}

10.4.2 Power Busbar Parasitics

The current paths on the copper layers have stray inductances. Table 4 presents the parasitic inductances to be determined. The other paths (B-C-D, G-H-I, B'-G', C'-H', D'-I') are relatively small compared to the ones of Table 4. Therefore, their stray inductances are not taken into consideration so as to reduce the computational load of the parameter extraction.

L_{AB} of path A-B	L_{DE} of path D-E	Top copper layer
L_{GF} of path G-F	L_{IJ} of path I-J	Bottom copper layer

Table 4: Dominant copper paths of DC Bus and their stray inductances to be determined

10.4.3 Parasitic Extraction Approach

The low frequency (LF) solver of CST EM Studio®, which regards the skin and proximity effect, is preferred for the simulations. The details of the simulation approach are given in Table 5. The needed open boundaries are approximated by putting a large air space around the DC bus. The electrolytic capacitors, IGBT and diode packages are not modeled to reduce the computational complexity. Instead, they are replaced by thin wires in the electromagnetic model to complete the current loops to satisfy the Ampere's law. The solver computes the closed magnetic energy W_{mag} .

The loop inductances, L_{ABGF} and L_{EDJI} , are calculated from the magnetic energy, W_{mag} , by the formula below:

$$L_{loop} = \frac{2 \cdot W_{mag}}{(I_{rms})^2}, \quad (1)$$

where I_{rms} is the root mean square (rms) value of AC current excitation.

The path inductances, L_{AB} , L_{GF} , L_{DE} and L_{JI} , should be derived from the loop inductances. The analytical formulas for a simple busbar configuration given in [7] reveal that both internal and external inductances are directly proportional to the length of the current paths. Therefore, each loop inductance might be split into two inductances according to the current path lengths. As a matter of fact, the current on the DC bus does not take a simple path, but instead distributes itself on the entire copper layer. To simplify, it is assumed that the current follows nearly the shortest distance between two pins on the conducting sheet. These paths and their lengths are shown in Fig. 14. The splitting equations are as follows:

$$L_{ABGF} \approx L_{AB} + L_{GF} \text{ and } \frac{L_{AB}}{L_{GF}} = \frac{\ell_{AB}}{\ell_{GF}}, \quad (2)$$

$$L_{DEJI} \approx L_{DE} + L_{JI} \text{ and } \frac{L_{DE}}{L_{JI}} = \frac{\ell_{DE}}{\ell_{JI}}. \quad (3)$$

In the above derivation, the inductances of the wires in the EM model are not considered. So the results for the path inductances are overestimated. The maximum level of EMI could, however, be predicted using them.

CST EM STUDIO®	
Solver Type	LF Frequency Domain
Solver Equation	Magnetoquasistatic (MQS)
Mesh Type	Tetrahedral Mesh
Adaptive Mesh Refinement	Yes
Number of Mesh Cells	Up to 1 Million

Table 5: Simulation approach

10.4.4. Verification of the Parasitic Extraction Approach

For simple backplane geometries, the loop inductances are estimated at 1 MHz by the help of the method of moments (MoM) and from the measurements in [8]. One of the configurations is adopted as our test structure to confirm the accuracy of the extraction approach. Fig. 16 illustrates the test structure and the current flowing direction. The sample is composed of two planar copper sheets in parallel with each other. The interspace is 1 cm. The width of the copper plates in the x-direction is 10 cm. The length is 20 cm in the y-direction, and the thickness of sheets is of 1 mm. The method introduced in the previous subsection is employed to extract the loop inductance of the structure. A current path, indicated by a (red) wire with a cone in its center, is applied as the excitation at one end (Fig. 16). At the opposite end, a thin wire is used to connect the bottom and top plates. So that a loop is constructed for current flow. The extracted loop inductance is displayed together with the computed and measured results of [8] in Table 6. The good agreement between the results confirms the reliability of the proposed approach.

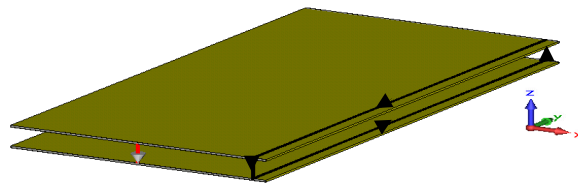


Fig.16: CST EM Studio® model of the backplane. Solid arrows show the direction of the current flow.

	Proposed Method	MoM	Measured
L_{loop} / nH	40.7	42.9	42.2

Table 6: Loop inductances

10.4.5. Simulation Results of the DC Bus

Figure 16 and 17 show the variation in the leakage inductances of the power busbar with respect to frequency. The resulting inductances are also displayed in Table 7 for three different frequencies. The expected reduction in the inductances due to the increase in the frequency (skin effect) is observed in the results (See Fig. 17, 18 and Table 7). This reduction becomes slight at higher frequencies as the external inductance becomes predominant.

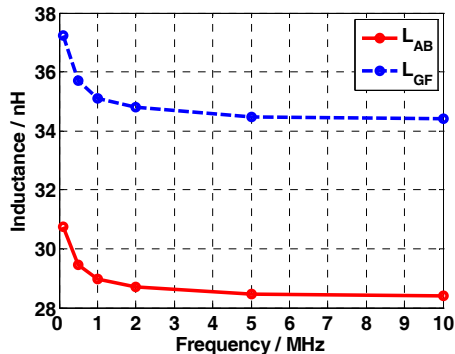


Fig. 17: Calculated inductances of the current paths AB and GF derived from the loop inductance L_{ABGF} .

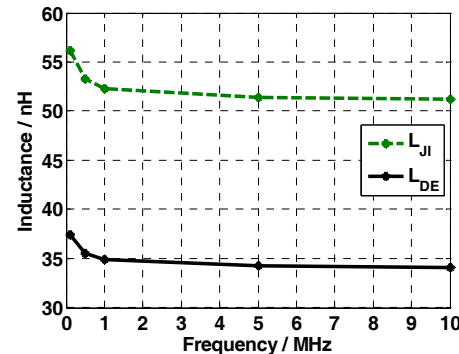


Fig. 18: Calculated inductances of the current paths DE and JI derived from the loop inductance L_{DEJI} .

	0.1 MHz	1 MHz	10 MHz
L_{AB} / nH	30.74	28.97	28.40
L_{GF} / nH	37.24	35.10	34.40
L_{JI} / nH	56.15	52.30	51.20
L_{DE} / nH	37.44	34.87	34.13

Table 7: Calculated parasitic busbar inductances

10.5. Modeling and Extraction of Parasitics in the IGBT Modules

10.5.1. Introduction

One of the most dominant parasitics causing even fatal problems in PWM inverters are the parasitics of the IGBT modules [9], [10]. This work models and extracts the parasitic parameters of a high-power multi-chip IGBT module. The verification of the obtained circuit model is achieved using Scattering (S-) parameters.

10.5.2 Six-pack IGBT Module

An IGBT module consisting of six chips, three IGBTs and three anti-parallel diodes, is studied. Figure 19 shows the picture of the module.

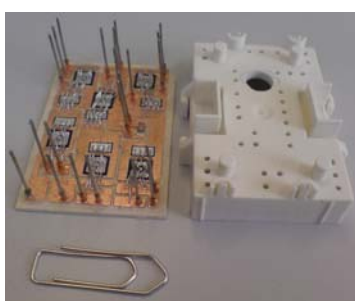


Fig. 19: Six-pack IGBT module

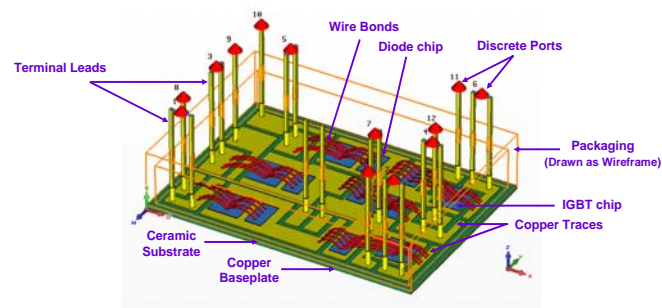


Fig. 20: EM model in CST Design Environment

10.5.3. High Frequency Electromagnetic Analysis

The EM analysis is conducted via the frequency domain solver of CST MW Studio® capturing the 3D geometrical effects and HF effects, such as skin and proximity effect, of the design. Table 8 summarizes the details of the computational analysis. The simulation model is depicted in Fig. 20.

10.5.4. Modeling and Parasitic Parameter Extraction Approach

The parameter extraction tool of CST MW Studio® based on the transmission line method is employed to compute the parasitics of the structure. This tool extracts a SPICE-compatible network model consisting of lumped elements R, L, C, G, K from previously calculated S-parameters [11]. As S-parameters represent the HF behavior of a 3D EM model equivalently, the derived circuitry responses nearly in the same way as physical device at the input/output terminals. The proposed network model of the module is shown in Fig. 21. Table 9 gives the extracted parasitic parameters.

MICROWAVE STUDIO®	
Solver Type	Frequency Domain
Mesh Type	Tetrahedral Mesh
Adaptive Grid Refinement	Yes
Number of Mesh Cells	≈ 900000
Frequency Range	0.1 MHz to 10 MHz

Table 8: HF electromagnetic analysis

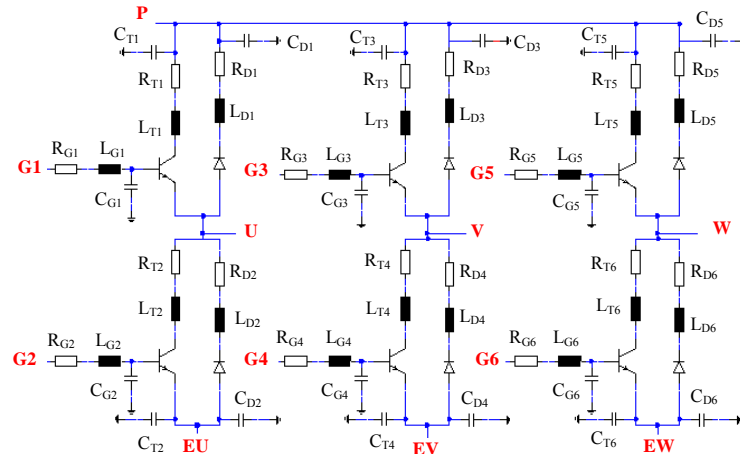


Fig. 21: Parasitic network model

First Phase Leg				Second Phase Leg			Third Phase Leg				
R_{T1} / mΩ	19.4	R_{T2} / mΩ	34.2	R_{T3} / mΩ	6.94	R_{T4} / mΩ	31.1	R_{T5} / mΩ	13.8	R_{T6} / mΩ	46.5
L_{T1} / nH	32.1	L_{T2} / nH	37.2	L_{T3} / nH	24.5	L_{T4} / nH	36.4	L_{T5} / nH	29.2	L_{T6} / nH	39.5
C_{T1} / pF	44.3	C_{T2} / pF	17.8	C_{T3} / pF	49.3	C_{T4} / pF	23.4	C_{T5} / pF	49.7	C_{T6} / pF	24
R_{D1} / mΩ	20.2	R_{D2} / mΩ	34.4	R_{D3} / mΩ	7.26	R_{D4} / mΩ	31.5	R_{D5} / mΩ	14.4	R_{D6} / mΩ	46.3
L_{D1} / nH	33.7	L_{D2} / nH	38.1	L_{D3} / nH	26	L_{D4} / nH	37.6	L_{D5} / nH	30.9	L_{D6} / nH	39.7
C_{D1} / pF	44.3	C_{D2} / pF	17.8	C_{D3} / pF	49.3	C_{D4} / pF	23.4	C_{D5} / pF	49.7	C_{D6} / pF	24
R_{G1} / mΩ	9.83	R_{G2} / mΩ	18.2	R_{G3} / mΩ	8.49	R_{G4} / mΩ	12.1	R_{G5} / mΩ	10.6	R_{G6} / mΩ	9.73
L_{G1} / nH	25.9	L_{G2} / nH	33.4	L_{G3} / nH	24.8	L_{G4} / nH	27.5	L_{G5} / nH	26.9	L_{G6} / nH	25.7
C_{G1} / pF	92.1	C_{G2} / pF	11.2	C_{G3} / pF	102	C_{G4} / pF	10.4	C_{G5} / pF	103	C_{G6} / pF	3.8

Table 9: Parasitic parameters computed at 1 MHz

10.5.5. Verification of the Parasitic Extraction Approach

As the analytical calculation of parasitic parameters for such a complex geometry is too complicated, the constructed parasitic circuit model is verified numerically. For this purpose, the circuit model is implemented in CST Design Studio™. The S-parameters for the case, when the transistor labeled as T1, is on and the current flows from the power supply to the AC motor, are computed. These results are presented in Fig. 22 together with the S-parameters of the EM model for the same case. The perfect match between both results proves the accuracy of the extraction method.

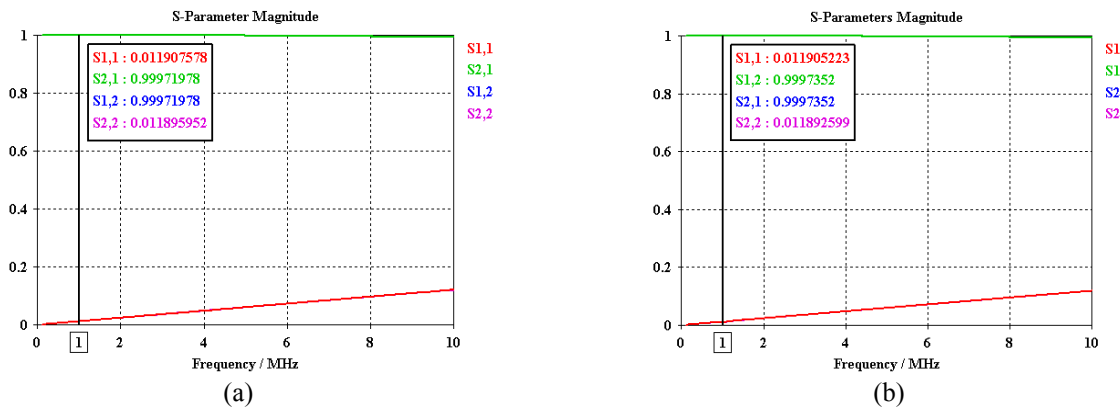


Fig. 22: Calculated S-Parameters of (a) the EM model and (b) the parasitic network model

10.5.6 Conclusions

A parasitic network model of an IGBT module is developed with the help of the network parameter extraction tool of CST MW Studio® based on the transmission line models. The electrical model and the extracted parameter values are verified by comparing the S-parameters of both electromagnetic and circuit model.

References

- [1] M. Clemens, E. Gjonaj, P. Pinder and T. Weiland, "Self-consistent simulations of transient heating effects in electrical devices using the finite integration technique," IEEE Trans. Magn., vol. 37, no. 5, pp.3375-3379, September 2001.
 - [2] M. Schauer, P. Hammes, P. Thoma, T. Weiland, "Nonlinear update scheme for partially filled cells," IEEE Trans. on Magn., vol. 39, no. 3, pp. 1421-1423, May 2003.
 - [3] M. Clemens, M. Wilke, G. Benderskaya, H. De Gersem, W. Koch and T. Weiland, "Transient electro-quasistatic adaptive schemes," IEEE Trans. on Magn., vol. 40, no. 2, pp. 1294-1297, March 2004.
 - [4] J. B. Kuang and S. A. Boggs, "Application of transient nonlinear field analysis to a distribution cable joint," Annual Report of CEIDP, p. 106-109, 1995.
 - [5] J. M. Erdman, R. J. Kerkman, D. Schlegel, and G. Skibinski, "Effect of PWM inverters on ac motor bearing currents and shaft voltages," IEEE Trans. on Ind. Appl., vol. 32, no. 2, pp. 250-259, 1996.
 - [6] A. Muetze, "Bearing currents in inverter-fed AC-motors," PhD dissertation in Technische Universitaet Darmstadt, 2004.
 - [7] M. C. Caponet, F. Profumo, R. De Doncker and A. Tenconi, "Low stray inductance bus bar design and construction for good EMC in power electronic circuits", IEEE Trans. on Power Elec., Vol. 17, No. 2, pp. 622-628, 2002.
 - [8] B. Bolsens, J. Van den Keybus, J. Driesen and R. Belmans, "Development of a measuring device for the parasitic inductance of the DC-link backplane of an inverter", IMTC, Proc. of IEEE, pp.1721-1724, 2006.
 - [9] W. Dong, "Analysis of soft-switching inverter techniques in electric vehicle applications," PhD thesis, Virginia Polytechnic Institute and State University, 2003.
 - [10] X. Huang, "Frequency domain conductive electromagnetic interference modeling and prediction with parasitics extraction for inverters", Ph.D. Thesis, Virginia Polytechnic Institute and State University, 2004.
 - [11] Computer Simulation Technology (CST), "User manual of CST Microwave Studio®", Darmstadt, 2008.